SCUOLA DI DOTTORATO

UNIVERSITÀ DEGLI STUDI DI MILANO-BICOCCA

Department of Earth and Environmental Science

PhD program in Chemical, Geological and Environmental Sciences

Cycle XXXIII

Curriculum of Environmental Sciences

SEA SURFACE TEMPERATURE PATTERNS AND OCEAN DYNAMICS IN THE MALDIVIAN REGION

Candidate Chiara DE FALCO

Registration number 835510

Supervisor Prof. Claudia Pasquero

Tutor Prof. Daniela Basso

Coordinator Prof. Marco G. Malusà

ACADEMIC YEAR 2019-2020

CONTENTS

Acknowledgements

I want to take a moment to thank all the people that helped me during these three years. I would first like to thank my supervisor, Professor Pasquero, for all her help, guidance, and patience throughout this project, and Professor Bracco for supervising and welcoming me in Atlanta, as well as for the support in the not academic troubles I had along the way. A thank goes to my research group for the interesting chats about fluid dynamics, weather forecast, home-made paintings and kitchen furniture. A special thanks to Anna, for the psychiatric help at less than 5¢. To Vale and Fabio, for being the best roommates. To Jordi, Irene, and Pietro, for being my Atlanta's family. To all my friends, for putting up with me. To Giulia, for sharing every step of this journey with me, to Ilaria, for being the other half of my brain, and to both for being the amazing women you are. To Francesco, for being there every time I need a friend. To my family, for the love, the support, and the understanding, this would have not been possible without you. To Joan, for unshakably believing in me and always being there.

English Abstract

The frequency of coral bleaching events has been increasing in recent decades due to the temperature rise registered in most regions near the ocean. Their occurrence in the Maldivian Archipelago has been observed in the months following the peak of strong El Niño events. Bleaching has not been uniform, and some reefs have been only marginally impacted. I have used satellite observations and a regional ocean model (CROCO) to explore the spatial and temporal variability of sea surface temperatures (SSTs), and quantify the relative magnitude of ENSO-related episodes with respect to the recent warming. In line with other studies, it is confirmed that the long-term trend in SST significantly increases the frequency of stress conditions for the Maldivian corals. It is also found that the interaction between currents and the steep bathymetry is responsible for a local cooling of about 0.2°C in the Archipelago during the warmest season, with respect to the surrounding waters. This cooling largely reduces the frequency of mortality conditions. The reduced SST surrounding the Maldives is probably linked to the Island Mass Effect: the enhanced productivity around small islands discovered in the sixties and documented worldwide. Despite its effects on marine productivity, the exact description of the physical processes behind the local cooling and nutrient input that enhances productivity is still unclear. From the analysis of SST variations and net primary productivity (NPP) around small islands and archipelagos, two kinds of signals can be identified, depending on the altitude and dimension of the islands. Around islands with considerable elevation and greatest diameters, cold/warm anomalies, most likely corresponding to upwelling/downwelling zones, emerge. Warmer areas don't appear around smaller islands that usually display only a local

cooling. Several oceanic and atmospheric processes might be involved. The case of the Maldives has been analyzed in detail using CROCO with increased resolution and a particle tracking model: Ariane. More than one process might coexist in generating the described patterns, the prevailing one varying along the year and depending on the strength and direction of the incoming flow. Near the Maldives, the frictional break of the currents in the presence of shallow bathymetry produces a strong vertical shear in the flow that favors vertical mixing and produces a nearly symmetric cooling around the islands. A different mechanism dominates the cooling pattern when the currents are particularly intense, such as during the monsoons: intense zonal currents cross the archipelago and give rise to intense wakes with large horizontal shear; strong upwelling originates in the lees, creating an asymmetric temperature signal (larger cooling in the lee of the islands) and obfuscating the effects of the enhanced vertical mixing.

Abstract in Italiano

La frequenza degli episodi di coral bleaching è aumentata interrottamente nelle ultime decadi a causa dell'incremento di temperatura registrato nei diversi oceani del pianeta. Nell'Arcipelago Maldiviano, tali eventi sono stati osservati principalmente nei mesi seguenti il picco di episodi El-Niño molto intensi. Il bleaching tuttavia non è stato uniforme e alcuni reef sono stati colpiti solo marginalmente. Ho utilizzato i dati da satellite e un modello oceanico regionale (CROCO) per investigare la variabilità, sia spaziale sia temporale, della temperatura superficiale dell'oceano (SST) e quantificare l'entità relativa di episodi legati ad ENSO, confrontandoli con l'effetto dell'incremento della temperatura negli ultimi decenni. In linea con altri studi effettuati, è stato confermato che il trend di temperatura aumenta significativamente la frequenza di episodi di stress termico per i coralli. È stato anche scoperto che, durante la stagione più calda, l'interazione tra le correnti e la ripida batimetria è responsabile di una diminuzione locale della temperatura elimina virgole avanati e dietro nell'Arcipelago di circa 0.2°C rispetto all'oceano circostante. Questo raffreddamento riduce notevolmente la frequenza di condizioni di mortalità per i coralli. La riduzione della SST attorno alle Maldive è probabilmente collegata all'Island Mass Effect: l'incremento di produttività intorno a isole di dimensione ridotte scoperto negli anni sessanta e documentato in tutto il mondo. Nonostante il suo effetto sulla produttività marina, l'esatto quadro dei processi che stanno dietro al raffreddamento locale e l'input di nutrienti che accresce la produttività è ancora incerto. Dall'analisi delle variazioni di SST e della produttività primaria netta (NPP) intorno a numerose isole ed arcipelaghi di piccole dimensioni sono stati identificati due tipi di pattern. Intorno ad

isole con un'altitudine considerevole e dimensioni maggiori, infatti, sono visibili anomalie calde/fredde, probabilmente corrispondenti ad aree di upwelling e downwelling. Aree più calde non sono invece visibili intorno ad isole di dimensioni minori. Sono diversi i processi, sia oceanici sia atmosferici, che potrebbero essere coinvolti e contribuire a generare il pattern di temperatura. Ho studiato nel dettaglio il caso delle Maldive, utilizzando CROCO - aumentando la risoluzione - ed un modello di particles tracking, Ariane, ed è emerso che il meccanismo predominante varia durante l'anno e dipende dalla direzione e magnitudo delle correnti. Vicino alle Maldive il rallentamento delle correnti a causa dell'attrito dovuto ad una batimetria poco profonda produce un forte shear verticale, che favorisce il mescolamento verticale e produce un raffreddamento quasi simmetrico intorno alle isole. Un altro meccanismo domina il pattern di raffreddamento quando le correnti sono particolarmente intense, come durante i monsoni: forti correnti zonali attraversano l'Arcipelago e generano wake intense con un elevato shear orizzontale; un intenso upwelling si origina nelle scie, creando un segnale di temperature asimmetrico (raffreddamento maggiore nella scia delle isole) e offuscando gli effetti del rafforzato mescolamento verticale.

CHAPTER 1

GEOGRAPHY, CLIMATE AND OCEAN DYNAMICS

1.1 Indian Ocean

The Indian Ocean is one of the major oceans on Earth, and its interaction with the atmosphere plays an important role in shaping climate on both regional and global scales (Mirsaeid et al., 2017). It exhibits a number of modes of climate variability, ranging from intraseasonal to interannual and longer time scales, most of which are coupled to the strong seasonal cycle (Schott et al., 2009). The Indian Ocean has many unique features, largely due to the extensive landmass of Asia to the north and a low latitude through flow from the Pacific via the Indonesian Throughflow (Schott et al., 2009). The presence of the Asian continent not only sets a boundary to the northward transport of heat but also drives one of the strongest monsoons on our planet. These intense winds generate a large seasonal variability throughout the year with currents, north of 10°S, displaying annual reversal (Hermes et al., 2019) including the Somali Current, the Southeast/Northwest Monsoon Currents south of India and semi-annual jets along the Equator (Wyrtki, 1973). In contrast to the Atlantic and the Pacific oceans, due to the presence of the rising branch of the Walker circulation, the Indian Ocean lacks the presence of steady equatorial trade winds. As a result, there is no climatological equatorial upwelling in the eastern ocean, in contrast to the other two tropical oceans. Instead, upwelling occurs in the Northern Hemisphere: off northwest Africa and the Arabian peninsula, and east and

west of the tip of India, and in the Southern Hemisphere along the northern edge of the southeast trades (Schott et al., 2009).

The lack of observations and data makes difficult to fully understand the decadal variability and makes it even more complex to distinguish between natural variability and climate change effects (Carson et al., 2015, Han et al., 2015, Hermes et al., 2019). However, there are strong evidences that Sea Surface Temperatures (SSTs) and heat content have been steadily increasing due to CO_2 rising concentrations related to anthropogenic emissions. Sea-level rise, increased carbon and nitrogen uptake, and more intense hydrological cycle are other effects related to global warming (Han et al., 2015, IPCC, 2013).

In the second half of Twentieth Century, the Indian Ocean has been warming faster than the other oceans (Dhame et al., 2020). In the last 20 years, one quarter of the total oceans heat intake has been adsorbed by the Indian Ocean, a big portion, taking into consideration that the Pacific and Atlantic Oceans account for broader areas (Cheng et al., 2017, Hermes et al., 2019). For example, the warming of the tropical oceans has been under the mean global rate in most of the central and eastern tropical Pacific, while the near-equatorial western Indian Ocean has warmed more than the mean global rate (Lough et al., 2018). The tropical Indian Ocean is warming at a rate of 0.15 °C year, 0.5 °C more than the same rate calculated over the tropical Atlantic and Pacific combined (Shineng and Fedorov, 2019).

Hermes et al. (2019) highlight the importance of the Indian Ocean for all the islands and the countries that surround it. More than 22 countries overlook the Indian Ocean basin, accounting for almost one third of the human population. Their water and food resources are intrinsically tight to

the state of the marine ecosystem and the influence that this basin exerts on the weather. Their economies, some of them being among the most vulnerable ones on the planet, depend on fishery and agriculture. The rising heat content of the water poses a threat to the delicate ecosystems like the coral reefs, that provide food and coast protection and attract tourists from all over the world. Marine productivity is projected to be really sensitive to climate change (Kumar et al., 2018), posing at serious risk fishery supplies. The increased heat content and its distribution influences the atmospheric circulation (Han et al., 2015), leading to anomalous winds and storm intensity, intense rainfall and drought. This extreme weather events are not only dangerous for the population safety but also to the country agriculture production. Finally, sea level rise (Han et al., 2015) is subtracting precious land from already vulnerable island countries.

1.2 Monsoons

The seasonal variability of the monsoons can be divided into four periods: the winter monsoon period, the summer monsoon period, and two transition periods between them. North of the Equator, the winter (NE) monsoon blows from the north-east, with moderate strength between December to March–April. At the Equator, the winds are weak and usually from the north. In April, the summer (SW) monsoon starts blowing from south-west, between the ITCZ (Inter-Tropical Convergence Zone) about 10°S and the Equator (Fieux, 2001). During the transition period between the end of the NE monsoon and the beginning of the SW monsoon, in April-May, the winds north of the Equator calm down. At the Equator, moderate eastward winds blow, which contrast with the westward winds over the equatorial

Pacific and Atlantic Oceans.

In most years, north of the Equator, the onset of the SW monsoon develops in two phases. It involves a reversal of the winds, which reach the Equator in early May as weak winds and progress northward along the Somali coast. In late May to mid-June, the wind intensity rises to full strength. They reach their maximum intensity over the Arabian Sea, usually in June–July. The SW monsoon blows, then, steadily from the south west from June to September–October. The NE monsoon is usually weaker than the SW, with fainter winds (Fieux, 2001, Schott and McCreary, 2001, Schott et al., 2009).

In the southern Indian Ocean, during the SW monsoon (July), the south-eastern Trades intensify and penetrate farther north than during the southern summer (January); they reach the Equator in the western part of the ocean and are the strongest in the three oceans. The air mass, full of moisture, transported by the trade winds crosses the Equator and reach the Asian continent, causing heavy rainfall (Fieux, 2001, Schott and McCreary, 2001, Schott et al., 2009). Sometimes the term 'monsoon' only refers to the wet monsoon (e.g. the SW one).

The second transition period occurs in October-November when, as during the first period, mild southeasterlies blow again. At the Equator, the zonal wind component is dominated by a semiannual period associated with the transition to westerly winds, while the meridional wind component has a strongly annual periodicity associated with the monsoon reversal (Fieux, 2001).

This is a particular wind forcing pattern that only happens in the

Indian Ocean. It is a dynamically important difference from the other tropical oceans: the absence of sustained easterly winds along the equator. (Schott and McCreary, 2001). Instead, the near-equatorial winds have an easterly component only during the late winter/early spring (Fig. 1.1,a), a semiannual westerly component during both inter-monsoons (Fig. 1.1,b), and a weak westerly annual mean (Fig. 1.1,c), as it is possible to see from the climatologies of the surface wind stress over 1999-2009 period, calculated using SCOW (the Scatterometer Climatology of Ocean Winds Risien and Chelton (2008)).

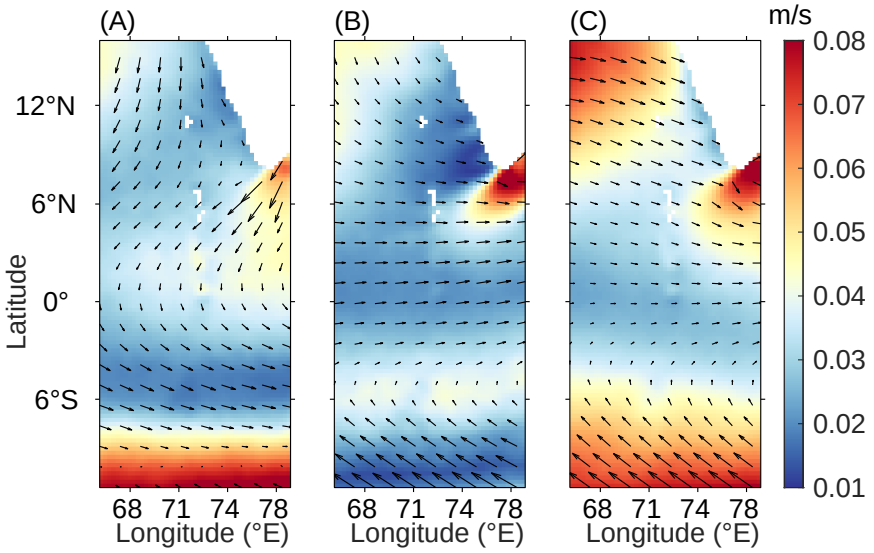

Figure 1.1: Wind Surface Stress from SCOW for (A) December-March, (B) April-May and October-November, (C) all year.

Precipitation over the Indian Ocean shows a general migration north-

ward/southward during the boreal summer/winter, following the migration of warm SSTs. Winter time cooling in the northern Arabian Sea is particularly strong because of the latent heat loss caused by cool dry air blowing off the Asian continent (Schott and McCreary, 2001).

1.2.1 Ocean Monsoon circulation

The main features of the ocean circulation in the area are well described in (Schott et al., 2009). Since the focus of my work is on the Maldives Archipelago and the West Arabian Sea, I will mainly describe the features of this area.

The South Equatorial Countercurrent (SECC) flows towards east in the northern hemisphere (0°-5° N) during the SW monsoon, while it migrates southward, below the equator, during the NE monsoon (Figs. 1.3, 1.2).

The reversing monsoon current flows south of India and Sri-Lanka and it goes east during the summer taking the name of Southwest Monsoon Current (SMC). It then turns northward after the tip of India and brings salty water from the Arabian Sea into the Bay of Bengal. During winter it flows in the opposite direction, taking the name of Northeast Monsoon Current (NMC), it flows westward across the basin during this season, carrying fresher Bay of Bengal water into the Arabian Sea. The West Indian Coastal Current (WICC) also experiences a reversal during the year: it is directed towards higher latitudes in winter and the equator during summer (Figs. 1.3, 1.2).

The Laccadives Low (LL) is a negative anomaly of about 10 cm of the Sea Surface Height (SSH) near the tip of India, it results in a cyclonic

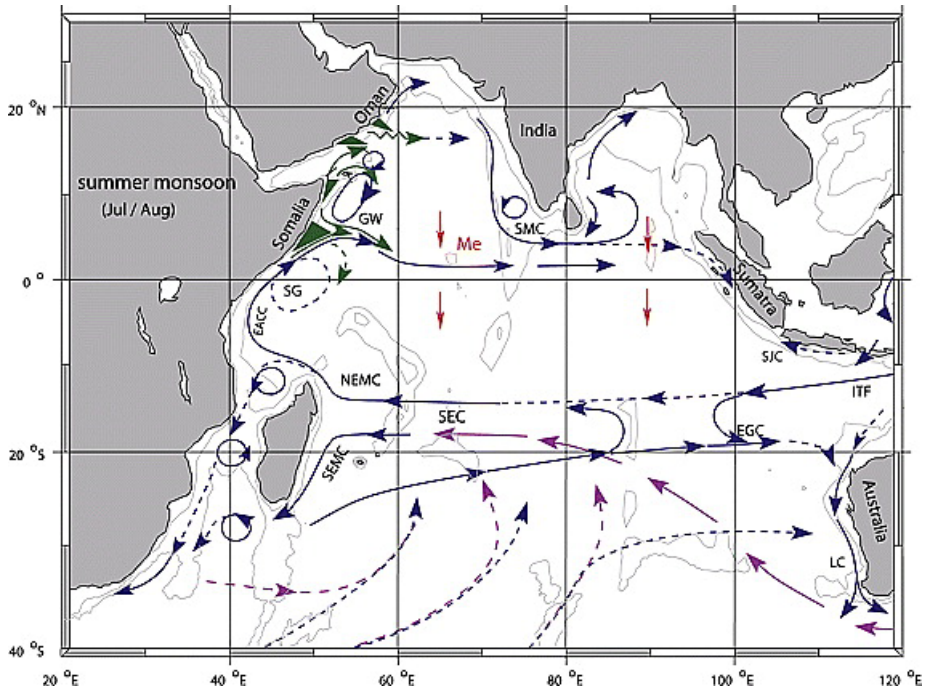

Figure 1.2: SW monsoon ocean circulation from Schott et al. (2009)

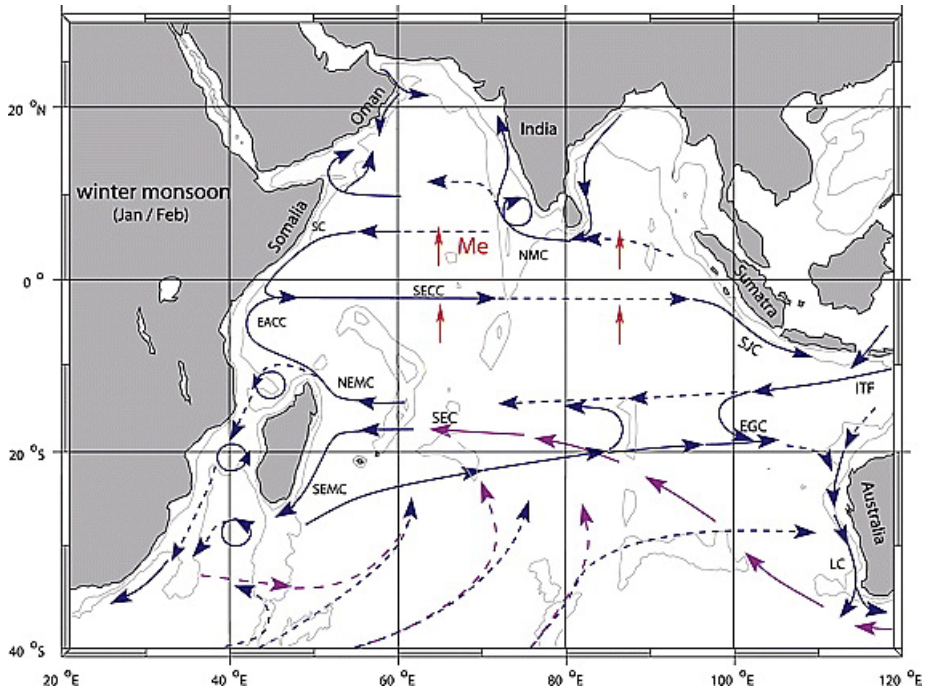

Figure 1.3: NE monsoon ocean circulation from Schott et al. (2009)

circulation, with a weak current flowing counterclockwise around the LL. In winter a similar structure forms in the same area: a positive SSH anomaly of similar magnitude, the Laccadives High (LH), results in an anticyclonic eddy with a more intense current than in summer flowing clockwise around the LH.

The spatial variability of the Mixed Layer Depth (MLD) in the Indian Ocean is also very large. The MLD can be less than 20 m during summer, while reaching more than 100 m during winter (Bhaskar et al., 2009). The area studied during this work has a seasonal cycle of about 20 m, minimum around 30 m and maximum around 60 m. It has two relatively minimum during the transition periods when winds are weaker: in April-May and October-November (see Fig. 1.4b,c). It becomes deeper during the NE and SW monsoons (see Fig. 1.4a,d).

1.3 Eddies Activity on the West Indian Coast

There is a remarkable difference - of more than 3 psu - between the sea surface salinity (SSS) in the Arabian Sea on the west side of India and the Bay of Bengal on the east side. During the SW monsoon, there is a large amount of freshwater discharge from river runoff and rainfall in the Bay of Bengal, while there is a loss of freshwater in the Arabian Sea due to excessive evaporation (Hormann et al., 2019).

The exchange of water between the two basins has a strong seasonal component, due to the reverse of the near-surface currents forced by the monsoon winds. It is also modulated by intraseasonal and interannual oscillations (Hormann et al., 2019).

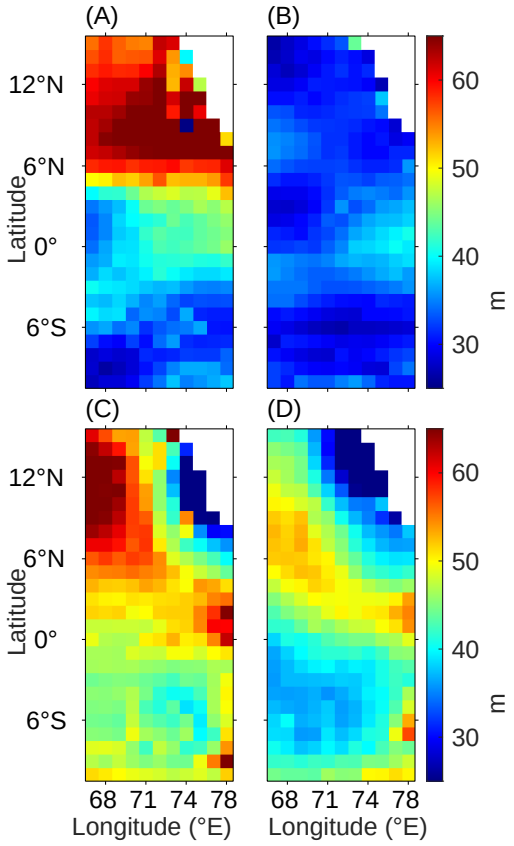

Figure 1.4: MLD from a temperature only criterion, as the depth at which the temperature difference with the surface is equal to 0.2°C. Temperature data from the World Ocean Atlas 2018 (WOA18, Zweng et al. (2018)). (A) December-February (DJF), (B) March-May (MAM), (C) June-August (JJA), (D) September-November (SON).

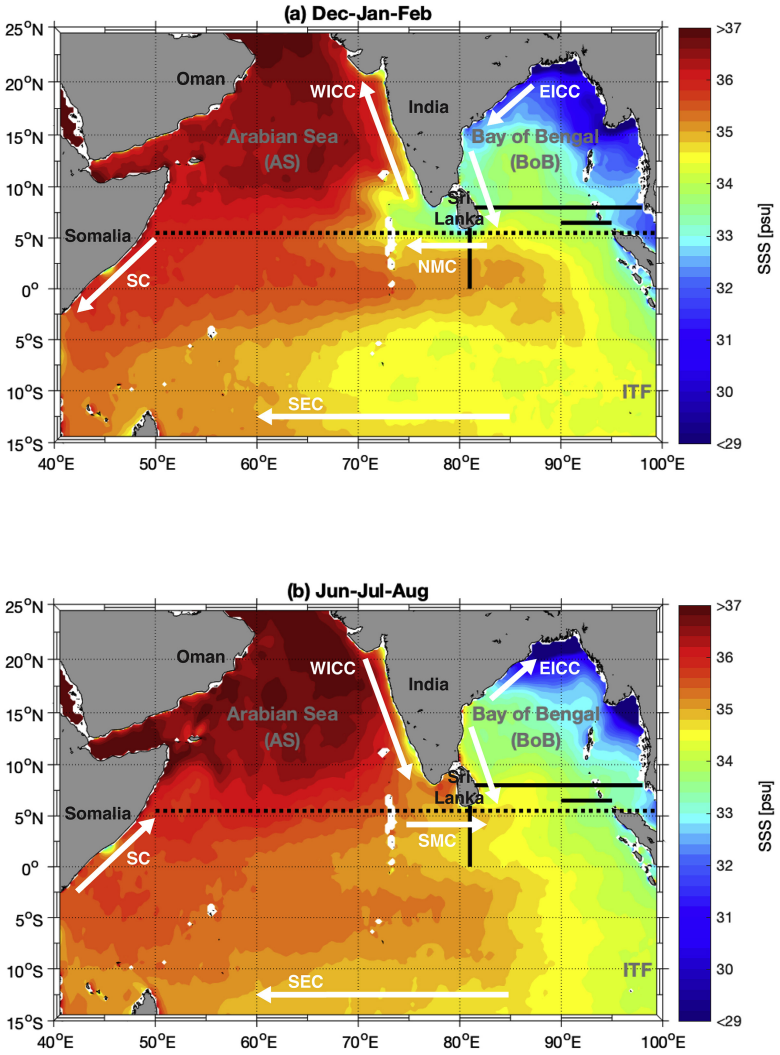

Figure 1.5: Path of the surface currents involved superimposed to the color map of mean SSS from SMAP (JPL Climate Oceans and Solid Earth group, 2019) for (A) December-February, and (B) June-August. From Hormann et al. (2019).

During the NE monsoon, the East India Coastal Current (EICC) flows southward and then it mixes with the NMC, transporting the fresher water inside the Arabian Sea. Afterward, the WICC keeps moving northward along the Indian coast (see Fig. 1.5,a). With the reversal of the currents during the Summer monsoon, the opposite process takes place, with entrainment of saltier water into the Bay of Bengal from the Arabian Sea (see Fig. 1.5,b).

This gives rise to a steep cross-shore density gradient that, in turn, generates a strong baroclinic instability. During this period there is an increased eddy activity, with meandering favoring the formation of cyclonic and anticyclonic eddies (Rao et al., 2013).

During the SW monsoon, the wind stress curl is the main eddy generation mechanism, with a climatological positive wind stress curl in the area. Accordingly to the value of the curl, cyclonic eddies are mainly detected during this period (Rao et al., 2013).

1.4 Interannual Variability

There are two main natural climate modes that influence the Indian Ocean: the El-Niño Southern Oscillation (ENSO) and the Indian Ocean Dipole Mode (IOD).

1.4.1 ENSO

El Niño events are from year to year climate fluctuations, starting with a weakening of the trades in the tropical Pacific and subsequently characterized

by a warming of the SSTs in the Eastern Equatorial part of the basin. Several dynamical processes are involved, both regarding the atmospheric and the oceanic circulation. El Niño events occur every 2-7 years and their opposite, the cold phases, are called La Niña conditions. El Niño effects propagate all over the world, affecting the global climate, marine ecosystems, and human activities (Timmermann et al., 2018).

The warming/cooling of the SSTs is coupled with a variation of the east-west sea level pressure gradient, called the Southern Oscillation. The coupled atmospheric-oceanic phenomenon is called ENSO (El Niño Southern Oscillation) (Capotondi et al., 2015). The positive phase, El Niño, is referred to as ENSO+ and the negative, La Niña, as ENSO-. It is phase locked to the annual cycle, the anomalies start developing in summer, peak in winter, and decay in spring (Schott et al., 2009).

When the SSTs change in the equatorial Pacific, they influence the atmospheric deep convection, which in turn affect the Walker Circulation. This large-scale shift in convection alters atmospheric circulation remotely, in both the tropics and extra-tropics, via atmospheric wave adjustments, often referred to as an atmospheric bridge (Schott et al., 2009, Timmermann et al., 2018).

The tropical Indian Ocean gradually warms during an ENSO year, in a basin wide way. The maximum effects are reached during the warmest season in the Maldives Archipelago: spring (March-May), about one season after SST has peaked in the Pacific at the end of the previous year (Liu and Alexander, 2007, Schott et al., 2009). During an ENSO+ year, atmospheric convection is suppressed over the tropical Indian Ocean, resulting in changes in wind patterns and cloud cover. This, in turn, influences the latent heat

and solar radiation fluxes (Schott et al., 2009).

The warming of the Indian Ocean influences precipitation all over the basin and the rim countries. A decrease in the precipitation rate over India and north-east Australia has been associated with ENSO+ events (Capotondi et al., 2015).

1.4.2 The Indian Ocean Dipole

Like ENSO, the Indian Ocean Dipole (IOD) is an interannual climate mode, sustained through positive feedbacks between equatorial winds and zonal SST gradients (Schott et al., 2009), it arises from coupled ocean-atmosphere interactions (Saji, 2018).

The SST pattern due to the IOD is characterized by a zonal gradient in the tropical Indian Ocean, with pronounced cold SST anomalies (SSTAs) in the eastern tropical Indian Ocean, off of Sumatra, and moderate warm SSTAs in the western tropical basin. It starts developing in June, and it peaks during the boreal fall, September to November (Schott et al., 2009). This is accompanied by less precipitation in the eastern Indian Ocean and increased ones in the west. These are the effects of the positive phase of the IOD, the negative one has an opposite influence, with negative SSTAs and wetter conditions in the east.

The IOD is solidly locked to the seasonal cycle, since the coupled ocean-atmosphere instability that generates is strongly modulated by the monsoon cycle (Saji, 2018). The IOD and ENSO have strong interactions, due to the proximity of Pacific and Indian Ocean and the existence of oceanic and

atmospheric pathways.

1.5 The Maldives

The Maldives are an atoll nation located in the centre of the Laccadive-Chagos ridge in the central Indian Ocean, south-west from the tip of India. It stretches for 860 km from latitude about 7°N to the equator, it is a long but narrow archipelago, ranging in longitude from 72° to 73°E. It has 26 atolls and more than one thousand coral islands. This makes it one of the largest atoll groups, but also one of the least studied (Naseer, 2003). It was evaluated to be the country with the seventh largest reef ecosystem within its borders, by the United Nation Environment Programme (UNEP). About 193 of the islands are inhabited by native Maldivians, 93 islands have tourist resorts, and 55 islands are reserved for industrial and agricultural use (Quinn and Zahir, 2013).

Mid-ocean coral islands are low-lying accumulations of locally derived calcareous sand and gravel deposited on reef platforms that provide the only habitable land in atoll nations such as the Marshall Islands, Kiribati, Tuvalu, and the Maldives. Atoll islands are morphologically sensitive, susceptible to widespread destruction given future sea-level rise and significant alteration during extreme natural events (Kench et al., 2006). The very low altitude of the islands, about 5 m, makes the Maldives one of the countries at greatest risk for the effects of climate change (Wilkinson, 2008). The health of the coral reefs, which are the physical basis of the Maldives, are of national strategic concern (Zahir et al., 2009).

Coral reefs form the resource base for the two major economic sectors:

Figure 1.6: Satellite image of the Maldives from EnviSat

tourism and fishery. The tourism industry has become the largest income earner. The tourism sector provides most of the reef management by reducing the exploitation of fish, coral rock and sand, and other reef resources in proximity to the resorts (Wilkinson, 2004). Coral reefs constitute the primary building material (Kench, 2011). The density of the population is low, except in the capital Malé, and there are large distances between atolls. The historically low population densities in the Maldives resulted in a large area of coral reefs where the influences of humans were low (Zahir et al., 2009). However over-fishing and pollution from poor land use and inadequate treatment of waste are among the major threats (Wilkinson, 2008). The future of coral reefs is uncertain. Anthropogenic activities seriously endanger the future of these ecosystems. Scarce information about the reefs health are available on a climatic scale since it has been only the

end of the 20th century, after the 'monstrous' 1998 El-Niño, that systematic and quantitative surveys of reefs were conducted by the government of the Maldives through the Marine Research Center (MRC), Ministry of Fisheries and Agriculture (Naseer, 2003). Unfortunately, the coverage is not uniform, with the northern and central reefs better surveyed than the southern ones (Ibrahim et al., 2017).

The atolls are arranged in two double chains separated by an inner see, deeper than the lagoons (20 - 80 m) but much shallower than the surrounding ocean (see Fig.1.6). There are broad and deep channels in between some atolls, where monsoon currents can reach velocities up to 2 m/s. An atoll consists of 2 components: the rim and the lagoon. The rim may consist of a single continuous reef with few or no reef passes (deep openings) to the ocean, or it may consist of many individual reefs with several passages to the ocean. The morphology of atoll rim reefs may be complex, having reef islands, sand bars, reef lagoons of variable depths, and extensive coral and sand flat formations (Naseer, 2003).

The archipelago is situated in a predominantly storm-free environment, uniquely located in the monsoon wind regimes of the Indian Ocean. A wet monsoon dominates the period April to November when the winds blow from the southwest. A dry season occurs from December to March with lighter winds from the northeast. The seasonal cycle of the heat flux is small and strongly modulated by the cloud cover and wind strength (see Fig. 1.7).

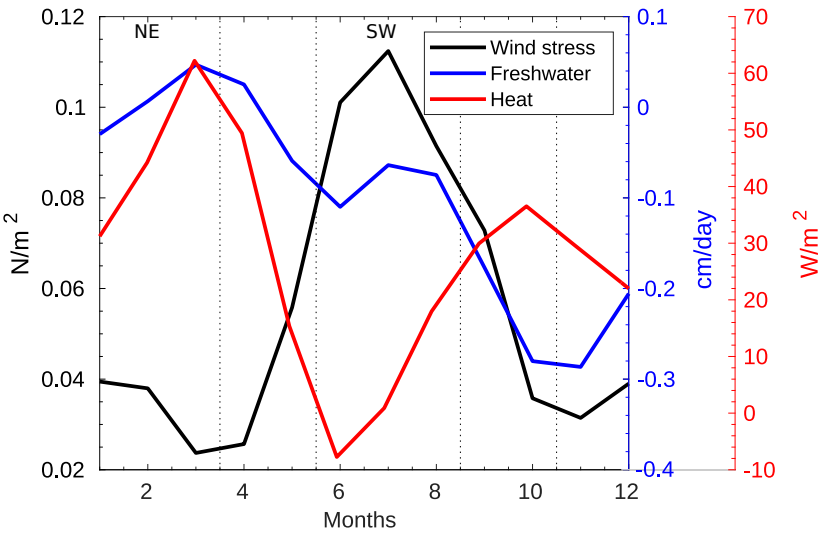

Figure 1.7: Spatially averaged over the Archipelago wind stress, freshwater flux (calculated as the difference between precipitation and evaporation) and net heat flux (the sum of long and short wave radiation, latent heat, and sensible heat) from atmospheric reanalysis ERA5 (Copernicus Climate Change Service C3S, 2017).

1.6 Modelling of ocean circulation near small islands and archipelagos

There are only few articles available in literature regarding the modeling of ocean dynamics in archipelagos and near small islands. The complexity of the system and, often, the scarcity of in situ data -of fundamental importance for the validation of the achieved results- make the development of these models a difficult task. Other limiting factors to consider are the model resolution together with insufficient computational power. Just recently, analyses of the ocean dynamics circulation and forecast systems have been developed (e.g. the Philippine, Han et al. (2009) and Arango et al. (2011); the Madeira Archipelago, Caldeira et al. (2016); Hawaii, de Souza et al. (2015); the Juan Fernandez Archipelago, Andrade et al. (2014a)).

Furthermore, there are still few studies that investigate the dynamics and circulation around the Maldives. Few brief information are provided by Preu and Engelbrecht (1991), that talk about upwelling cells due to monsoonal currents; however, there is no explanation of the involved dynamical mechanisms, patterns, and seasonality. Upwelling is reported also by Sasamal (2006) from satellite data of chlorophyll-a. Peaks in the concentration of chlorophyll-a are attributed to wake eddies due to the interaction between currents and bathymetry, however a systematic analysis is missing. A brief study of the interaction between currents and the islands was also performed by Owen et al. (2011), using a two-dimensional model in which the atolls are represented by simplified shapes. The models only analyse the interaction between a completely zonal flow (eastward and westward) and the surface atoll shapes. The main focus of the work was to study the currents speed in the main channels to provide information about the

possibility of extracting energy from waves. To my knowledge, these are all the available papers.

CHAPTER 2

DATASETS AND MODEL

To characterize the physical settings of the area and the ocean circulation, I have used several typologies of datasets and I have run a dynamical model, CROCO (Coastal and Regional Ocean COmmunity model), analyzing its outputs.

2.1 Data

2.1.1 Satellite Data

The observational SST dataset of choice in this work is the Group for High Resolution Sea Surface Temperature (GHRSST) Level 4 (National Centers for Environmental Information (NOAA), 2016), available over the period 1982 - 2018 with daily temporal and 0.25° spatial resolution. It is based on SST measured by Advanced Very High Resolution Radiometers (AVHRR) blended with in-situ observations, ships and buoys (both drifters and moorings), using the Optimal Interpolation (OI) method (Reynolds et al., 2007).

We performed a more detailed analysis of some years using a version of GHRSST at higher spatial resolution (0.054°), available from April 2006 (UK Met Office, 2005). This last version uses satellite data from multiple sensors

in addition to AVHRR, including the Advanced Along Track Scanning Radiometer (AATSR), the Spinning Enhanced Visible and Infrared Imager (SEVIRI), the Advanced Microwave Scanning Radiometer-EOS (AMSRE) and the Tropical Rainfall Measuring Mission Microwave Imager (TMI).

Thermal infrared SST measurements, as in the case of the first dataset, have the advantage of providing long time series, however, the wavelengths used for the radiometric observations overlap with the clouds infrared adsorption spectrum and are sensitive to the scattering of atmospheric aerosols and water vapor. On the other hand, the longer wavelengths used by passive microwave instruments are mostly transparent to clouds, even though accuracy and resolution are worse due to the lower strength of the Earth's signal in the microwave spectrum. The most recent products, as the second dataset used, blend SSTs from different types of sensors. Since the two kind of instruments effectively measure two different kinds of SST, skin and sub-skin, and the in-situ measurements usually provide bulk SST, careful corrections must be applied during the blending process. The different effects on each SST of the temperature gradient with depth, diurnal heating, evaporative cooling, and the biases introduced by different atmospheric conditions must be taken into consideration (Minnett, Peter and Kaiser-Weiss, Andrea, 2012). The blending and interpolation algorithms, used to obtain a field on a regularly spaced grid without swap gaps, introduce their own errors, usually provided with the final product together with the instruments sensitivity(GHRSST Science Team (2010), 2011).

2.1.2 Ocean and Atmosphere Reanalysis

Reanalyses merge observations with numerical models to produce a synthesized estimate of the state of the system. Typically, they extend for several decades and provide information about the entire globe. The atmospheric and the oceanic reanalysis used in this work are ERA5 and SODA3, respectively.

ERA5 (Copernicus Climate Change Service C3S, 2017) is the latest climate reanalysis produced by ECMWF (European Centre for Medium-Range Weather Forecasts), providing hourly data on many atmospheric, land-surface, and sea-state parameters together with estimates of uncertainty. ERA5 data are available in the Climate Data Store on regular latitude-longitude grids at 0.25° x 0.25° resolution, with atmospheric parameters on 37 pressure levels. ERA5 covers the period from 1950 to the present.

The Simple Ocean Data Assimilation (SODA) (Carton et al., 2018) reanalysis version 3 relies on the ocean component of the NOAA Geophysical Fluid Dynamics GFDL coupled with the Modular Ocean Model MOM5 and the Sea Ice Simulator SIS1. It is eddy permitting and has a resolution of 1/4° x 1/4° degree and 50 vertical levels. A scheme has also been implemented to reduce the bias in the surface fluxes. It covers the period 1980–2017 at a spatial resolution of 0.25° available as 5-day averages. In order to be consistent, to force CROCO, I have chosen SODA3.4.2 since it is coupled with ERA-Interim (Dee et al., 2011), the closest reanalysis to ERA5. Unfortunately, some of the 5 days average files have been lost and not the whole 1980-2017 period is available, when I needed to analyse the 37-years I have used SODA3.7.2, forced with JRA-55 (Japan Meteorological

Agency, Japan, 2013).

2.2 CROCO

The model adopted is the Coastal and Regional Ocean Community model (CROCO)(Auclair et al., 2018) (https://www.croco-ocean.org). Over the last 2 decades, the Regional Oceanic Modeling System (ROMS) was developed between UCLA, Rutgers University and IRD. It is a three-dimensional numerical oceanic model intended for simulating the circulation, biogeochemical cycles, and sediment dynamics in various coastal regions and at high resolution (Marchesiello, 2020). CROCO is an oceanic modeling system built upon the IRD version of the model made use of the AGRIF grid refinement procedure developed at INRIA (Grenoble) and designed for simulating high-resolution offshore and nearshore dynamics (Shchepetkin and McWilliams, 2005).

Unresolved processes are taken into account by providing a range of possible parametrizations, the choice of which is strongly linked to the studied area, the adopted resolution and the investigated subject. Lateral and vertical mixing schemes are used, introducing their own errors and limitations. Bottom friction is parametrized using a classic vertical logarithmic profile defined by a shear velocity and bottom roughness. The bottom roughness is defined empirically and, therefore, it is not always the best representation of reality. Finite differences close to a steep topographic slope generate important numerical errors and the original bathymetry needs to be smoothed to minimize them. Pressure gradient errors are also introduced by Boussinesq approximation and the empirical nonlinear equation of state, the

used one is the UNESCO formulation as derived by Jackett and McDougall (1995).

However, CROCO is widely used model that has been shown to be able to reproduce reliable results in a reasonable amount of time (e.g Fringer et al. (2019), Huo and Peltier (2021), Lahaye et al. (2019), Renault et al. (2016)).

An important objective for CROCO is to resolve very fine scales (especially in the coastal area), and their interactions with larger scales. By default, CROCO solves the same primitive equations as in ROMS, also using the same robust and efficient time-splitting method (Debreu et al., 2012, Shchepetkin and McWilliams, 2005). Recently, also options for non-hydrostatic applications have been implemented (Auclair et al., 2018),

It has the capability of a 2-way nesting procedure with a high resolution 'child' model embedded into a coarser resolution 'parent' model (Debreu et al., 2012). This is a fundamental tool to proceed with the down-scaling and therefore achieve higher resolutions. Lagrangian tracers can be deployed at different times along the reefs to quantify the impact of the submesoscale currents on transport and mixing, although I have decided not to use this feature but to use another model, Ariane (`https://mespages.univ-brest.fr/~grima/Ariane/`), to track the Lagrangian particles behaviour.

2.2.1 Equations of Motion

CROCO is a three dimensional, free surface, hydrostatic (in this application), eddy-resolving ocean model. It uses split-explicit time stepping to solve the

set of primitive equations that describes the physics of the ocean, consisting of the mass and momentum budgets, the equation of state for seawater, and conservation equations for tracers such as temperature and salinity (Vallis, 2017).

The governing equations in simple form in Cartesian coordinates are the momentum equations:

$$\frac{\partial u}{\partial t} + \vec{\nabla} \cdot (\vec{v}u) - fv = -\frac{\partial \phi}{\partial x} + \mathrm{F}_u + \mathrm{D}_u \tag{2.1}$$

$$\frac{\partial v}{\partial t} + \vec{\nabla} \cdot (\vec{v}v) + fu = -\frac{\partial \phi}{\partial y} + \mathrm{F}_v + \mathrm{D}_v \tag{2.2}$$

the hydrostatic equation:

$$\frac{\partial \phi}{\partial z} = -\frac{\rho g}{\rho_0} \tag{2.3}$$

continuity equation:

$$\vec{\nabla} \cdot \vec{v} = \frac{\partial u}{\partial x} + \frac{\partial v}{\partial y} + \frac{\partial w}{\partial z} = 0 \tag{2.4}$$

the scalar transport equation:

$$\frac{\partial C}{\partial t} + \vec{\nabla} \cdot (\vec{v}C) = \mathrm{F}_C + \mathrm{D}_C \tag{2.5}$$

the equation of state:

$$\rho = \rho(T, S, P) \tag{2.6}$$

Where:

$\vec{v} = (u, v, w)$ is the velocity

$\vec{\nabla} = \frac{\partial}{\partial x} + \frac{\partial}{\partial y} + \frac{\partial}{\partial z}$ is the divergence

$\mathrm{D}_u, \mathrm{D}_v, \mathrm{D}_C =$ Diffusive terms

$\mathrm{F}_u, \mathrm{F}_v, \mathrm{F}_C =$ Forcing terms

$f(x, y) =$ Coriolis force

$\phi(x, y, z, t) =$ Dynamic Pressure :$\phi = (P/\rho_o)$

$P =$ Total Pressure, $\mathrm{P} \approx -\rho_o g z$

$u, v, w =$ the (x, y, z) components of the velocity

Equations 2.1 and 2.2 are the momentum balance equations in x and y directions, respectively. The Boussinesq approximation: the density variations in the ocean are quite small compared to the mean density of the ocean ρ_0 (Vallis, 2017) (I have chosen ρ_0=1027 kg/m^3). The contribution of density can then be neglected in the momentum equations except in the buoyancy force in the vertical momentum equation. Under the hydrostatic approximation, it is further assumed that the vertical pressure gradient balances the buoyancy force. Therefore, equation 2.4 is the continuity equation for an

incompressible fluid. Non-hydrostatic processes, such as convection, have to be parametrized. Despite the adoption on the Boussinesq approximation CROCO takes into account the compression induced by vertical pressure changes in the barotropic mode (Shchepetkin and McWilliams, 2009). As equation of state 2.6 a full, non-linear equation is adopted (Shchepetkin and McWilliams, 2003). Furthermore, the geopotential surfaces are assumed to be spheres so that gravity is parallel to the earth's radius (spherical earth approximation) and the depth of the ocean is considered negligible compared to the radius of the earth (thin-shell approximation).

Equations for Vertical Boundary conditions are given by :

at Top, $z = \zeta(x, y, t)$

$$\begin{aligned} K_m \frac{\partial u}{\partial z} &= \tau_s^x(x, y, t) \\ K_m \frac{\partial v}{\partial z} &= \tau_s^y(x, y, t) \\ K_c \frac{\partial C}{\partial z} &= \frac{Q_c}{\rho_o c_p} \\ w &= \frac{\partial \zeta}{\partial t} \end{aligned} \tag{2.7}$$

and at Bottom, $z = -h(x, y)$

$$\begin{aligned} K_m \frac{\partial u}{\partial z} &= \tau_b^x(x, y, t) \\ K_m \frac{\partial y}{\partial z} &= \tau_b^y(x, y, t) \\ K_c \frac{\partial C}{\partial z} &= 0 \\ -w + \vec{v} \cdot \nabla h &= 0 \end{aligned} \tag{2.8}$$

Where:

K_m, K_C = Vertical Eddy Viscosity and Diffusivity

$\zeta(x, y, t)$ = surface elevation

Q_C =surface concentration flux

τ_s^x, τ_s^y =surface wind stress

τ_b^x, τ_b^y =bottom stress

Q_C and τ_s^x, τ_s^y are provided as forcing fluxes and described in the following paragraphs. At the bottom, the horizontal velocity components are constrained to accommodate a prescribed bottom stress.

ROMS has a free surface $\zeta(x, y, t)$ = (Shchepetkin and McWilliams, 2005); hence it is able to resolve the evolution of the surface elevation and the barotropic gravity waves, which are about two orders of magnitude faster than the baroclinic waves (Griffies et al., 2000). This approach has several advantages over the rigid-lid and implicit free-surface methods

(Griffies et al., 2000, Shchepetkin and McWilliams, 2005): Among these are a better numerical stability and flow characteristics over rough topography, a straightforward implementation of the input of freshwater, and computational efficiency.

2.2.2 Terrain following, sigma coordinates and horizontal coordinates

These equations are discretized in an orthogonal curvilinear coordinate system in the horizontal direction and a stretched terrain-following coordinate system in the vertical direction (Shchepetkin and McWilliams, 2003, 2005, Song and Haidvogel, 1994). Terrain-following coordinate systems have been developed in ocean circulation models to study coastal regions: they grant an increase in the vertical resolution as the water column shoals or in a designated area of interest, such as in the thermocline or in the bottom boundary layers. One major challenge is that, as the ocean gets deeper towards the interior basin, the vertical resolution of the surface ocean mixed layer decreases leading to a poorer representation of surface processes (Griffies et al., 2000, Shchepetkin and McWilliams, 2003). In ROMS, this problem has partly been mitigated by introducing vertical stretching functions that increase the resolution towards the surface (Haidvogel and Beckmann, 1999, Shchepetkin and McWilliams, 2003, Song and Haidvogel, 1994). The sigma level models are very sensitive to topography, which results in numerical errors in the pressure gradient. Due to these numerical errors, the energy of the model might diverge and cause the model to 'blow-up'. In small regional domains this is less of a problem because water masses are renewed at the open boundary. However, the horizontal pressure gradient errors generated

due to difference between the gradient along the sigma surface and bottom topography, have to be minimized. It is therefore necessary to smooth the bathymetry: a Hanningan filter (Velleman and Hoaglin, 1981) has been repeatedly applied until the slope factor (rx0) and the Haney number (rx1) (Shchepetkin and McWilliams, 2003) values for a numerically stable grid were reached.

The vertical velocity in s-coordinate is Ω:

$$\Omega(x, y, s, t) = \frac{1}{H_z}\left[w - (1+s)\frac{\partial \zeta}{\partial t} - u\frac{\partial z}{\partial x} - v\frac{\partial z}{\partial y}\right] \tag{2.9}$$

and the vertical velocity w then is:

$$w = \frac{\partial z}{\partial t} + u\frac{\partial z}{\partial x} + v\frac{\partial z}{\partial y} + \Omega H_z \tag{2.10}$$

Due to the application of the vertical stretching coordinate, each grid cell has different thickness (H_z) and volume. The model state variables are vertically staggered so that the horizontal momentum (u,v) and tracers are located at the center of each grid cell. The vertical velocity is computed at the bottom and top faces of the cell.

In CROCO, two vertical transformations are available for the generalized vertical terrain following the vertical system, indicated as vtrasform=1 and vtrasform=2. The vertical coordinate transformation equations can be

written, respectively, as:

$$\begin{aligned} z(x,y,\sigma,t) &= z_0(x,y,\sigma) + \zeta(x,y,t)\left[1 + \tfrac{z_0(x,y,\sigma)}{h(x,y)}\right] \\ z_0(x,y,t) &= h_c\sigma + [h(x,y) - h_c]\, C_s(\sigma) \end{aligned} \tag{2.11}$$

and

$$\begin{aligned} z(x,y,\sigma,t) &= \zeta(x,y,t) + [\zeta(x,y,t) + h(x,y)]z_0(x,y,\sigma), \\ z_0(x,y,\sigma) &= \tfrac{h_c\sigma + h(x,y)C_s(\sigma)}{h_c + h(x,y)} \end{aligned} \tag{2.12}$$

where $z_0(x,y,\sigma)$ is a nonlinear vertical transformation, $\zeta(x,y,t)$ is the time-varying free-surface, $h(x,y)$ is the ocean bottom, σ is a fractional vertical stretching coordinate ranging from $1 \leq \sigma \leq 0$ $C_s(\sigma)$ is a non-dimensional, monotonic, vertical stretching function ranging from $1 \leq C_s(\sigma) \leq 0$, and h_c is a positive thickness controlling the stretching, it gives approximately the transition depth between the horizontal surface levels and the bottom terrain following levels. Just for this first transform, it has to be smaller than hmin, the minimum depth of the topography, or it would lead to $\partial z/\partial\sigma < 0$.

For vtransform=1 (Song and Haidvogel, 1994)

$$C(\sigma) = (1 - \theta_B) \frac{\sinh(\theta_S \sigma)}{N} + \theta_B \left[\frac{\tanh\left[\theta_S \left(\sigma + \frac{1}{2}\right)\right]}{2 \tanh\left(\frac{1}{2}\theta_S\right)} - \frac{1}{2} \right] \tag{2.13}$$

where θ_S and θ_B are the surface and bottom control parameters. Their ranges are $0 < \theta_S \leq 20$ and $0 < \theta_B \leq 1$, respectively. N is the number of vertical levels.

For vtransform=2 (Shchepetkin, 2005)

$$\begin{gathered} sc = \frac{\sigma - N}{N} \\ csf = \frac{1 - cosh(\theta_s sc)}{cosh(\theta_s) - 1} \; if \; \theta_b > 0, \\ or \; csf = -sc^2 \\ C_s(\sigma) = \frac{exp(\theta_b csf) - 1}{1 - exp(-\theta_b)} \; if \; \theta_s > 0, \\ or \; C_s(\sigma) = csf \end{gathered} \tag{2.14}$$

The resulting stretching function is continuous with respect to θ_S and θ_B as their values approach zero. They have a range of: $0 < \theta_S \leq 10$ and $0 < \theta_B \leq 4$.

In the horizontal, the state variables in CROCO are staggered on an Arakawa-C grid (Arakawa and Lamb, 1999) and they are evaluated over a boundary fitted orthogonal coordinates system (ξ, η). The free-surface (ζ),

density (ρ), and active or passive tracers (t) are located at the center of the cell. The horizontal velocities (u) and (v) are located at the west-east and south-north edges of the cell, respectively. The density (ρ) is computed between points where the computation of currents takes place. (Arakawa and Lamb, 1999, Griffies et al., 2000, Haidvogel and Beckmann, 1999).

2.2.3 Numerical Schemes

The horizontal momentum equations in ROMS are solved in a split-explicit time-stepping scheme (Shchepetkin and McWilliams, 2005, 2009), which separates the faster barotropic mode from the slower baroclinic mode. Thus, the model calculates the evolution of the depth-integrated barotropic flow at a much faster time step than the vertical deviation from the barotropic flow. In order to avoid the errors associated with the aliasing of frequencies resolved by the barotropic steps but unresolved by the baroclinic step, the barotropic fields are time averaged before they replace those values obtained with a longer baroclinic step. A cosine shape time filter, centered at the new time level, is used for the averaging of the barotropic fields (Shchepetkin and McWilliams, 2005). In addition, the separated time stepping is constrained to maintain exactly both volume conservation and consistency preservation properties which are needed for the tracer equations (Shchepetkin and McWilliams, 2005). The equations are time discretized using a third order accurate predictor (Leap-Frog) and corrector (Adams-Molton) time-stepping algorithm. Mode coupling only occurs for the corrector sub-step.

In numerical modeling applications, the grid spacing is too large to resolve the small scale turbulent processes on terrain following sigma levels.

Of particular importance for my research, which focuses on the vertical exchange of tracers, in particular temperature, are the representations of processes associated with vertical mixing of mass and momentum.

ROMS is built with five different turbulent closure methods, the one I have used is the K-profile parametrization (KPP). Many schemes have a background molecular value which is used when the turbulent processes are assumed to be small (such as in the interior). The KPP is a widely used parametrization scheme in most of the ocean modeling systems. It is based on the Monin-Obukov similarity theory and provides an estimate of the vertical mixing with both local and non-local sources (Large et al., 1994). This first-order closure scheme (Large et al., 1994) approximates mixing processes through the product of the vertical gradient of momentum and tracers, and the corresponding local eddy viscosity and diffusivity coefficients. This mixing scheme treats the oceanic surface and bottom boundary layer, and mixing in the ocean interior, separately.

CROCO first calculates the vertical eddy viscosity and diffusivity for the entire water column, in the absence of the surface and bottom boundary layer, as the superposition of three processes: the local Richardson number instability due to resolved vertical shear, internal wave breaking, and double diffusion both for momentum and tracers.

$$K_{m,s}(z) = K^{\mathrm{sh}}_{m,s}(z) + K^{\mathrm{iw}}_{m,s}(z) + K^{\mathrm{dd}}_{m,s}(z) \tag{2.15}$$

Turbulent mixing due to shear instability in the vertical velocity profile is typically regionally and temporally confined to regions of strong currents as it happens in the narrow passages among the atolls that form the Maldivian

Archipelago. The diffusivity associated is defined by the ratio of the local gradient Richardson number ($\mathrm{Ri_g}$) and a critical value $\mathrm{Ri_0}$ equal to 0.7, where $\mathrm{Ri_g}$ is defined as the ratio between the Brunt-Vaisala frequency ($\mathrm{N^2}$) and the shear (Vallis, 2017).

$$Ri_g = \frac{N^2}{(\partial u/\partial z)^2 + (\partial v/\partial z)^2} \tag{2.16}$$

Whether there is mixing or not, the magnitudes of the viscosity and diffusivity are defined by:

$$K^{sh}_{m,s}(z) = \begin{cases} K_0 & Ri_g < 0 \\ K_0 \left[1 - \left(\frac{Ri_g}{Ri_0}\right)^3\right] & 0 < Ri_g < Ri_0 \\ 0 & Ri_0 < Ri_g \end{cases} \tag{2.17}$$

$$K_0 = 5 \times 10^{-3}\ \mathrm{m^2\ s^{-1}}, \quad \mathrm{Ri_0} = 0.7$$

Where K_0 is the maximal diffusivity. Values of $\mathrm{Ri_g}$ greater than $\mathrm{Ri_0}$, are associated with a stable stratification. For negative values, due to a negative Brunt-Vaisala frequency and, therefore, definitely unstable, K is set to $\mathrm{K_0}$.

Diffusivity and viscosity due to internal wave breaking are taken as inversely proportional to Brunt-Vaisala frequency N (Gargett and Holloway,

1984).

$$K_m^{\mathrm{iw}}(z) = \frac{10^{-6}}{\sqrt{\max\left(N^2(z), 10^{-7}\right)}}, \quad K_s^{\mathrm{iw}}(z) = \frac{10^{-7}}{\sqrt{\max\left(N^2(z), 10^{-7}\right)}} \tag{2.18}$$

The last component in eq. 2.15 is the double diffusive mixing. It can occur when the vertical gradient of density is stable, but the vertical gradient of either salinity (salt fingering) or temperature (diffusive convection) is unstable in its contribution to density (Large et al., 1994). Regions of active salt fingering and diffusive convection can be identified using the double-diffusion density ratio R_ρ.

$$R_\rho = \frac{\alpha \partial_z T}{\beta \partial_z S}, \tag{2.19}$$

Where α and β are the thermodynamic expansion coefficients for temperature and salinity, respectively. The mixing of momentum from double diffusion is treated in the same fashion as the diffusive mixing of salinity $K_m^{dd} = K_s^{dd}$.

For the salt filtering condition, $R_\rho > 1$:

$$K_s^{dd} = \begin{cases} 1 \times 10^{-4} \left[1 - \left(\frac{(R_\rho - 1}{R_\rho^0 - 1} \right)^2 \right)^3 & 1.0 < R_\rho < R_\rho^0 \\ 0 & \text{otherwise} \end{cases} \tag{2.20}$$

$$K_T^{dd} = 0.7 K_s^{dd}$$

Where $R_\rho^0 = 1.9$

In case of the diffusive condition, $0 < R_\rho < 1$, for the temperature:

$$K_T^{dd} = \left(1.5 \times 10^{-6}\right) \left(0.909 \exp\left(4.6 \exp\left[-0.54 \left(R_\rho^{-1} - 1\right)\right]\right)\right) \tag{2.21}$$

For other scalars:

$$K_s^{dd} = \begin{cases} K_T^{dd} \left(1.85 - 0.85 R_\rho^{-1}\right) R_\rho & \text{for } 0.5 \leq R_\rho < 1.0 \\ K_T^{dd} 0.15 R_\rho & \text{otherwise} \end{cases} \tag{2.22}$$

The depth of the boundary layer (HBL) is obtained using a modification of the original KPP scheme (McWilliams et al., 2009). It calculates HBL from the sum of four different terms (Cr(z)) that takes into account shear, buoyancy, rotation, and turbulent entrainment. The first level z at which Cr(z)=0 corresponds to the value of HBL. An integral layer is defined, where production of turbulence by shear balances dissipation by the stratification. A non-dimensional vertical shape function is used to define the vertical profile of diffusivity in the boundary layer that varies continuously reaching

the value 0 at the bottom of the layer. This shape function is then multiplied by the HBL and the turbulent velocity scale (that depends on the surface forcing) to get the local value of the diffusivity. This scheme is consistent with the original one and has the advantages of also being consistent with the Ekman problem and producing a deeper mixed layer (CROCO Developing Team, 2020).

Additionally, KPP calculates a non-local transport (γ) term that accounts for the unresolved penetration into the layers below the mixed layer, although this term only regards the tracers and it is always zero for the momentum (Large et al., 1994). The bottom boundary layer option is calculated is the same way as the surface one.

The choice of the vertical mixing parameterizations is always a complex step during the setting of a model. The original KPP used to produce a shallower ML and to overestimates the SST (Damerell et al., 2020) than other schemes, e.g. the GLS (Generic Length Scale) (Umlauf and Burchard, 2003) or the M-Y2.5 (level 2.5 Mellor-Yamada turbulence closure) (Mellor and Yamada, 1982). However, it is hard to define which one is the best, all have their strengths and weaknesses (Damerell et al., 2020), comparisons have shown different outcomes depending also on the area and domain chosen (Damerell et al., 2020, Durski et al., 2004, Robertson and Dong, 2019). The modified KPP scheme adopted was able to well reproduce the MLD seasonal cycle and the vertical stratification in the studied area (see paragraph 2.3.3).

A split and rotated third-order upstream horizontal advection scheme is used for tracers and momentum that are calculated vertically with a fourth-order centered vertical advection scheme.

2.3 Ariane

The particles tracking model adopted is ARIANE (Blanke and Raynaud, 1997). Using the Eulerian velocity field provided by an ocean circulation model, as CROCO, it can calculate the three-dimensional trajectories of Lagrangian particles. Streamlines are computed analytically and, assuming that the velocity field is stationary, they represent the trajectory of each parcel.

It solves the continuity equation which is expressed as a function of the transport:

$$\frac{\partial F}{\partial x} + \frac{\partial G}{\partial y} + \frac{\partial H}{\partial z} = 0 \tag{2.23}$$

Where F, G and H are the transport in each direction: F = dydzu , G = dxdzv and H = dxdyw and (u,v,w) are the three components of the velocity that are assumed to vary linearly in the x, y and z direction, respectively.

The velocity field is known on each side of a grid cell - it uses an Arakawa-C grid as CROCO - and then interpolated at the location of every particle. The position of the advected particle in the next time step is computed using the minimum crossing time, the process is repeated independently in each direction (Blanke and Raynaud, 1997). The principle of mass conservation then assures that the trajectories are continuous within the cell.

For example, in a cell extending from x = 0 to x = 1, the transport F

can be written as:

$$F(r) = F_0 + r\Delta F \tag{2.24}$$

with $r \in [0,1]$, $F_0 = F(0)$ and $\Delta F = F(1) - F(0)$.

The equation of motion (e.g. $u = dx/dt$) for the transport is:

$$F = \frac{dr}{ds} \tag{2.25}$$

Where s is called the psuedo-time and defined as $s = t/dxdydz$.

Assuming as initial condition (r,s)=(0,0) and combining equations 2.24 and 2.25, the position r is:

$$r = \frac{F_0}{\Delta F}(exp(s\Delta F - 1) \tag{2.26}$$

If $\Delta F = 0$ eq. 2.26 simplifies i: $r = F_0 s$. Similar relationships hold along the other directions.

The moment at which a particle crosses a side and switches to another cell corresponds to the moment at which r is equal to the exit value (in this example r=1).

Writing ds as $F^{-1}dr$, and substituting r, the equation for the pseudo-time becomes: $ds = (F\Delta F)^{-1}dF$. A crossing time can be obtained only if F(1) and F(0) have the same sign, which also implies that F must not be null in the cell. In case these conditions are not verified for F, the continuity

equation assures that they are going to be true for H and/or G.

If they are verified for F, s is:

$$s = \Delta F^{-1} ln(\frac{F}{F_0}) \tag{2.27}$$

When the transport reaches the exit face (r=1, F(1)), the crossing time is computed as:

$$\Delta s = \Delta F^{-1} ln(\frac{F_0 + \Delta F}{F_0}) \tag{2.28}$$

If $\Delta F = 0$ then $\Delta s = 1/F_0$.

If more than one crossing time is defined for a single cell, then, the shortest one is adopted as travelling time and used to update the positions in all directions. Computations are done for the next cell, with a starting point equal to the exit point of the previous one, and the age of the particle is regularly updated.

2.3.1 Model Set-up

The bathymetry dataset used is ETOPO1 (Amante and Eakins, 2009), a global relief model of Earth's surface that integrates land topography and ocean bathymetry, with a 1-minute ($\sim$ 1.85km) resolution. Since steep gradients in the topography and isolated seamounts can lead to numerical problems, a proper bathymetry smoothing is necessary for the stability of

the model. I performed several tests to achieve a topography that does not give rise to instability, but it is not too smooth for a realistic configuration. The geometrical parameters of the filtering procedure were progressively changed. For each variation, I checked the vorticity at the bottom of the ocean, which is a good index of the noise in the model due to possible numerical instability. Then the obtained bathymetry was interpolated over the CROCO grid. The final value of rx1 is slightly higher, of 0.3, than the recommended one of 0.2. Several tests with rx1 ranging from 0.15 to 0.35 have been performed.

The first tests were performed at a "coarse" resolution of 1/20° resolution (roughly 5km), referred to as R5. The chosen domain includes part of the east Arabian Sea that includes the Maldives, the Laccadives, the Chagos Archipelago, and the south-west coast of India, from 67°E to 79°E in longitude and from -11.6°S to 16°N in latitude (see Fig. 2.2).

The first step was a 10 years spin-up run of the R5 under climatological forcing and boundary conditions to ensure a statistically steady state in CROCO, the total kinetic energy was checked to ensure that the drift of the model was comparably small, see Fig. 2.6. The model runs with a calendar of 360 days and all months have an equal length of 30 days. Averages are written to the output for each month throughout the simulation. Then, to perform a study of the interannual variability in the region, I simulated 24 years: from 1993 to 2016. In this realistic simulation, the model runs with the true length of each month, taking also into account leap years. Averages and instantaneous fields are written every 5 days.

The second set of simulations has a higher resolution of 1/64° (roughly 1.6 km), referred to as R1.6_v2 obtained through an offline nesting using the

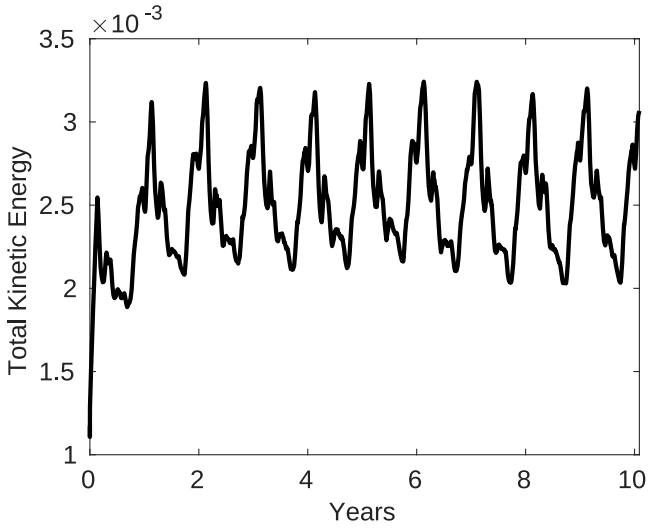

Figure 2.1: Total Kinetic Energy over the 10 years period of the CROCO spin-up.

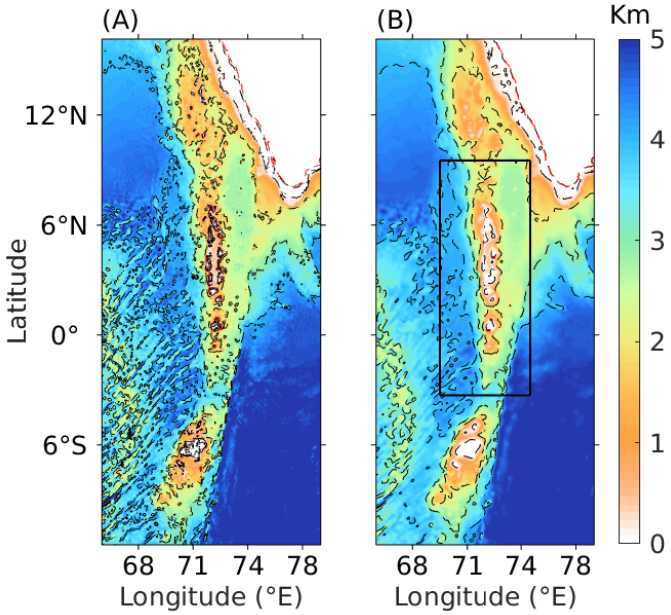

Figure 2.2: (A) Original bathymetry from Etopo1, (B) smoothed bathymetry used in the spin-up and the R5 runs. In black the isolines at 20, 100, 2000, 3000 and 4000 meters, in red the coastlines. The black rectangle delimit the area used for the R1.6 runs (Fig 2.3).

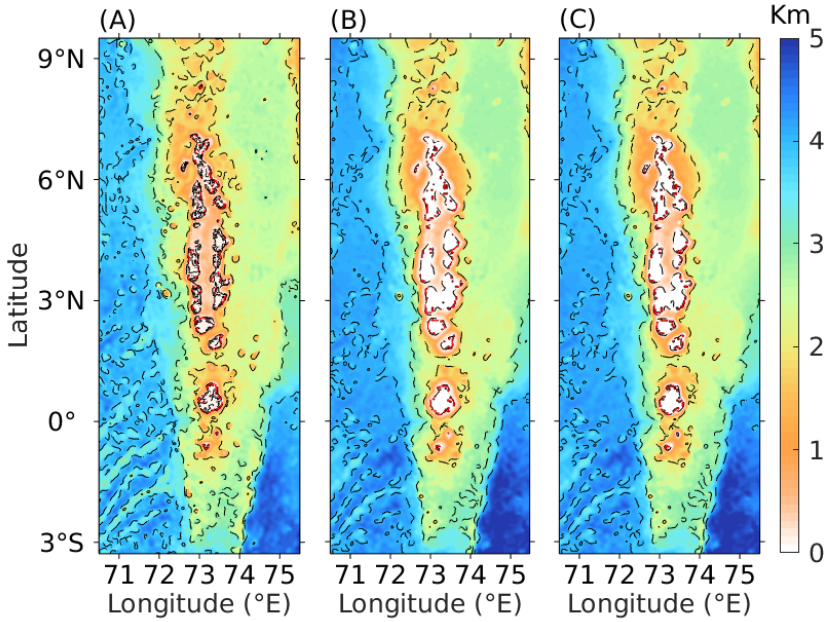

Figure 2.3: (A) Original bathymetry from Etopo1, (B) smoothed bathymetry used in R1.6 with vtransform=2, (C) smoothed bathymetry used in R1.6 with vtransform=1. In black the isolines at 20, 100, 2000, 3000 and 4000 meters, in red the coastlines.

output of the 'parent' R5 simulations. The domain is smaller, it covers the Maldivian Archipelago and the surrounding ocean from 70.5°E to 75.5°E in longitude and from 3.3°S to 9.5°N in latitude (see Fig.2.3), to better understand the ocean dynamics of the islands and the interaction between the bathymetry and the large scale circulation. The simulations are available for fewer years, from 2010 to 2016 since they are more computationally demanding. Averages and instantaneous fields are written in the output every 3 days.

Table 2.1: Parameters used for the vertical coordinates stretching

vtrasform	2	1
Run	Spin-up R5 R1.6_v2	R1.6_v1
θ_S	7	7
θ_B	3	0.5
h_c	75	15
h_{min}	20	20
N	60	60

For this second set of simulations, several tests have been performed, changing both the stretching parameters and the smoothing degree of the bathymetry. In all simulations, the second vertical stretching (vtransform=2) has been used, since it presents several advantages compared to the 'old' ones. Another set of the high resolution simulations called R1.6_v1 with the same characteristics was run with the the oldest vertical trasformation available

(vtransform 1) to be able to use Ariane to add Lagrangian tracers to the the simulated currents field. Unfortunately, Ariane only supports the first kind of vertical coordinates and not the newer version of the stretching. The two bathymetries have not relevant differences (see Fig 2.3 B,C). Averages and instantaneous fields are written in the output every 3 days and for a selected period of time every hour. All geometric parameters used are listed in table 2.1.

2.3.2 Initial, Boundary and Forcing Conditions

CROCO requires initial conditions (IC), boundary conditions (BC), and forcing. Boundary and initial conditions are taken from SODA3 (Carton et al., 2018) and the forcing comes from ERA5 (Copernicus Climate Change Service C3S, 2017). The spin-up run has been forced with monthly climatolgies from these datasets covering the period from 1993 to 2016. The BC for the R5 had a monthly frequency, for the R1.6 5days averages from R5 were used. To account for high-frequency variability, which are critical for mesoscale and sub-mesoscale processes, as well as for the vertical mixing, the forcing was every 6 hours and 1 hour, respectively for the R5 and the R1.6 (see table 2.2).

The lateral BC are open boundary conditions with the addition of a nudging layer, a layer where the model is relaxed towards external data, a nudging term is, therefore, added in both tracer and surface elevation equations. A moderate nudging is useful to prevent substantial drift of the model data towards values that are not representative of the real data (Marchesiello et al., 2001).

Table 2.2: Forcing and Boundary conditions for each run with the corresponding spatial and temporal resolution.

Run	FC	BC
Spin-up	ERA5 Spatial Resolution: 0.25° Time-Step: monthly	SODA3 Spatial Resolution: 0.25° Time-Step: monthly
R5	ERA5 Spatial Resolution: 0.25° Time-Step: 6 hour	SODA3 Spatial Resolution: 0.25° Time-Step: monthly
R1.6_v2	ERA5 Spatial Resolution: 0.25° Time-Step: 1 hour	R5 Spatial Resolution: 0.05° Time-Step: 5 days
R1.6_v1	ERA5 Spatial Resolution: 0.25° Time-Step: 1 hour	R5 Spatial Resolution: 0.05° Time-Step: 5 days

CROCO needs also forcing conditions at the surface and bottom boundary conditions for momentum and tracers. Only data for the surface boundary are provided while the bottom conditions are calculated analytically by CROCO. The model will interpolate between available records to get data at each time-step. The data include the net surface fluxes for tracers and momentum: surface u-momentum stress (τ_x), surface v-momentum stress(τ_y), freshwater flux (precipitation minus evaporation), solar radiation and the net surface heat flux:

Q_{net} = short-wave radiation + long-wave radiation + sensible heat + latent heat.

Heating/cooling occurs when the flux is positive/negative. Many years of climatological simulation may experience temperature drifting. For the spin-up run, several reanalyses have been tested: ERA-Interim (Dee et al.,

2011), ERA5 (Copernicus Climate Change Service C3S, 2017) and MERRA2 (Gelaro et al., 2017), the best results were obtained with ERA5 but the magnitude of the temperature trend was still substantial. Therefore, in order to minimize this trend, a heat restoring term has been added both to the spin-up run and the R5 runs that covers a 24 years span. This procedure helps to reduce biases in the surface forcing.

The restoring is expressed as:

$$Q_{model} \sim Q + dQdSST \cdot (SST_{model} - SST_{data}) \tag{2.29}$$

Where dQdSST is the net surface heat flux sensitivity to the SST, calculated as:

$$dQdSST = \left(\frac{\partial Q}{\partial T}\right)_{SST_{data}} \tag{2.30}$$

The surface temperature is restored to GHRSST (1/4° resolution) monthly means. Climatological averages over 1993-2016 were computed for the spin-up. The dQdSST used is from the Comprehensive Ocean-Atmosphere Data Set (COADS) (Woodruff et al., 1987).

2.3.3 Model evaluation

Before further proceeding, the model output has been validated: the obtained results were compared to the climate conditions of the region as described

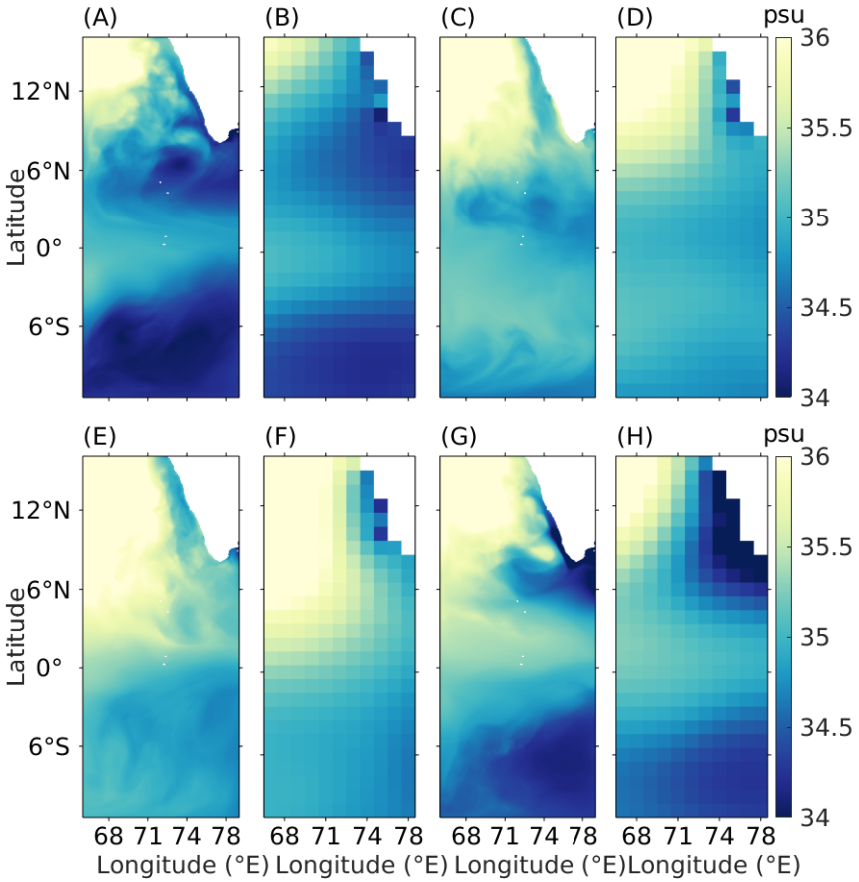

Figure 2.4: SSS from CROCO spin-up (A,C,E,G) and WOA (B,D,F,H) for December-February(A,B). March-May (C,D). June-August (E,F). September-November (G,H).

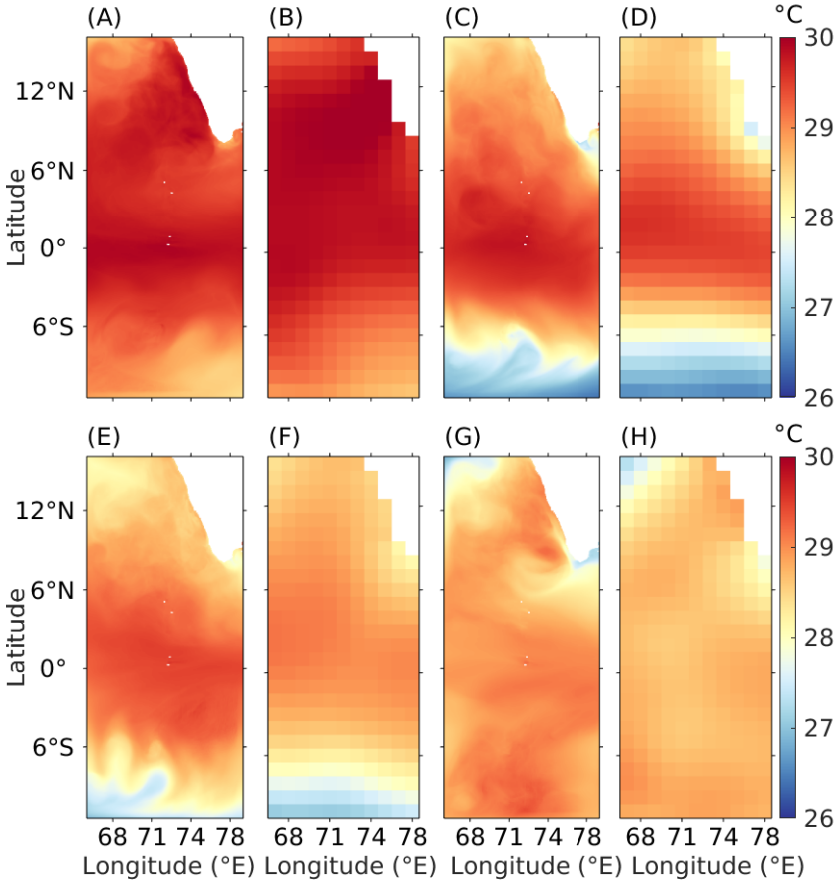

Figure 2.5: SST from CROCO spin-up (A,C,E,G) and WOA (B,D,F,H) for December-February (A,B). March-May (C,D). June-August (E,F). September-November (G,H).

by reviewed articles and satellite data. The evaluation is based on the last year of the climatological mean spin-up simulation, when the model has reached a steady state and using all years of the R5 runs.

The surface salinity (SSS) and sea surface temperature (SST) from the spin-up were compared to SODA3 and the World Ocean Atlas 2018 (WOA18). The WOA18 series includes the objectively analyzed climatological fields of in situ temperature (Locarnini et al., 2018), salinity (Zweng et al., 2018), oxygen, and other measured variables at standard depth levels for various compositing periods for the world ocean at 1/4° resolution. Several decades are available, I have used the ones covering the 1981-2010 period. The comparison of the obtained seasonal fields for SSS and SST in shown in Fig. 2.4 and Fig. 2.5 respectively. Both the temporal and spatial variability are well reproduced. The maximum value of the temperature is reached during spring. The fresh water input from the Benguela Bay, that is transported around the tip of India, is as well present.

The main features of the ocean circulation in the area are well described in the review paper of (Schott et al., 2009) as described in paragraph 1.2.1. The output of the spin-up well represents all main features of the circulation, as shown in the comparison between SODA3.3.1 in Fig. 2.6 for both monsoon periods. There is a good agreement both in the seasonal cycle and in the spatial structure of the Sea Surface Height (SSH) anomalies (panels A to D in Fig. 2.6) reproducing the positive and negative anomalies due to the Laccadive High and Laccadive Low respectively; as well as in the currents cycle and structure - panels E to H in Fig. 2.6 - well representing the reversing currents due to the monsoon circulation. The slight difference in the magnitude of the signal might be due to the different resolution

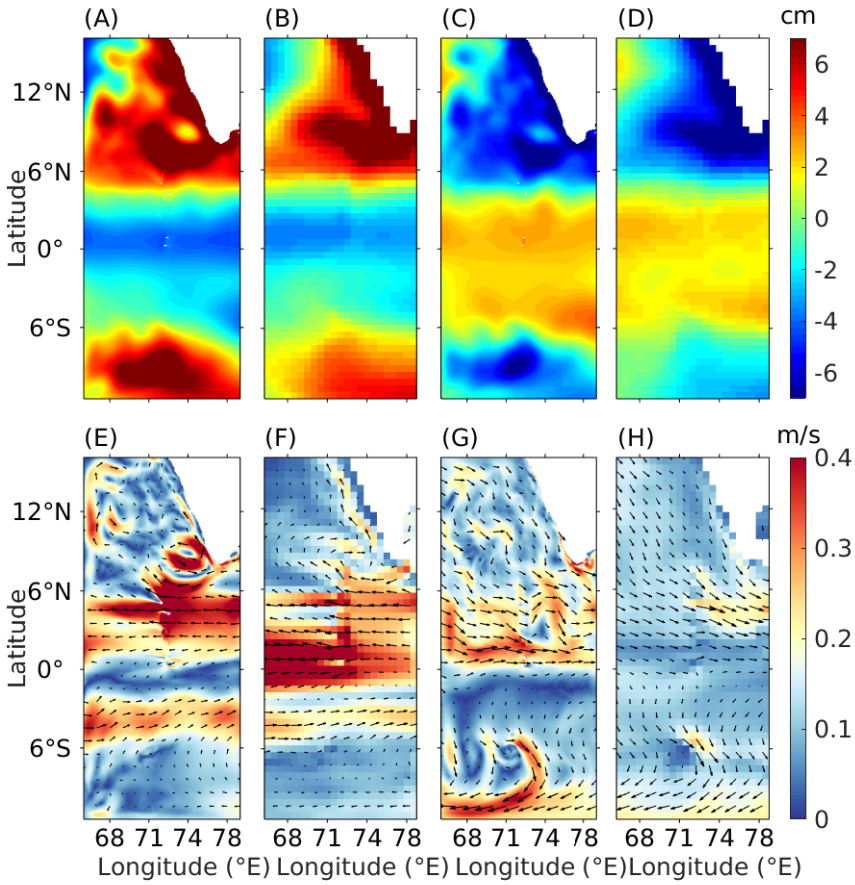

Figure 2.6: SSH and currents velocity from SODA3 (B,D,F,G) and CROCO R5 (A,C,E,G) averages over the 1993-2016. For the NE monsoon months (A,C,E,G) and the SW monsoon months (B,D,F,H).

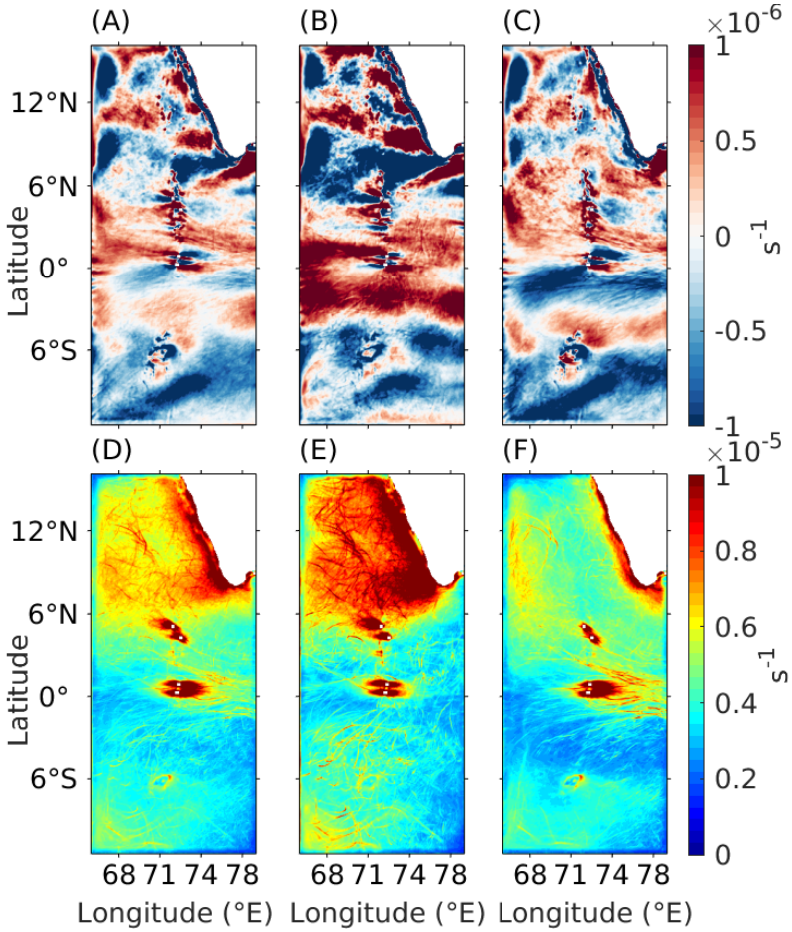

Figure 2.7: Average vorticity (A,B,C) and standard deviation (D,E,F); calculated over the whole year (A,D), the NE monsoon months (B,E) and the SW monsoon months (C,F) from CROCO R5 over the 1993-2016 period.

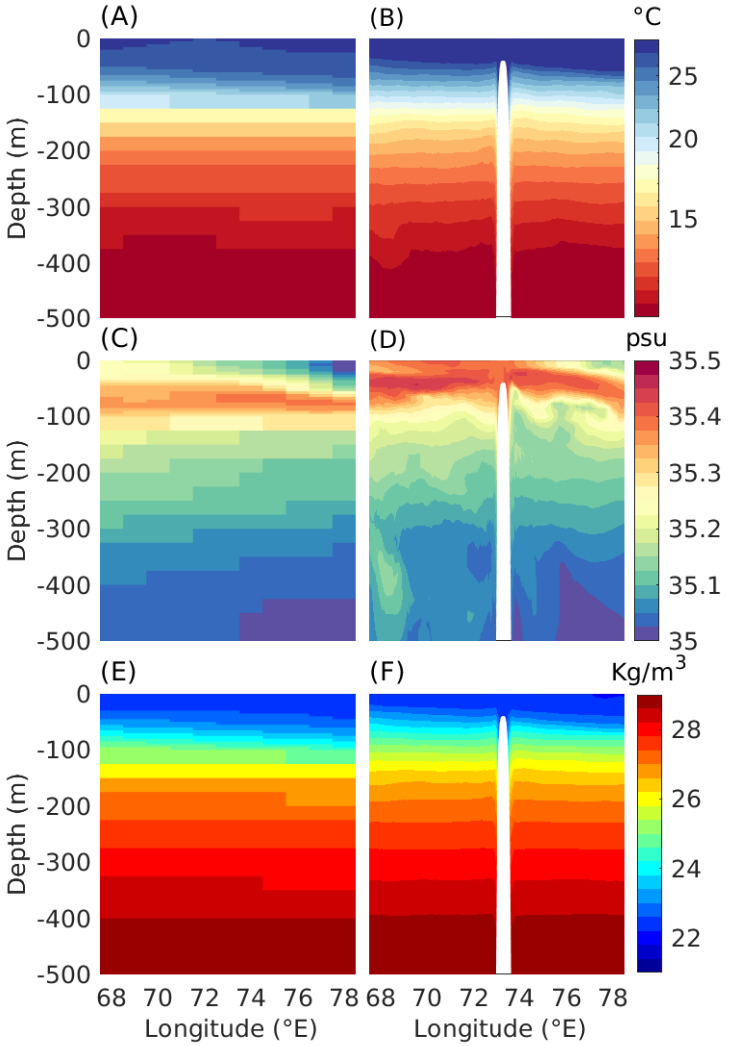

Figure 2.8: Vertical transect of temperature (A,B), salinity (C,D), and density (E,F) at a latitude of 0.5° in January from WOA (A,C,E) and CROCO spin-up final year (B,D,F).

between SODA3.3.1, ∼25 km, and the model, ∼5 km, with the second one better able to reproduce the mesoscale circulation. The seasonal cycle of the vorticity of R5 is shown in Fig. 2.7, in the northern part of the domain there is an increased eddy activity in winter, not only in magnitude as seen in the mean vorticity (Fig. 2.7,B), but also in the variability, as shown by the standard deviation of the vorticity (Fig. 2.7,E) compared to the SW monsoon. As explained in paragraph 1.3, eddy formation is enhanced in the first half of the year due to baroclinic instability associated with the presence of steep density gradients along the west coast of India (Rao et al., 2013).

Several vertical transects, for all months and at different locations, for temperature, salinity, and density (ρ) have been compared to WOA18 variables, to check that the vertical stratification was well reproduced. An example for January from the spin-up is shown in Fig. 2.8. Even in the presence of a steep sea mount (Fig. 2.8 B,D,F), all three variables show a good agreement. The seasonal cycle of the MLD from the climatology over 1993-2016 from the 5km simulations follows the same pattern as the one from WOA18 (Fig. 2.9). Even though almost all seasons show a good agreement, the magnitude of the signal in January and February is about 10 m shallower in the CROCO simulation.

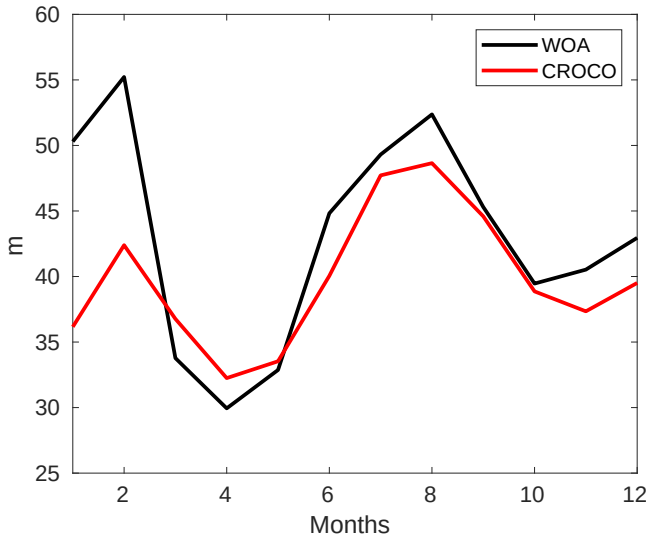

Figure 2.9: Average Mixed Layer Depth, defined as the depth at which the temperature difference with the surface is equal to 0.2°C from WOA18 and climatology over 1993-2016 from R5.

CHAPTER 3

CLIMATIC AND OCEANOGRAPHIC CONTROLS ON CORAL BLEACHING CONDITIONS IN THE MALDIVIAN REGION

The frequency of coral bleaching events has been increasing in recent decades, due to the temperature rise registered in most ocean regions. Their occurrence in the Maldivian Archipelago has been observed in the months following the peak of strong El Niño events. Bleaching has not been uniform, and some reefs have been only marginally impacted. I use satellite observations and a regional ocean model to explore the spatial and temporal variability of SSTs and quantify the relative magnitude of ENSO-related episodes with respect to the recent warming. In line with other studies, it is confirmed that the long-term trend in SST significantly increases the frequency of stress conditions for the Maldivian corals. It is also found that the interaction between currents and the steep bathymetry is responsible for a local cooling of about 0.2°C in the archipelago during the warmest season, with respect to the surrounding waters. This cooling largely reduces the frequency of mortality conditions.

3.1 Coral Reefs

Coral reefs are a hotspot of biodiversity, they occupy less than 0.1% of the ocean floor but provide a habitat for about 25% of the known marine

species (Moberg and Folke, 1999, Plaisance et al., 2011). Despite their exceptionally high biodiversity, coral reefs are vulnerable to the loss of the functionally important species (Hughes et al., 2017). Although corals exist both in temperate and tropical waters, shallow corals prefer clear, warm, moving water in subtropical and tropical seas. They form only in a zone extending from approximately 30° N to 30° S of the Equator. Tropical corals do not grow at depths of over 50 meters (Achituv and Dubinsky, 1990).

Coral reefs are a fundamental source of income for the local population, through fishery and tourism. The staggering biodiversity is an important source of medical advances, helping with the development of new pharmaceuticals. Corals are the main reef building organism: each individual coral is referred to as a polyp. Coral polyps live on the calcium carbonate exoskeletons of their ancestors, adding their own exoskeleton to the existing coral structure, providing biogenic sediments that help fight erosion and sea level rise. They provide coastal protection from storms and waves. They break 97% of the energy of waves (Ferrario et al., 2014), of key importance for an atoll nation as the Maldives, with an average altitude over the sea level of about 5 m.

Whether the ability of coral reefs to provide these essential services will continue in the future, however, is uncertain. Warming of ocean waters, acidification, overfishing, pollution, and damage from coastal development constitute local and global threats that jeopardize the sustainability of reef systems. Most of the reefs are projected to disappear in a few decades by the 2050 (Hoegh-Guldberg et al., 2017).

The Maldives increase in SSTs is the most pressing danger (Pisapia et al., 2019, 2016). The Indian Ocean is the ocean that have warmed the

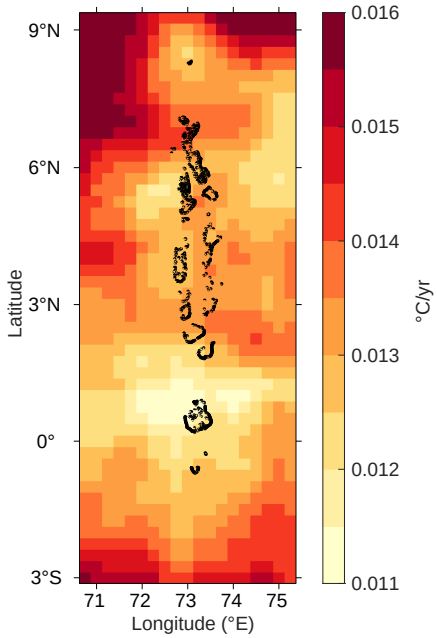

Figure 3.1: Annual trend of the temperature from 1982 to 2018, from GHRSST data, at 25km resolution.

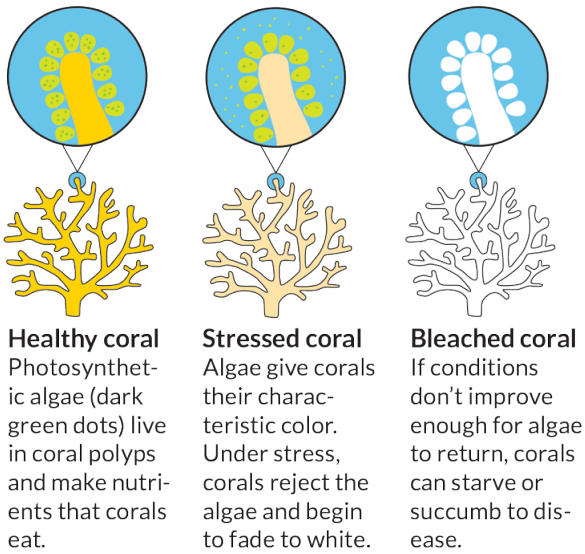

Figure 3.2: Infographic about coral bleaching from the National Oceanic and Atmospheric Administration (NOAA) Coral Reefs Conservation Program.

most in the last 50 years (Dhame et al., 2020). The increase of temperature over the Maldives Archipelago has been, on average, of about 0.5°C, with values comprised between 0.4 and 0.65°C (see Fig. 3.1).

Whenever SSTs exceed climatological values by 1 or 2^{o}C in the warmest season for a sufficiently long time, reef-building (sclearctinian) corals expel their symbiotic algae, with consequent bleaching and often mortality. Usually, coral polyps live in an endosymbiotic relationship with an algae, which is crucial for the survival of the coral, providing, through photosynthesis, nutrients that account for up to 90% of the coral's energy (Dove and Hoegh-Guldberg, 2006). The algae also provides the coral its beautiful colors,

once expelled, the exoskeletons become visible and the corals turn white. Bleached corals are not dead but they are more vulnerable to diseases and, if the symbiosis is not reestablished fast enough, they will starve (see Fig. 3.2). Although corals exist across large latitudinal and seasonal gradients in temperature, their thermal tolerance or bleaching thresholds are typically only 1–2^{o}C above their local maximum summer temperatures. Making them extremely vulnerable to increasing SSTs and the more frequent marine heatwaves (Safaie et al., 2018). Even under favorable conditions, it can take decades for severely bleached reefs to fully recover (Liu et al., 2014a).

In the Maldives, these prolonged periods can occur in the period between April and June, usually following peak positive El Niño Southern Oscillation (ENSO) conditions in the tropical Pacific (Ibrahim et al., 2017, Pisapia et al., 2016, Schuhmacher et al., 2005, Zahir et al., 2009). The two most recent bleaching events during which coral mortality rates well above 50% were recorded at most sites occurred in 1998, when little monitoring was in place, and in 2016, when a more careful assessment was possible (Ibrahim et al., 2017, Zahir et al., 2009). In the decade following the 1998 bleaching event, most of the Maldivian coral reefs recovered to pre-1998 levels of coverage, with some changes in composition towards more temperature resilient species (Morri et al., 2015). The recovery level was higher and faster than in other sites in the Indian Ocean. Various factors may have contributed to this nearly complete recovery, including elevated biomass of herbivorous fish on reefs that are not targeted by local fishermen (McClanahan et al., 2011, Risk and Sluka, 2000), large connectivity among sites (Naseer and Hatcher, 2004), overall pristine conditions of most of the islands and atolls, with still limited anthropogenic pollution and eutrophication compared to other regions (Ibrahim et al., 2017), and the existence of refuges or sites where

corals survived through bleaching events and repopulated the surrounding reefs. The presence of refuges was clearly observed during the 2016 events, where some reefs, or *hope spots*, reported bleaching only to 25% or less of their area, despite a much greater (up to 100%) decline in live coral coverage at other sites (Ibrahim et al., 2017).

In this work, I use satellite and reanalysis products and a regional ocean model to explore the possibility of physical drivers contributing to the patchiness of bleaching events, and therefore to the presence of these *hope spots*, in the Maldives, and to evaluate how the predicted warming may modify the likelihood of coral bleaching in the next few decades. While recognizing that many factors other than physical may contribute to the observed differences among sites, and that products from satellites may not have sufficient resolution to resolve scales small enough to distinguish clearly between specific sites, I wish to explore how and where ENSO events, both positive and negative, may modify the strength and duration of SST anomalies, and how the ocean circulation influences the distribution of ocean temperatures in one of the most pristine marine biodiversity hotspots on the planet.

3.2 Data and Methods

The SST data set of choice in this work is the Group for High Resolution Sea Surface Temperature (GHRSST) Level 4 (National Centers for Environmental Information (NOAA), 2016), available over the period 1982 - 2018 with daily temporal 0.25°spatial resolution. I performed a more detailed analysis of the years 2013 and 2016 using a version of GHRSST at higher

spatial resolution (0.054°), available from April 2006 (UK Met Office, 2005).

To better understand the patterns of SST revealed by this analysis, I conducted a numerical investigation using the R5 simulation from CROCO for a neutral ENSO year (2013).

The analysis has been performed on two domains in the Indian Ocean; one covers the Maldivian Archipelago and the surrounding ocean, from 70.5°E to 75.5°E in longitude and from 3.3°S to 9.5°N in latitude, while the second is restricted to the atolls, from 72.5°E and 74°E in longitude and from 0.5°S to 7.5°N in latitude (see Fig. 3.3).

3.2.1 Degree Heating Period

If given enough time (order of years or longer), corals can acclimatise and adapt to slightly different conditions (Guest et al., 2012, Maynard et al., 2008, Penin et al., 2013). This implies that coral bleaching does not happen at a fixed temperature at all times or locations. The local temperature threshold to define a potential stress for corals is typically based on the maximum monthly mean temperature (MMM). The US National Oceanic and Atmospheric Administration (NOAA) defines as HotSpots (HS) the daily temperature anomalies above MMM. Corals are considered to be thermally stressed at temperatures 1°C or more above MMM, e.g. HS≥1°C (Chaudhury et al., 2019, Glynn and D'Croz, 1990, Lough, 2011):

$$HS = SST_{daily} - MMM \tag{3.1}$$

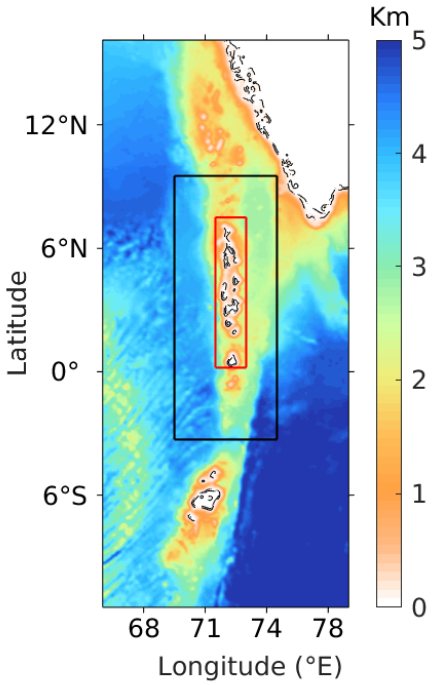

Figure 3.3: Smoothed bathymetry used in the CROCO R5, with 50 and 100 m contour lines. The inner boxes identify the analysed domains.

The extent of bleaching depends not only on the temperature maxima but also on the temporal persistence of the thermal stress (Lesser, 2011). To account for both the magnitude and the duration of the stress, the metric "Degree Heating Period" (DHP) is introduced. It is computed at any given time by integrating HS of 1°C or greater over the preceding 12 weeks:

$$\mathrm{DHP}(t) = \int_{t-84\mathrm{days}}^{t} \mathrm{HS}(t')\ \mathcal{H}(\mathrm{HS}(t') - 1^o\mathrm{C})\ dt', \tag{3.2}$$

where $\mathcal{H}$ is the Heaviside function. Operationally, the integral operator is replaced by a summation, as temperature is typically available as a discrete time series: for daily temperatures, for instance, defining δt =1day the DHP becomes

$$\mathrm{DHP}(t_i) = \Sigma_{i-83}^{i} \mathrm{HS}(t_i)\ \mathcal{H}(\mathrm{HS}(t_i) - 1^o\mathrm{C})\delta t. \tag{3.3}$$

Depending on the units used to express it and the HS stress threshold used, this metric appears in the literature with the name of Degree Heating Days (expressed in °C day) (Maynard et al., 2008) or Degree Heating Weeks (expressed in °C-week) (Liu et al., 2014a).

Values of DHP above 4°C-week and 8°C-week are representative of bleaching and mortality conditions, respectively (see table 3.1).

The use of a threshold-based metric has been criticised (McClanahan et al., 2019). However it remains widely implemented and provides useful information (Hughes et al., 2017, Ibrahim et al., 2017, Kayanne, 2017, Liu

Stress Level	Definition	Ecosystem Impact
No Stress	HS≤0	-
Bleaching Watch	0<HS<1	-
Bleaching Warning	1≤HS | 0<DHP<4	Possible Bleaching
Bleaching Alert Level 1	1≤HS | 4<DHP<8	Bleaching Likely
Bleaching Alert Level 2	1≤HS | 8≥DHP	Mortality Likely

Table 3.1: NOAA coral reefs bleaching monitoring thresholds (Liu et al., 2006)

et al., 2014a, Lough et al., 2018, e.g.).

3.2.2 ENSO years

Considering that bleaching in the Maldives occurs during strong El Niño years, the analysis is performed by taking into account the ENSO cycle. For this purpose, we use the Oceanic Niño Index (ONI). The ONI tracks the running 3-month average SST in the Niño3.4 region, located in the tropical Pacific between 120°E-170°E and 5°S to 5°N.

Considering that the onset of El Niño is typically at the end of the year, and that its warming impact on the Indian Ocean temperatures peaks in April-May (Schott and McCreary, 2001), we define ENSO years as the twelve months from October to September. ENSO+(-) years are those with five consecutive 3 months running means with a temperature anomaly

ENSO+		ENSO-	
1986-1987	2006-2007	1984-1985	2005-2006
1987-1988	2009-2010	1988-1989	2007-2008
1991-1992	2014-2015	1995-1996	2008-2009
1994-1995	2015-2016	1998-1999	2010-2011
2002-2003		1999-2000	2011-2012
2004-2005		2000-2001	

Table 3.2: ENSO+ (El-Niño) and ENSO- (La-Niña) years, defined from October to September.

higher that 0.5°C (lower than -0.5°). The studied years, between 1982 and 2018, have been divided into ENSO+ (El-Niño), ENSO- (La-Niña), and Neutral years (see table 3.2).

3.3 Results

3.3.1 Interannual variability of coral bleaching conditions

The amplitude of the climatological seasonal cycle of sea surface temperature in the study region is less than 2°C (see Fig. 3.4), and the surface MMM is in April. From the onset of the summer monsoon, at the end of May, the extensive cloud cover reduces the solar radiation that reaches the ocean surface inducing a SST reduction in the region (Dey et al., 2015, Roy et al., 2014). The spatial structure of the surface MMM is shown in Fig.3.5A, with values locally varying between 29.5°C in the south and 30°C in the north of the domain. Coral bleaching occurred, so far, in the warmest season, from March to May, and in association with strong El Niño events (Chatterjee

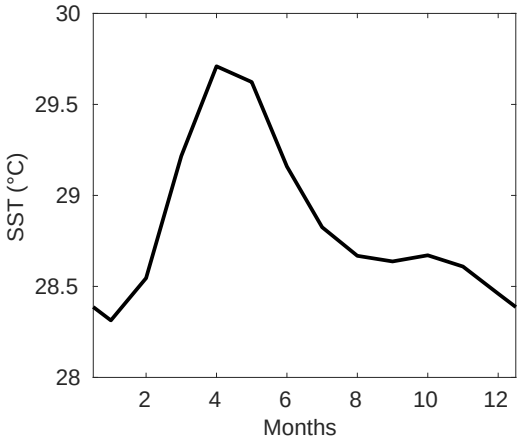

Figure 3.4: Climatological (1982-2018) seasonal cycle of the SST averaged over the domain from GHRSST

et al., 2012, Ibrahim et al., 2017, Wilkinson, 2008, Zahir et al., 2009).

The maximum daily SST has a strong correlation with the peak of the annual ONI value that, in the considered period, always occurs in the preceding winter; with local correlation coefficients varying between 0.45 in the equatorial region to 0.84 in the northern latitudes (Fig. 3.6).[1]

Figure 3.5B shows the linear regression of the maximum daily SST during the March-May period onto the maximum ONI index. During years

[1]I verified that the influence of the Indian Ocean Zonal Mode or Dipole, the other major mode of climate variability in this region (Edwards et al., 2001, Saji, 2018), on the SST is negligible in April-May: it interests only the coolest season of the year, from September to November, and is therefore unrelated to bleaching events.

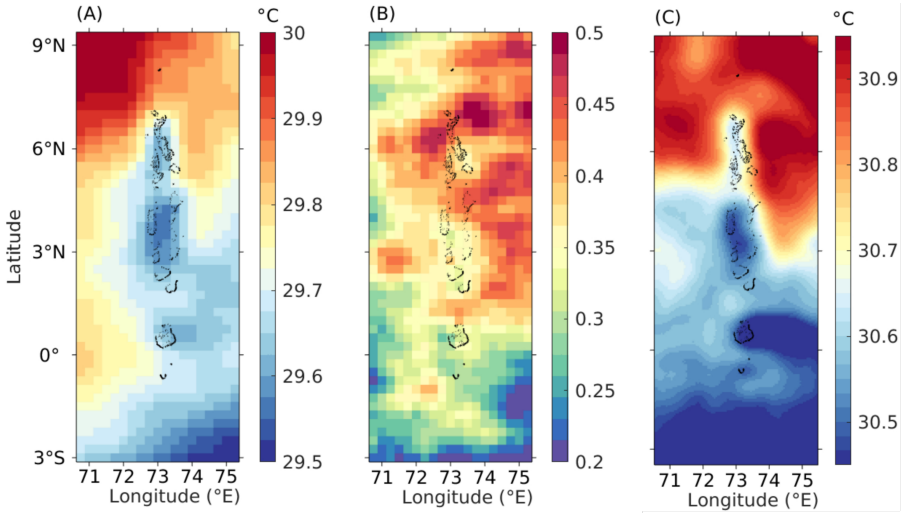

Figure 3.5: (A) Map of maximum monthly mean surface temperature averaged over the period 1982 - 2018; (B) linear regression coefficient of April-May maximum daily surface temperatures on maximum annual ONI for the 1982 - 2018 interval; (C) mean April-May SST in 2016 following the 2015 El-Niño. GHRSST data have been used at 25 km resolution for panels A and B and at 5 km resolution - the same used later in the model run - for panel C.

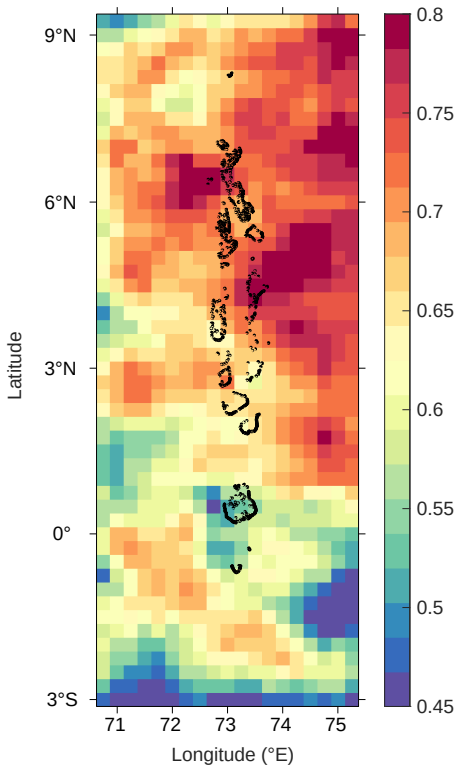

Figure 3.6: Correlation coefficient of April-May maximum daily surface temperatures on maximum annual ONI for the 1982 - 2018 interval.

with peak ONI values of 1°C, the local difference between March-May peak daily surface temperature and its mean value varies from 0.2°C near the Equator to 0.5°C on the north-eastern corner of the domain. Three relative minima are present over the Archipelago, with ENSO related temperature variability smaller near the atolls and in the shallow inner sea, and larger over the deep passes among the islands (see Fig. 3.3). In the surface MMM map and in the ENSO-SST regression map, waters around the Maldivian archipelago are characterized by climatological temperatures and ENSO impacts somewhat smaller compared to the surrounding areas. These maps suggest a role for the physical circulation at the atolls in controlling the temperature anomalies that will be discussed later on.

The patchiness in Fig. 3.5B is further highlighted in Fig. 3.5C that shows the warming patterns following the 2016 El-Niño in April and May. The warming caused by the 2016 event was more intense in April and less so in May, while in 1998 the opposite was verified (see Fig. 3.12 panels A to D).

Interestingly, the 2016 satellite data hint to the possibility of *hope spots* in the Faafu, South Ari and Baa atolls (Fig.3.7) where indeed 7 of the 8 reefs with high potential of surviving the bleaching event were sampled (Ibrahim et al., 2017). The southern atolls, Gaafu especially, show conditions that are similar or even more promising. Unfortunately, the scarcity of surveys in these atolls precludes the possibility of an adequate assessment of local reefs conditions (Ibrahim et al., 2017).

Focusing on the interannual variability of the upper ocean conditions, we compute probability density functions (PDFs) of April and May temperatures over the whole study area and over the box covering only the

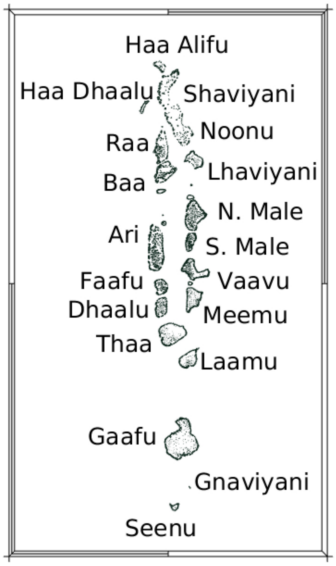

Figure 3.7: Map of the Maldives Archipelago

atolls, separately for ENSO+, ENSO- and ENSO neutral years. The PDFs (Fig. 3.8) indicate that the largest differences between the three clusters of years are in the warm tail of the distributions. During ENSO- (La-Niña) years, the probability of occurrence of low temperatures (T<29°C) is nearly unchanged compared to neutral years, while chances of high temperatures (T>30°C) are suppressed (Fig. 3.8a).

During ENSO+ (El-Niño) years, the whole distribution is wider and is significantly displaced to higher temperatures. This asymmetric behavior (e.g. El-Niño - La-Niña differences being relatively small at low temperatures and large at high temperatures) can be explained by the fact that over this domain, there is an anti-correlation between the depth of the mixed-layer and the SST, with colder (warmer) surface waters being associated with a

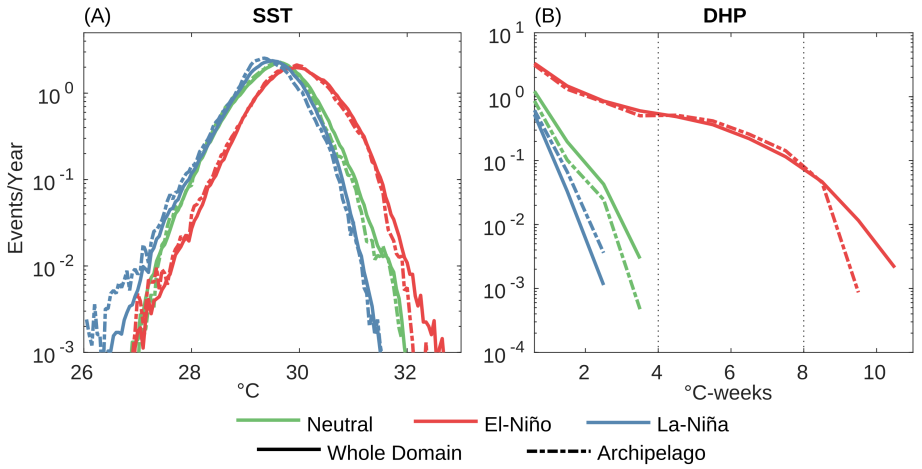

Figure 3.8: Sea surface temperature distributions for the month of April from GHRSST (panel A). Distribution of the degree heating period conditioned to days with HS (Hot Spots) temperature greater than 1°C in the satellite data (panel B).

deeper (shallower) mixed layer (see Fig. 3.9).

The mixed layer in the warmest months (April-May) is shallower during ENSO+ years than in the 1980-2016 climatology (see Fig. 3.10A).This difference results in part from a strengthening of the heat flux into the Ocean (Fig. 3.10B), and also from the weakening of the winds over the Maldives (Fig. 3.10C) during ENSO+ years. An anomalous air-sea heat flux that warms the ocean in an El Niño year, when surface temperatures tend to be higher and the mixed-layer shallower than climatological values (see Fig. 3.10A), is distributed over a thinner layer and generates a larger temperature increase. On the other hand, anomalous air-sea fluxes leading to ocean cooling are distributed, during any year, over a deeper mixed-layer

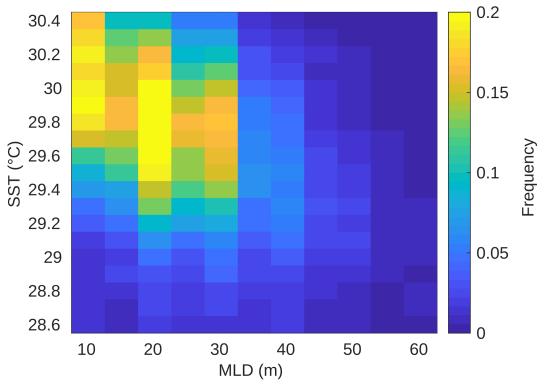

Figure 3.9: Mixed Layer Depth and corresponding temperature (at 5 m depth) 2 variable distribution, from SODA3.3.1 for the period 1980–2016 at a spatial resolution of 0.25°and at a temporal resolution of. 5-day averages

generating a smaller temperature decrease (see Fig. 3.11).

The PDFs (Fig. 3.8) further highlight that the impact of ENSO+ events is reduced near the islands, with a lower probability of reaching 32^oC around the atolls with respect to the open ocean.

To further quantify the thermal stress on corals linked to ENSO episodes, we compute the average number of days per year with local HS value larger than 1°C. Results, computed for ENSO+, ENSO-, and neutral years and then spatially normalised, are shown in Table 3.3.

For instance, the value of 1.0±0.3 found in GHRSST for ENSO neutral conditions indicates that on average each pixel within the domain experiences thermal stress for 1.0±0.3 days per year. During El Niño years, this value increases to 5.1±1.6 days/year, while during La Niña years it decreases to

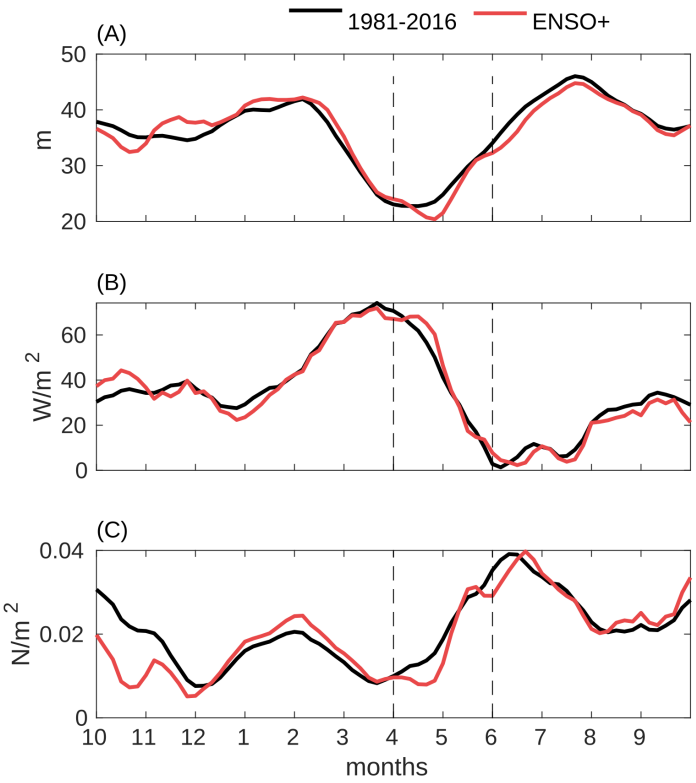

Figure 3.10: (A) 20-days running mean of the climatological seasonal cycle of the mixed Layer Depth (MLD) from SODA3 for all the available year and only the El-Niño years. (B) 20-days running mean of the climatological seasonal cycle of the net heat flux from SODA3 for all the available year and only the El-Niño years.(C) 20-days running mean of the climatological seasonal cycle of the surface wind stress from SODA3 for all the available year and only the El-Niño years. The shallower mixed layer in April and May during ENSO+ years shown in panel a is due both to slightly stronger heat fluxes (B) and weaker wind stress (C).

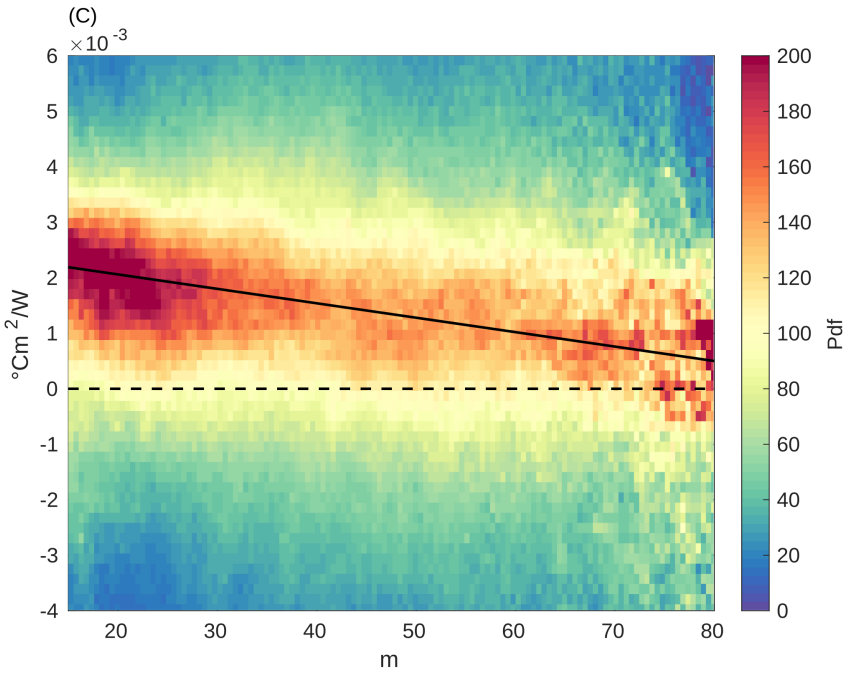

Figure 3.11: Probability density functions of the temperature at 5m change normalized by the heat flux, as function of the mixed layer depth, from CROCO simulation. The peak of the distribution moves to smaller thermal variations for deeper mixed layer. The solid line is obtained from the linear regression of the points corresponding to the peak of frequency for each MLD bin; the dashed horizontal line indicates a null thermal variation.

	HS>1°C		DHP>4°C-weeks | HS>1°C	
	AM±MSE	**HM**	**AM±MSE**	**HM**
Neutral	0.97±0.31	0.3	0	0
ENSO+	5.1±1.6	3	1.2±0.5	0.8
ENSO-	0.25±0.06	0.1	0	0

Table 3.3: Number of days per year with HS >1°C (left column) and with simultaneous DHP >4°C-weeks and HS >1°C (right column), from GHRSST dataset. Arithmetic Mean (AM) ± Mean Standard Error (MSE) and Harmonic Mean (HM) are shown, separately for neutral years, ENSO+ and ENSO- years.

0.25±0.06 days/year. No significant differences are found between the whole domain and the small box, despite the warm tail of ENSO+ distribution being lower over the atolls (Fig. 3.8A).

Considering that an isolated occurrence of a daily HS>1°C is typically well borne by corals, while it can lead to bleaching if significant thermal stress occurred over the preceding weeks, we focus on the simultaneous occurrence of large values of DHP and HS>1°C. The PDFs of DHP conditioned on HS>1°C are shown in Fig. 3.8b. Both bleaching threshold (DHP=4°C-week) and mortality threshold (DHP=8°C-week) have been reached in at least one El Nino year during the analysed period of 1982-2018, while these values never occurred during non El-Niño years (see also Table 3.3).

Mortality conditions, corresponding to the extreme DHP values from 8 to 10 in Fig.3.8b, are less frequent over the small box comprising only the Archipelago. During ENSO+ years, the chances of reaching mortality

conditions drops by 84% in the small box compared to that in the whole domain.

The analysis of the patterns of SSTa during two strong recent El Niño events (see Fig. 3.12), indicates that the warming temperature trend (see Fig. 3.1) may be already impacting the Maldives coral reefs. At face value, the 2016 anomalies were as strong as in 1998, and indeed the two bleaching events were of comparable severity (Eakin et al., 2019, Pisapia et al., 2019). However, if the anomalies are computed after removing the multidecadal linear SST trend of 0.012°C/year, which is the lower bound estimate from the 1982-2018 period, then they are significantly larger in 1998 around the Maldivian archipelago (see Fig. 3.12C,D). This suggests that the mortality of spring 2016 was exacerbated by the basin-wide, global ocean warming. Based on this analysis, it might be expected that coral bleaching, historically present only following strong ENSO+ events, could occur more regularly. This statement does not account for coral adaptation and assumes that the threshold temperature conducive to thermal stress remains fixed.

3.3.2 Physical control of spatial temperature patterns

As mentioned earlier, the MMM in Fig. 3.5A has a latitudinal dependence with lower values south of the Equator, and larger values at the northern atolls . On top of this latitudinal structure, there is a clear minimum near the Maldives, where the temperature is lower than in the surrounding areas by about 0.2°C during the warmest months. This pattern is reflected also in the regressions with the ONI index and in the PDFs (Fig. 3.5B and Fig. 3.8). The reduced temperatures over the Maldives are visible in all analysed

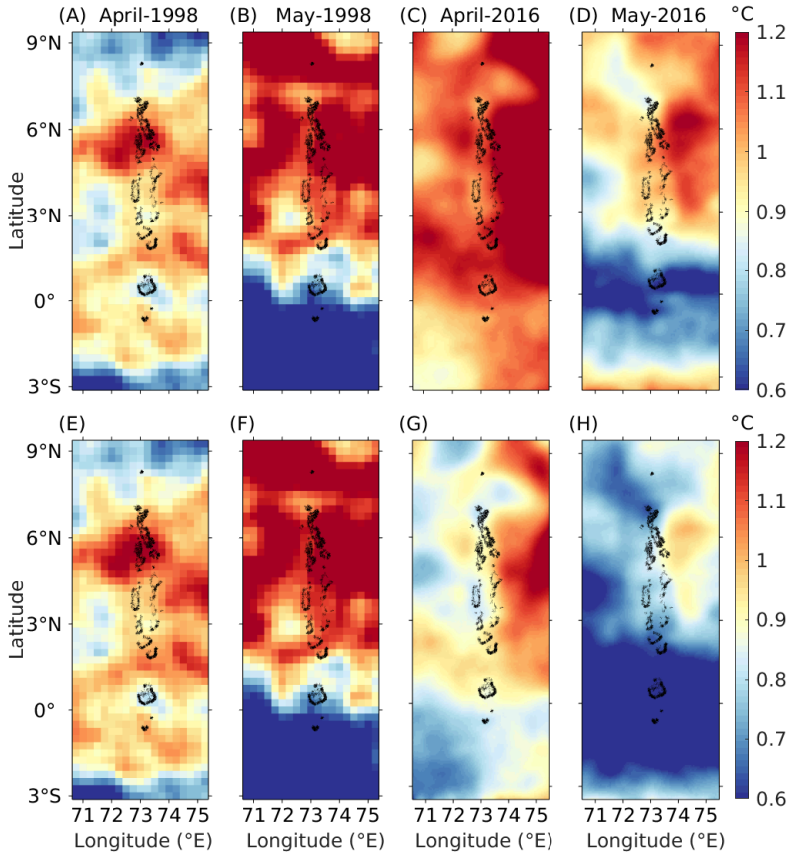

Figure 3.12: GHRSST SSTa (obtained as SST departures from local MMM) for April and May 1998 and 2016 in panel (A-D) and the same SSTa detrended with the 0.3^{o}C warming trend (E-G). At a 25km resolution for the 1998 (A,B and E,F) and 5km resolution for the 2016 (C,D and G,H).

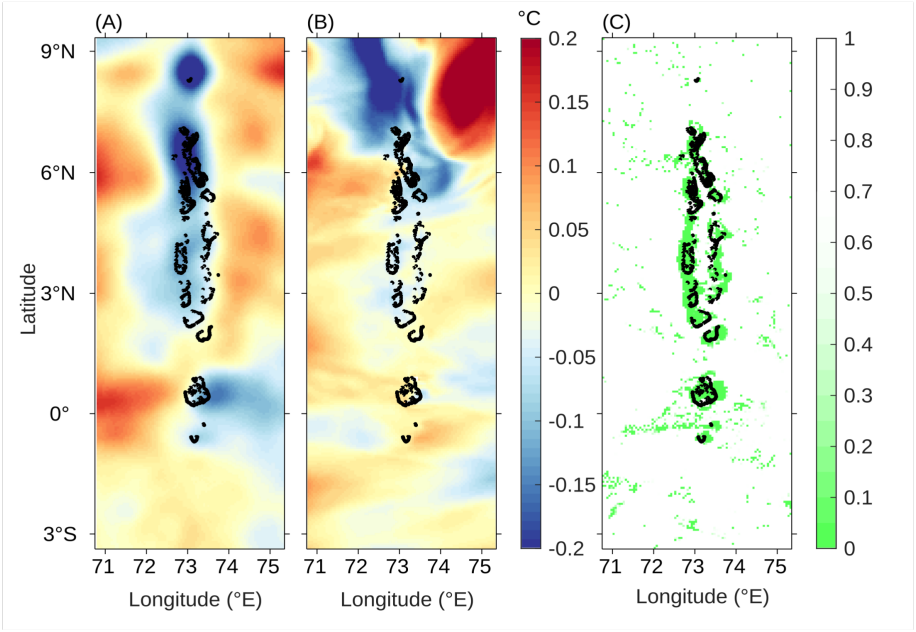

Figure 3.13: SST anomalies with respect to the zonally averaged monthly mean temperature in April and May 2013, from (A) GHRSST and (B) CROCO simulation. (C) Annual mean of the minimum of the Richardson number between 20 and 50m, an indicator of mixing at the base of the mixed layer, from CROCO simulation.

years. Figure 3.13A, for example, shows the April-May mean SST anomaly with respect to its zonal (longitudinal) mean in 2013, a neutral year with respect to ENSO. The atmospheric heat fluxes do not display any cooling over the Maldives, suggesting that the cooling has an oceanic origin.

To better understand the dynamical processes involved, we simulated the ocean circulation in and around the Archipelago, focusing on the year

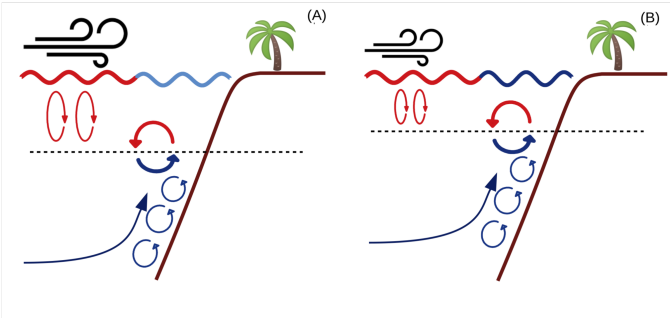

Figure 3.14: A schematic representation of the effects of mixing in the upper ocean for two mixed layer depths: (A) When the mixed layer is deeper, the cooling from below is distributed over a greater volume of water, and the resulting decrease of temperature has a lower magnitude than in case (B), when the mixed layer is shallower and the volume of water involved in the process is smaller, resulting in a stronger surface temperature reduction.

2013, using CROCO. Results are shown in Fig. 3.13(B,C). Even though the magnitude of the temperature signal in R5 is smaller that than in the satellite data, the cooling increases with depth, showing that the physical processes involved are well represented in the model.

Mixing enhancement around the islands is present year-round (see Fig. 3.13,C), with varying intensity and geographic distribution depending on the strength and direction of the currents. Averaged over the whole archipelago, the thermal signal of upper-ocean mixing is greatest in March–May as seen in the SSTs (see Fig. 3.15). In these months, the mixed-later depth is shallowest (see Fig. 3.16), due to weaker winds during the transition period between the monsoons, and the impact of mixing from below is easily detected at the surface (see Fig. 3.14).

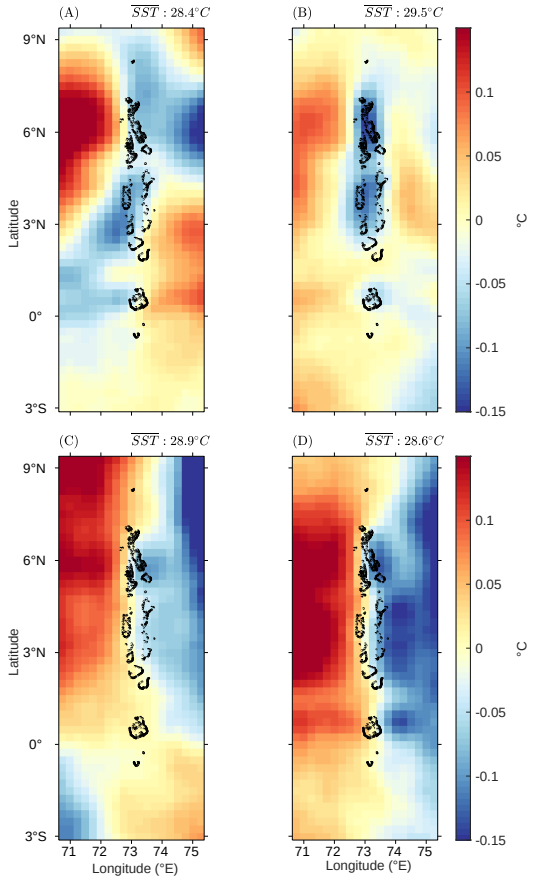

Figure 3.15: SST anomalies with respect to the zonal (latitudinal) mean from GHRSST (25 km horizontal, daily temporal resolution) 1982-2018. In the top right corner the mean SST of each period averaged over the domain. (A) December-February. (B) March-May. (C) June-August. (D) September-November.

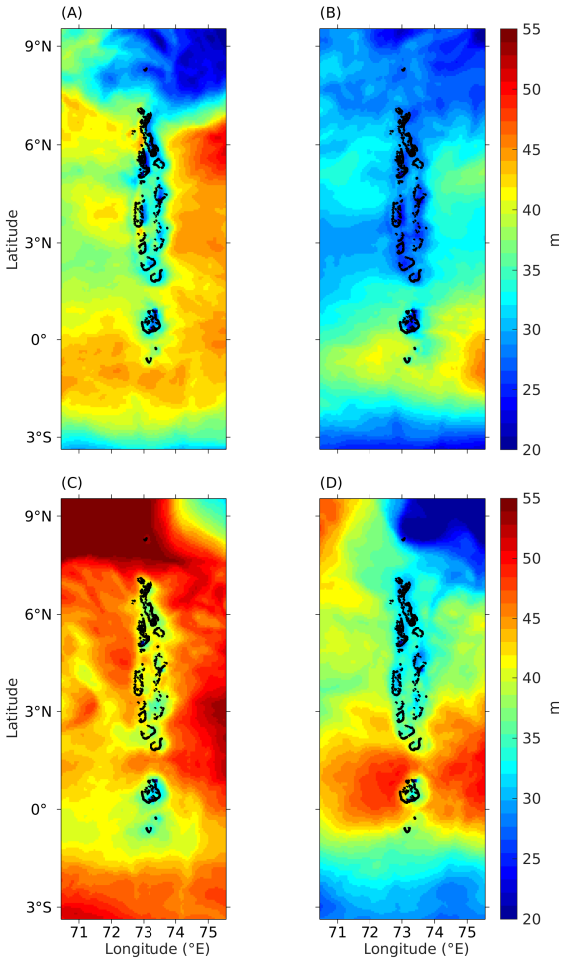

Figure 3.16: Mixed layer depth annual cycle from CROCO simulation. (A) December-February. (B) March-May. (C) June-August. (D) September-November.

3.4 Conclusions

Before the 1980s, bleaching events were registered in the Maldives only on local scales (Hughes et al., 2018). Since then, however, the anthropic pressure on coral reefs has been increasing (Anthony et al., 2008, Brierley and Kingsford, 2009, Brown and Cossins, 2011, Dove et al., 2013, Hughes et al., 2003). In particular, the SST warming following the two strongest El Niño episodes of the past 3 decades caused widespread bleaching in April and May of 1998 and 2016.

After the 1998 bleaching episode coral recovery was faster than in other regions of the Pacific Ocean, and in 2016 several *hope spots* were found, in which bleaching affected 25% or less of the colonies. Both observations point to the existence of patchy impacts that cannot be easily explained in terms of biological drivers alone. Most of the atolls are indeed in pristine conditions relative to many others at similar latitudes (Ibrahim et al., 2017) and are not subject to an overwhelming pressure from stressors common to tropical coral assemblages such as overfishing, coastal development, or pollution. Exceptions to this statement were observed in the years prior to 2016 limited to the Central Maldives, where some reefs were found moderately affected by outbreaks of crown-of-thorns starfish and sediment inputs (Pisapia et al., 2016).

El-Niño related increase in temperature is the most important global factor that leads to mass bleachings. How much a single reef is impacted by this world-wide event strictly depends on regional biological and physical processes. Environmental and background climate conditions influence the temperature at which a bleaching event can occur (Carilli et al., 2012).The

diverse response of corals to a strong El-Niño event remains an active research area. Both local radiative budgets, temperature differences and each species resilience and recovery abilities, as well as the frequency of heat waves in the considered area, should be considered. For example, it has been seen that corals have an increased ability to resist and recover after a severe thermal stress event in ocean regions characterized by high-frequency variability and large temperature swings (Carilli et al., 2012, Thompson and van Woesik, 2009). On the other hand, reefs subjected to anthropogenic stressors such as overfishing and pollution tend to have reduced recovery abilities (Richmond et al., 2018, Wooldridge, 2009).

In this work, I explored the possibility that physical drivers may partially justify the observed patchiness. I found that indeed the warm SST patterns recorded in 1998 and 2016 did not have the same structure, and that the one recorded in 2016 may explain why some atolls were spared in part. Through this analysis, I also noticed that the ocean immediately surrounding the islands is characterised by temperatures on average lower than its open counterpart by about 0.2^oC in the spring season, when bleaching occurs. These cool anomalies - with reference to the latitudinal mean - persist also during El Niño, potentially limiting its catastrophic impact on the reefs: they likely contribute to the existence of *hope spots* and reduce the maximum values of temperatures at which the corals are exposed during bleaching events.

Using a regional ocean model, CROCO, I found that these patches emerge due to the mixing associated with the strong shear around the bathymetry of the islands. The currents near the ocean surface have to slow down when intersecting the steep sea floor. The shear that is consequently

generated enhances the vertical mixing, bringing colder water from below into the mixed layer. If the mixed layer is sufficiently shallow, the colder water can imprint the ocean surface and lead to local cooling. If the mixed layer is deeper than about 30 m, and the winds are strong enough to sustain it, then the signal is not detectable near the surface, and the impact of the mixing from below on the SST is negligible. The first situation is representative of the period from February to May, and the second of the rest of the year. The stronger the zonal (latitudinal) component of the near surface currents, the stronger is the shear and therefore the vertical mixing.

The model resolution implemented, 5 km in the horizontal, is not sufficient to delve into the strength and local distribution of this mechanism across and within the atolls.

So far, the coral reefs of the Maldives have been spared from complete bleaching despite the strong positive temperature trend in the Indian Ocean. Their recovery has also been quicker relative to that of other places. The pristine conditions of most of the islands and their proximity have likely contributed. Here I have shown that the specific current-mixed layer depth conditions and their interactions with the bathymetry could have also played a role.

CHAPTER 4

UPWELLING SIGNATURE AROUND SMALL OCEANIC ISLANDS AND THE CASE OF THE MALDIVES ARCHIPELAGO

The phenomenon of enhancement in the primary productivity around islands (see Fig. 4.1) has been reported since the late fifties and called Island Mass Effect (IME)(Doty and Oguri, 1956), yet much remains unknown about the prevalence and drivers of this ecologically important event (Gove et al., 2016). It refers to a spectrum of biological and physical processes, upstream, in close proximity, and downstream to islands and reefs (Hamner and Hauri, 1981). Islands act as oases, increasing long-term phytoplankton biomass up to 86% compared to the offshore conditions (Gove et al., 2016).

Increased productivity has been measured near several islands, for example: Madeira Archipelago (Caldeira et al., 2002), Juan Fernández Archipelago (Andrade et al., 2014b), and St. Croix (Virgin Islands) (Chérubin and Garavelli, 2016). In the Indian ocean it has been reported at Aldabra and Cosmoledo atolls (Heywood et al., 1990), Kerguelen Islands (Bucciarelli et al., 2001) as well as the Maldives (de Vos et al., 2014, Radice et al., 2019, Sasamal, 2006).

However, a systematic and worldwide survey is still lacking, with most studies carried on in a small number of geographically confined locations. Gove et al. (2016) proved that is a near-ubiquitous feature among 91% of the coral reefs they studied across the tropical Pacific, providing an important

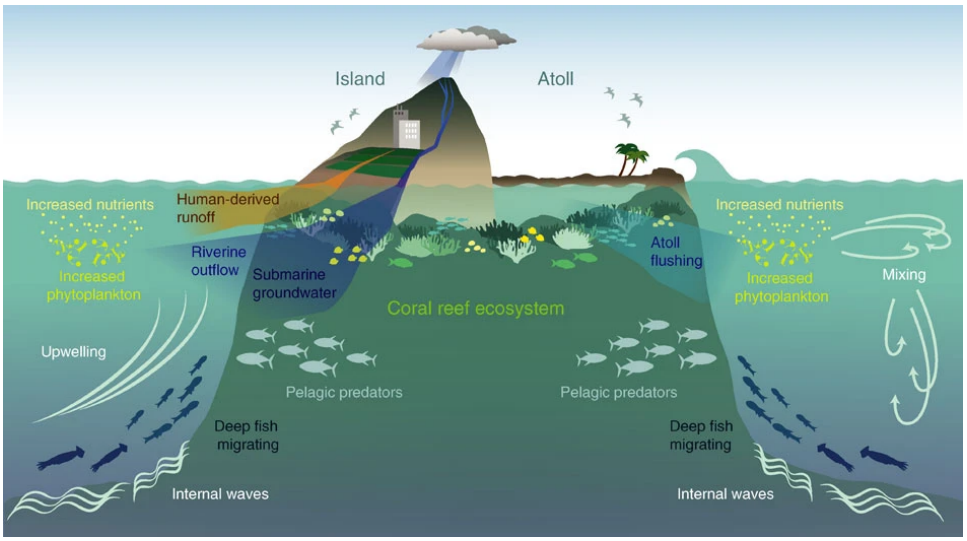

Figure 4.1: Sketch of the Island Mass Effect increased phytoplankton production, and physical and geological processes involved from Gove et al. (2016)

hint that it is a widespread phenomenon.

Plumes of high concentration of chlorophyll-a have been detected propagating downstream of several islands (Andrade et al., 2014b, Coutis and Middleton, 2002, Dong et al., 2007, Sasamal, 2006, Zeiden et al., 2019). Phytoplankton production has also been observed to be enhanced upstream of islands (Gove et al., 2006, Hamner and Hauri, 1981, Liu et al., 2014b).

The mechanisms at the origin of this phenomenon can be several. They all relate to an enhanced input of nutrients in the euphotic layer, which favors biological productivity. Upwelled water is colder, saltier and enriched in nutrients. Several mechanisms have been shown to lead to local upwelling

around islands and atolls, such as cyclonic eddy production, inertial instabilities (Dong et al., 2007, Teinturier et al., 2010), and lee related divergence (Chang et al., 2013, Hasegawa et al., 2004). Upstream of an island, currents impinging on the bathymetry can uplift the isotherms and lead to vertical transport (Gove et al., 2006, Hamner and Hauri, 1981, Liu et al., 2014b). Increased vertical shear, due to the interaction between strong incoming flow and bottom friction, can enhance vertical mixing and intrude water from the thermocline in the mixed layer (De Falco et al., 2020). Tidal waves interacting with the sea floor generate internal waves that are able to deliver cold and nutrient-rich waters to the surface (Storlazzi et al., 2020, Wyatt et al., 2020).

Several land-born factors can also substantially contribute to the IME, such as: nutrient intake from island runoff (Bell, 1992), groundwater discharge (Hwang et al., 2005, Street et al., 2008) and human activities that can increase nearshore nutrient concentrations above natural levels (Gove et al., 2016, Vitousek et al., 1997).

I have checked the SST variations and net primary productivity next to several small islands and archipelagos in order to verify if a similar effect can be seen in the temperature as well. Two different kinds of patterns emerge depending on the size and altitude of the island. The first pattern is characterized by warm/cold anomalies at the two opposite sides of the island and the second by a local, sometimes almost symmetric, cooling. In the following, those patterns are described and the possible mechanisms generating them are discussed. The specific case of the Maldives Archipelago is then studied in detail.

4.1 Data and Methods

The SSTs are from GHRSST dataset at 5km, described in Chapters 2 and 3. Winds at 10 m above the surface are from ERA5 and the surface currents at 0.25° from SODA3.

The Net Primary Productivity (NPP) was obtained from `http://sites.science.oregonstate.edu/ocean.productivity` and estimated according to the Vertically Generalized Production Model (VGPM) algorithm from (Behrenfeld and Falkowski, 1997). The VGPM is a "chlorophyll-based" model that estimates net primary production from chlorophyll using a temperature-dependent description of chlorophyll-specific photosynthetic efficiency. For the VGPM, net primary production is a function of chlorophyll, available light, and photosynthetic efficiency. The product is based on MODIS (NASA Goddard Space Flight Center, Ocean Ecology Laboratory, Ocean Biology Processing Group, 2014) chlorophyll and temperature data. The available light is represented by the depth of the euphotic zone, which is estimated from a model developed by Morel and Berthon (1989) and based on chlorophyll concentration.

For the baroclinic Rossby radius I used the dataset of Chelton et al. (1998) of climatological values with 1° resolution. The first baroclinic Rossby radius of deformation is of fundamental importance in atmosphere–ocean dynamics. It is the horizontal scale at which rotation effects become as important as buoyancy (Nurser and Bacon, 2014). A simple formula to

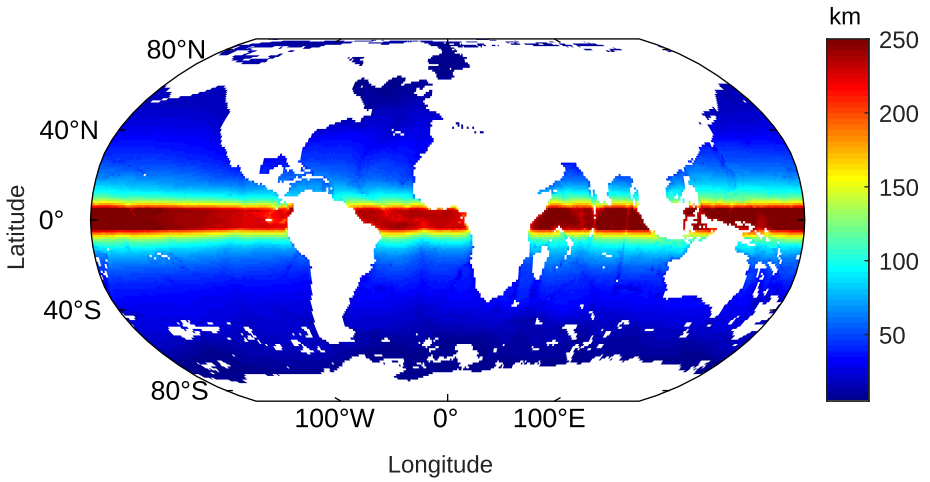

Figure 4.2: Climatology of the baroclinic Rossby deformation radius from Chelton et al. (1998)

calculate it is (Vallis, 2017):

$$Rd = NH/f \tag{3.1}$$

where N is the Brunt-Väisälä frequency, a measure of the buoyancy, H is the vertical scale, and f is the Coriolis parameter: $f = 2\Omega sin(\theta)$ (Ω is the rotation rate of the Earth and θ is the latitude). Chelton et al. (1998)

derived it from the first baroclinic gravity-wave phase speed (c) as:

$$\begin{cases} Rd = \frac{c}{f} & \theta > 5^\circ \\ Rd = \sqrt{\frac{c}{2\beta}} & \theta \leq 5^\circ \end{cases} \tag{3.2}$$

θ is again the latitude and $\beta = 2\Omega cos(\theta)/R_E$, with R_E is the radius of the Earth.

The geographical variability is dominated by the latitudinal dependence of the extra-tropical solution on the Coriolis parameter f. Rd decreases from about 240 km in the near-equatorial band to less than 10 km at latitudes higher than about 60°(see Fig. 4.2). The basin-scale longitudinal variations are manifestations of geographical differences of the vertically integrated stratification, which tends to be strongest in the western parts of the basin, where the permanent pycnocline is deeper. Finally major topographic features such as the Mid-Atlantic Ridge, the East Pacific Rise, the Hawaiian Ridge, the complex of ridges in the Indian Ocean, and numerous smaller ridges and seamount chains throughout the world ocean are clearly delineated by the locally reduced values of Rd in shallower water.

To be able to identify local variations in the temperature near islands and archipelagos, I have used the spatial Laplacian of the SST. Even though it does not identify the minimum or maximum of temperature, it allows to locate the areas surrounding local minima (positive Laplacian) and local maxima (negative Laplacian). The advantage of using this metric resides in the fact that it highlights the small-scale patterns, reducing the signature of large-scale variations, as it is shown in Fig. 4.3, where the 2013

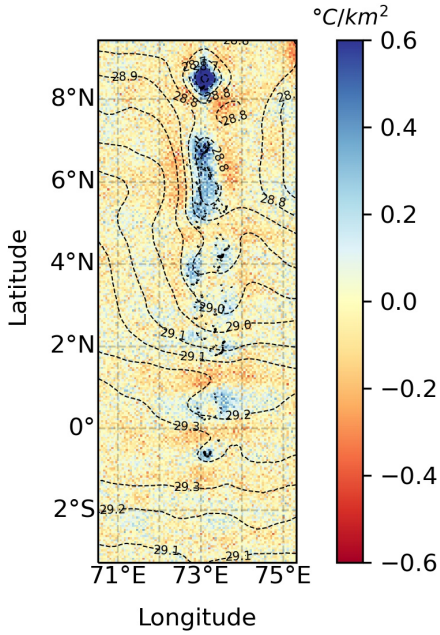

Figure 4.3: Comparison between the 2013 annual SST laplacian (shaded) and the annual SST (isolines) for the Maldives.

annual SST and laplacian around the Maldives are compared. SSTs are influenced by several processes with a wide range of spatial and temporal scales. The SST laplacian is a useful tool that can help identify local temperature variations, albeit not providing any information about the physical mechanisms generating them nor about the actual magnitude of the signal. A comparison with the NPP patterns can, although, provide important information about localized area of enhanced vertical mixing or upwelling. Regions of both increased productivity and colder temperatures can be linked - with reasonable certainty - to an intensified input of nutrient rich waters from below the mixed layer. Furthermore, it is always important to consider the complexity of the systems studied and the huge amount of physical and biological processes involved, being the SST influenced only by the firsts, it can also help disentangle the different effects. The educated hypothesis that is possible to make by interpreting the data need to be verified through modeling and in-situ measurements.

The R1.6v1 simulation for 2013, with a temporal resolution of 1 hour was used coupled with the particle tracking model Ariane, to resolve the three-dimensional trajectories that can help identifying the processes that affect vertical transport in the upper ocean. Particles were deployed every 12 hours 5 meters above and below the local mixed layer depth, at about 5 km from the coastline, in the northern central part of the Archipelago (from 2.1° to 7.1°N). The boxes containing the particles were set both at the east and west sides of the Archipelago (see Fig. 4.4). The trajectory of each particle was then tracked.

The simulation lasts for the first 15 days of three selected months, representative of different dynamical settings. February and June represent

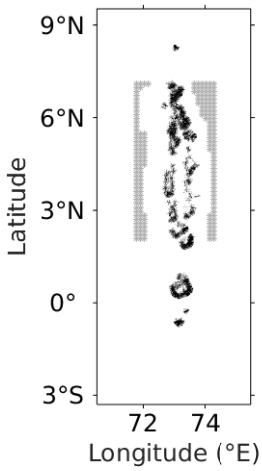

Figure 4.4: Initial particles position at west and east sides of the Archipelago

the NE and SW monsoon circulation, respectively, and April was considered as a transition month.

4.1.1 SST signature around small islands and archipelagos

The classical problem of an obstacle in a horizontal flow, for a fluid with uniform density and in a non-rotating reference frame has been widely studied (Batchelor, 2000, Cushman-Roisin and Beckers, 2011), showing that the flow is well characterized by the Reynolds number. However, in the ocean, the presence of stratification and rotation further complicates the problem. The resulting flow strongly varies depending on whether both stratification and rotation are equally important or if one is predominant (Dong et al., 2007).

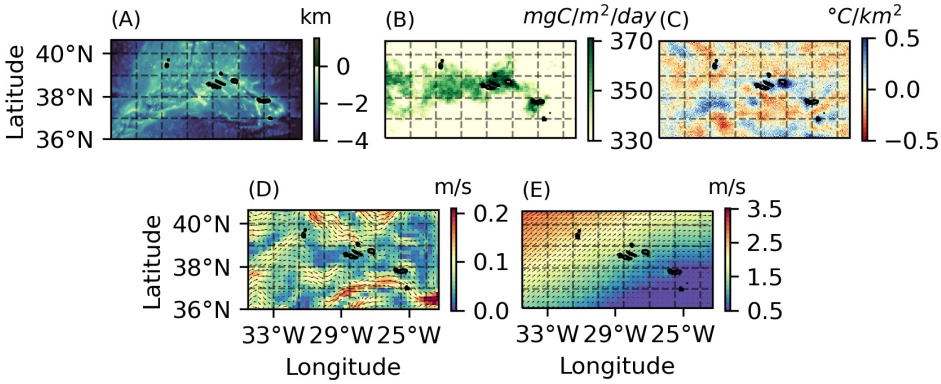

Figure 4.5: Azores (A) Bathymetry and Annual (B) NPP, (C) SST Laplacian, (D) Currents, and (E) Wind Speed of the 2013. Black dashed line 100 m depth isoline..

4.1.2 Wind forced dynamics

The circulation resulting from the interaction of a surface Ekman layer with a circular island in a stratified flat bottom ocean, is explained thoroughly by Spall and Pedlosky (2013). When a uniform and steady wind stress is applied on an island, the resulting Ekman current velocity is directed 90° to the right of the wind stress. The basic response is similar to the development of boundary currents, with upwelling/downwelling in narrow layers next to the coastline. The flow on the downstream side of the island produces upwelling, while the upstream side of the island experiences downwelling. However, this kind of circulation is subordinated to the developement of baroclinic boundary currents of the scale of the Rossby radius to fulfill the mass balance. The horizontal scale (L) of the islands considered in this

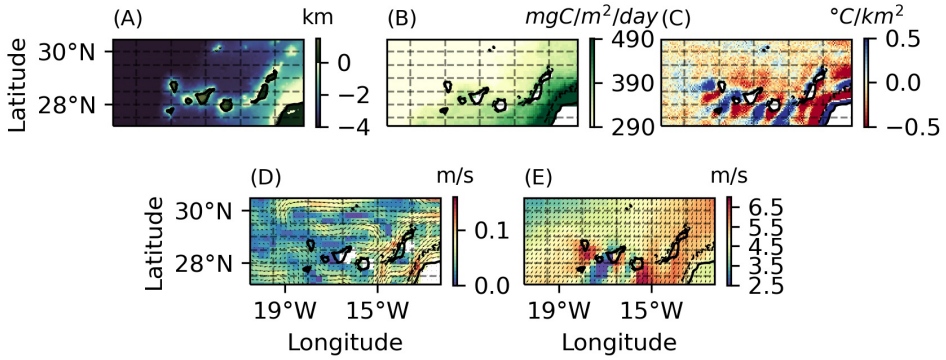

Figure 4.6: Canary Islands (A) Bathymetry and Annual (B) NPP, (C) SST Laplacian, (D) Currents, and (E) Wind Speed of the 2013. Black dashed line 100 m depth isoline..

thesis is not enough to sustain the formation of this kind of circulation, where $L >> Rd$ is necessary (see Table 4.1).

Not only the wind stress forcing should be considered but also the wind stress curl that can provide another source of vorticity around an island. In this second case, the height of the island plays an important role.

When winds pass an island, the intensity of the wind behind the island could decrease dramatically because of the increase in land surface roughness and blocking by high mountains. This can lead to positive and negative wind curls on the right and left sides (when one faces downstream), respectively. Ekman pumping then forces local upwelling or downwelling (Basterretxea et al., 2002). In the case of the Hawaiian Islands, the combination of wind stress generated by the island mountains and the flow of geostrophic currents results in an ocean wind wake that can extend thousands of kilometers (Xie

et al., 2001).

Cold/warm anomalies can be seen around the Canaries, Cape Verde, the Hawaii, Vanuatu, Reunion, and Mauritius main island (see Fig. 4.6A, 4.8A, 4.9A, 4.10A and 4.11A). A pattern that closely resembles the SST variations is also present in the NPP (Figs. 4.6B, 4.8B, 4.9B, 4.10B and 4.11B). These are volcanic islands, with an elevation over the sea level large enough to interact with the winds. Furthermore, they are located in the Easterlies band and subjected to a relatively stable wind regime along the year.

The effect of the wind wake on the sea surface temperature has also been reported for the Canary Islands (Basterretxea et al., 2002, Zimmerman, 1969), and Cape Verde (Chavanne et al., 2002). However, in several cases, the surface cooling is located windward (Figs. 4.6, 4.8, 4.9, 4.10, 4.11) and cannot be explained by the wind curl variations that happen mainly leeward. A preliminary analysis of ERA5 winds, at a resolution of 25 km, shows no match between the temperature and wind stress curl pattern (not shown). Wind stress datasets from satellites' scatterometers (Korsbakken and Furevik, 1998) have the same resolution which, unfortunately, is not enough to perform a detailed analysis of the surface wind patterns with a high level of reliability. Winds with a 1 km resolution, measured with a synthetic aperture radar (SAR), are now available from Sentinel1 (Gao et al., 2019) but only over limited areas.

Downstream of mountainous islands, like Canary and Hawaii, strong trade winds crossing them are separated from much calmer areas in the lee of the wake and generate areas of strong horizontal wind shear. Locally, the depth of the surface mixed layer depends on wind speed. In the lee of the

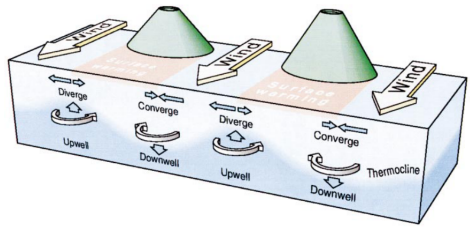

Figure 4.7: Schematic of the Hawaii depicting the eddy generation mechanism due to the wind shear. Ekamn transport taking places in areas of divergence/convergence lead to depression or elevation of the pycnocline, which, in turn, generates cyclonic and anticyclonic eddies, respectively. From Barton (2001).

islands, the winds are weaker and the ML becomes shallower. During the day the heat fluxes are distributed over a thin surface layer which results in intense surface warming (Barton, 2001) (see Figs 4.6, 4.9).

Furthermore, the strong shear between the winds that accelerate when squeezed in the channels between the islands and the calmer lee generates areas of strong Ekman convergence/divergence. In the Northern/Southern Hemisphere at the western boundary upwelling/downwelling must compensate the divergence/convergence, while at the eastern boundary the opposite happens (see Fig. 4.7). In turn, upwelling and downwelling forces changes in the position of the pycnocline, which generates cyclonic and anticyclonic eddies, respectively (Barton, 2001).

Atmospheric wakes have also been detected in the Azores (Caldeira and Reis, 2017). However, São Miguel (Azores largest island) temperature pattern does not display any clear downwelling signal (Fig. 4.5A), despite the

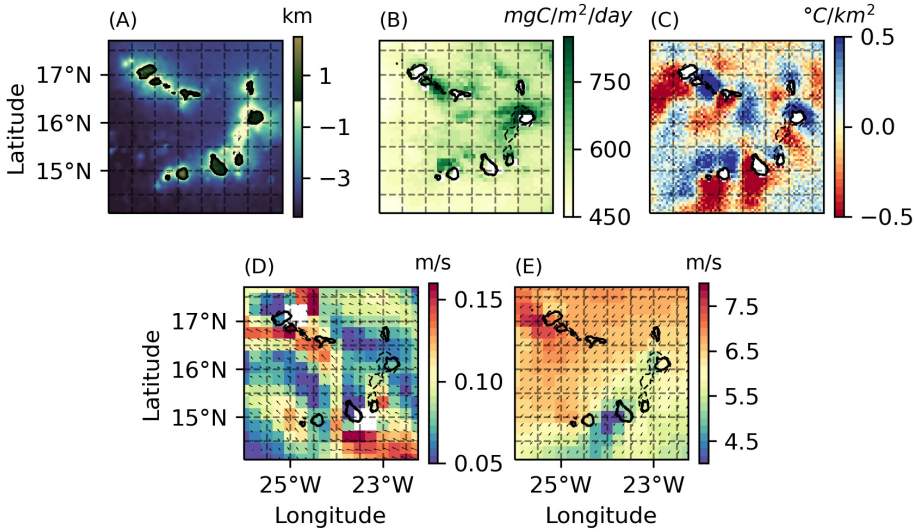

Figure 4.8: Cape Verde (A) Bathymetry and Annual (B) NPP, (C) SST Laplacian, (D) Currents, and (E) Wind Speed of the 2013. Black dashed line 100 m depth isoline..

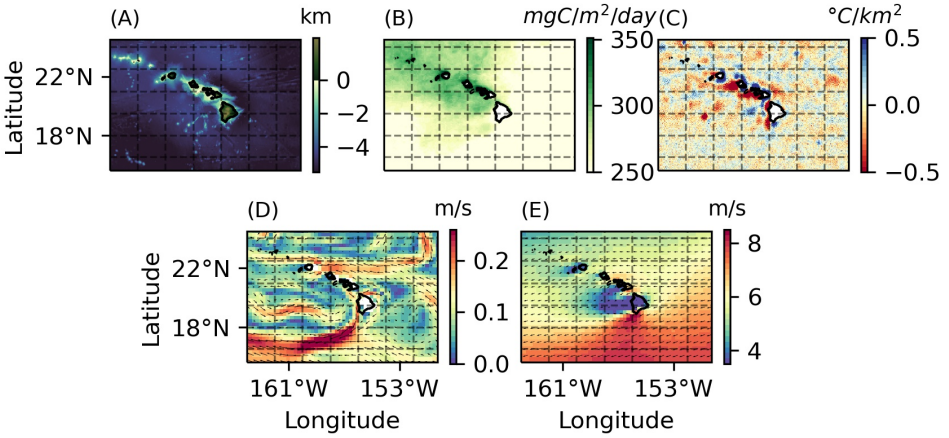

Figure 4.9: Hawaii (A) Bathymetry and Annual (B) NPP, (C) SST Laplacian, (D) Currents, and (E) Wind Speed of the 2013. Black dashed line 100 m depth isoline.

considerable altitude (1000m). On the other hand, the zonal length is much smaller, about 15km. The main island of Okinawa shows a symmetrical cooling pattern (Fig. 4.12), even though it is 135 km long - it is, however, really narrow (15 km wide) - and has a moderate maximum altitude of 500 m. A similar pattern does not appear around Tristan da Cunha (3000m of altitude) (Fig. 4.29) and Saint Helena (800m) (Fig. 4.28). Cold anomalies can be seen around the Comoros (900m), the Seychelles (800m) (see Fig. 4.27) and the Mariana Islands (800m) (see Fig. 4.18) despite their considerable altitude - similar to the one of Reunion and Mauritius main island - but with smaller diameters (table 4.1).

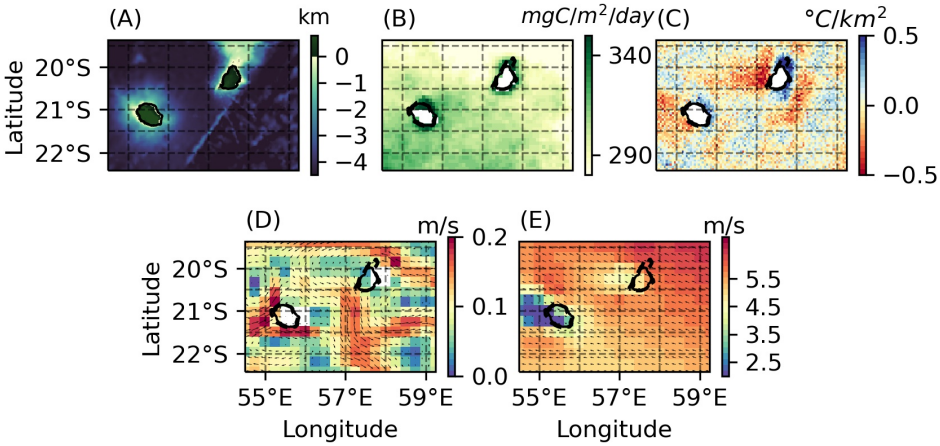

Figure 4.10: Reunion and Mauritius main island (A) Bathymetry and Annual (B) NPP, (C) SST Laplacian, (D) Currents, and (E) Wind Speed of the 2013. Black dashed line 100 m depth isoline.

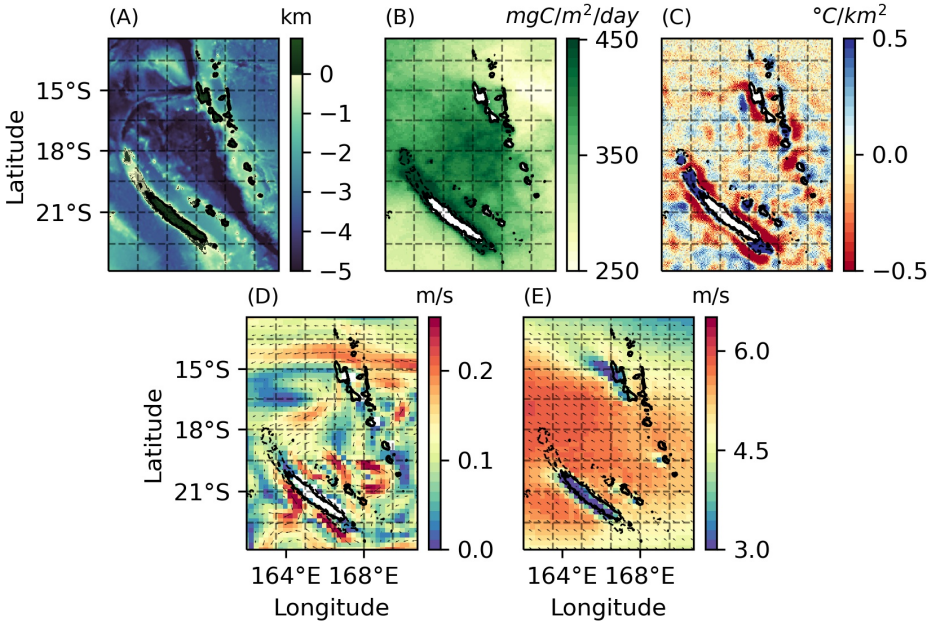

Figure 4.11: New Caledonia and Vanuatu (A) Bathymetry and Annual (B) NPP, (C) SST Laplacian, (D) Currents, and (E) Wind Speed of the 2013. Black dashed line 100 m depth isoline.

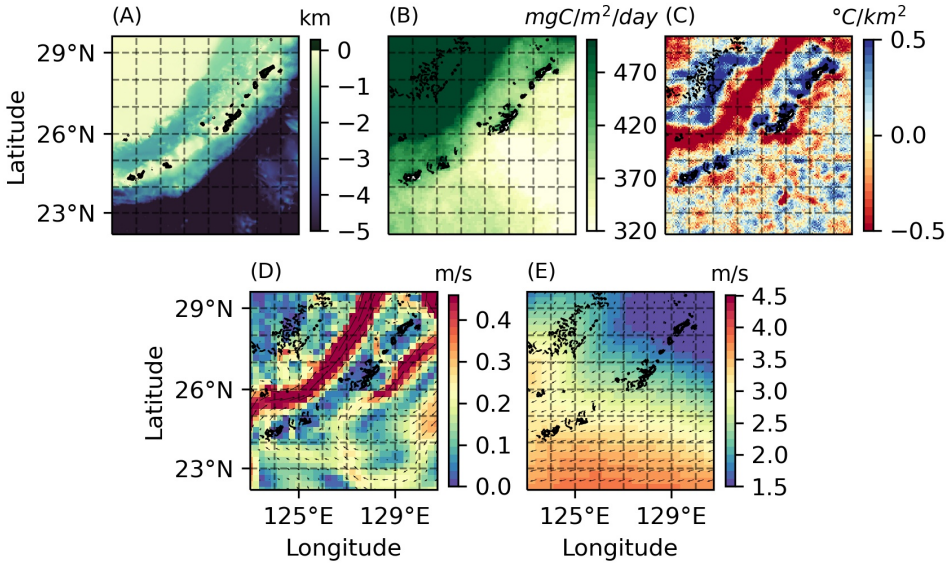

Figure 4.12: Okinawa (A) Bathymetry and Annual (B) NPP, (C) SST Laplacian, (D) Currents, and (E) Wind Speed of the 2013. Black dashed line 100 m depth isoline.

4.1.3 Island Wakes

If the island is small enough, the flow behaviour is similar to the one in a non-rotating and with uniform density incoming stream: the turbulence is characterized by the current speed (U), the island diameter (D), and the horizontal eddy viscosity (ν). For low Reynolds number ($Re = UD/\nu$), the laminar flow is attached to the cylinder with no eddy or wake effects. As Re increases, eddies - alternating in sign - form in the wake. Further increase in Re changes the von Kármán's vortex street to turbulence.

In the case of islands with a greater diameter and big enough depth, the planetary vorticity (f) and the vertical stratification (characterized by N and Rd) become more important. Three more dimensionless parameters become predominant in determining the wake pattern: the Rossby number ($Ro = U/fD$), the Ekman number ($Ek = \nu/fD^2$), and the Burger number ($Bu = Rd^2/D^2$) (Chang et al., 2013).

The predominance of anticyclonic or cyclonic eddies depends on the ratio between Ro and Bu. The onset of the asymmetry begins when Ro/Bu exceeds about 0.2, above which small and large Re leads to the predominance of anticyclonic and cyclonic eddies, respectively (Dong et al., 2007). High Reynolds number regimes can favor local cooling. Cyclonic eddies pump deeper water to the surface, moreover, when they are prevailing, anticyclonic eddies tend to be distorted and disintegrate due to inertial instabilities (Dong et al., 2007) that, in turn, enhance the vertical mixing (Teinturier et al., 2010). Anticyclonic eddies have been shown to favor deeper mixed layers in winter, by weakening the summer-induced stratification (Dufois et al., 2016). As a result, they have colder cores with a higher concentration of

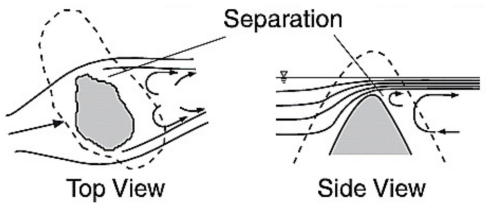

Figure 4.13: Schematic illustrations of deep wake circulation around an island. Solid lines are streamlines. The gray areas are the island (left panel) and the bottom (right panel). Re-adapted from Hasegawa et al. (2004)

nutrients.

Another mechanism that could be responsible for local upwelling is the increase of friction in the wake of an island. Shallow and deep water wakes differ in the mechanism generating the enhancement. In shallow waters, bottom friction generates a secondary circulation in the eddies produced by the land-current interaction, with the sea surface height sloping upward from the centre. At the base of the eddy the centrifugal acceleration is weakened by friction. The pressure gradient persists and pushes water towards the middle and drives the upwelling. (Wolanki and Hamner, 1988).

In the second case, the bottom drag becomes unimportant and the upwelling is controlled from the top, the difference in speed between the currents that accelerate around the flanks of the island and the lee, where the velocity is substantially smaller. The pair of horizontal surface jets behind the island, entrains water from the lee side of the island and cause surface divergence in the wake (Hasegawa et al., 2004) that is fed by a deeper returning current in the lee (see Fig. 4.13). In addition to the horizontal divergence, the vertical separation of the jets downstream of the shoals

	Latitude	Longitude	Max Altitude	Max Dimension		Mean Rd
Andaman and Nicobar	6 to 15 °N	90 to 96 °E	700 m	18 km		101 km
Azores	36 to 40 °N	23 to 34 °W	2300 m	65 km		23 km
Bermuda	31 to 33 °N	67 to 64 °W	76 m	19 km		38 km
Canary islands	13 to 11 °S	36 to 38 °W	2000 m	50 km		32 km
Cape Verde	26 to 22 °S	14 to 18 °E	2800 m	55 km		56 km
Chagos	4 to 9 °S	69.5 to 74.5 °E	3 m	40 km	2 km	161 km
Comoros	14 to 10 °S	42 to 42 °E	900 m	70 km		140 km
Hawaii	15 to 24 °N	164 to 150 °W	4200 m	148 km		62 km
Keeling Islands	12 to 11 °S	96 to 97 °E	9 m	18 km	1km	100 km
Maldives	1 °S to 9 °N	71 to 74 °E	5 m	80 km	1 km	198 km
Mariana Islands	12 to 20 °N	143 to 147 °E	820 m	48 km		78 km
Marshalls	3 to 12 °N	160 to 172 °W	5m	30 km	1 km	163 km
Mauritius (main island)	20 to 19 °S	57 to 58 °E	800 m	65 km		57 km
Mauritius (Rodrigues)	20.5 to 19 °S	63 to 64 °E	62 m	20 km		58 km
Mauritius (St. Brandon)	16 to 15 °S	58.5 to 60.5 °E	5 m	50 km	5 km	68 km
Mauritius (Tromelin)	16 to 15 °S	53.5 to 57 °E	7 m	1.5 km		76 km
Micronesia (Kosrae)	4.5 to 5.8 °N	162 to 163.5 °E	600 m	16 km		231km
Micronesia (Pohnpei)	5.5 to 8.5 °N	155 to 159 °E	780 m	31km		165 km
Micronesia (Tol Weno)	4 to 9.5 °N	148 to 154.5 °E	400 m	11 km		170 km
Nauru	1°S to 0	166.5 to 167 °E	65 m	6 km		250 km
Okinawa Islands	22 to 30 °N	123 to 130 °E	503 m	106 km		51 km
Reunion	21 to 20 °S	55.5 to 56 °E	3000 m	63 km		57 km
Seichelles	10 to 2 °S	52 to 59 °E	900 m	26 km		143 km
St. Helena	16 to 15 °S	6 to 5 °W	800 m	16 km		60 km
Tristan da Cunha	37 to 36 °S	13 to 11 °W	2800 m	11 km		27 km
Vanuatu	24 to 12 °S	162 to 171 °E	1880 m	135 km		66 km

Table 4.1: List of analysed islands: coordinates, maximum altitude, maximum diameter of the islands (for the atolls, diameter of atolls and islands), and averaged Rossby radius in the area

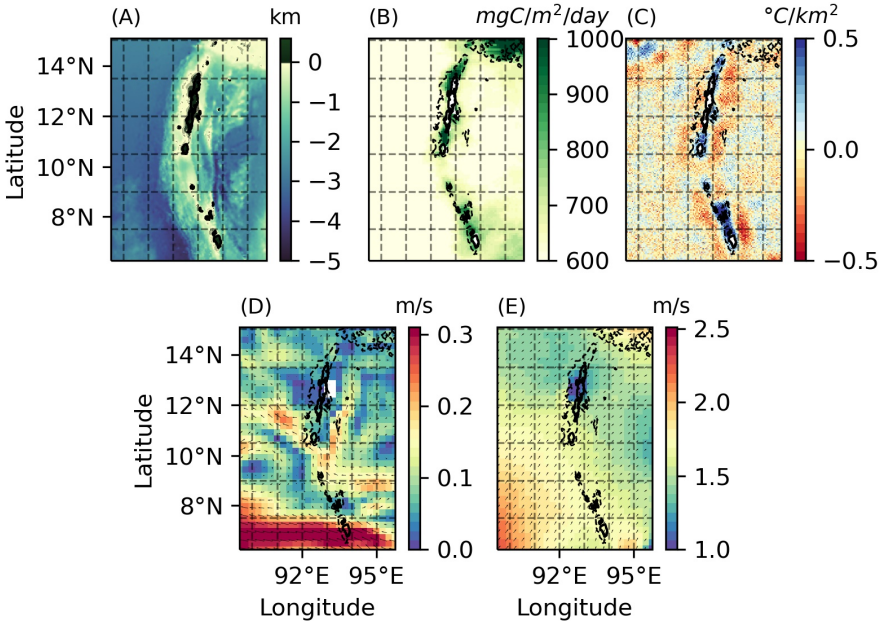

Figure 4.14: Andaman and Nicobar Islands (A) Bathymetry and Annual (B) NPP, (C) SST Laplacian, (D) Currents, and (E) Wind Speed of the 2013. Black dashed line 100 m depth isoline.

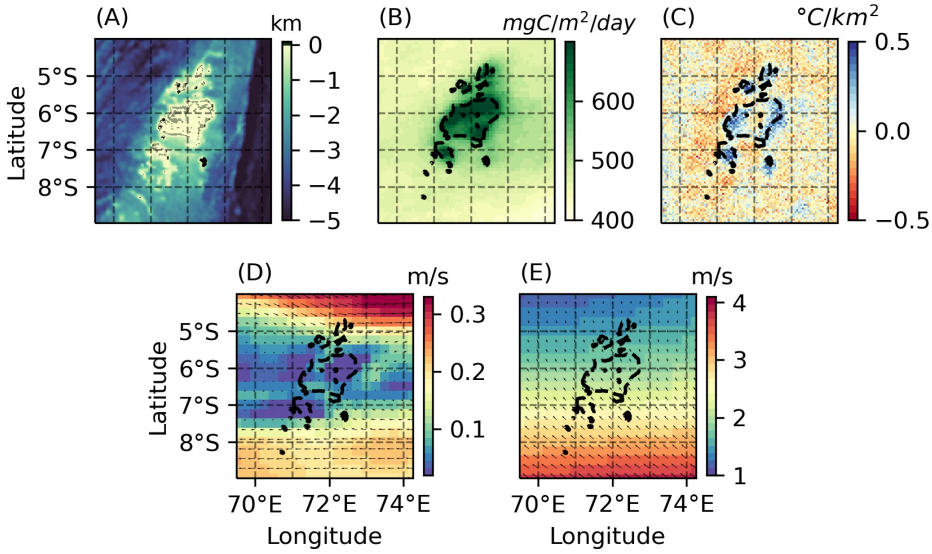

Figure 4.15: Chagos Archipelago (A) Bathymetry and Annual (B) NPP, (C) SST Laplacian, (D) Currents, and (E) Wind Speed of the 2013. Black dashed line 100 m depth isoline.

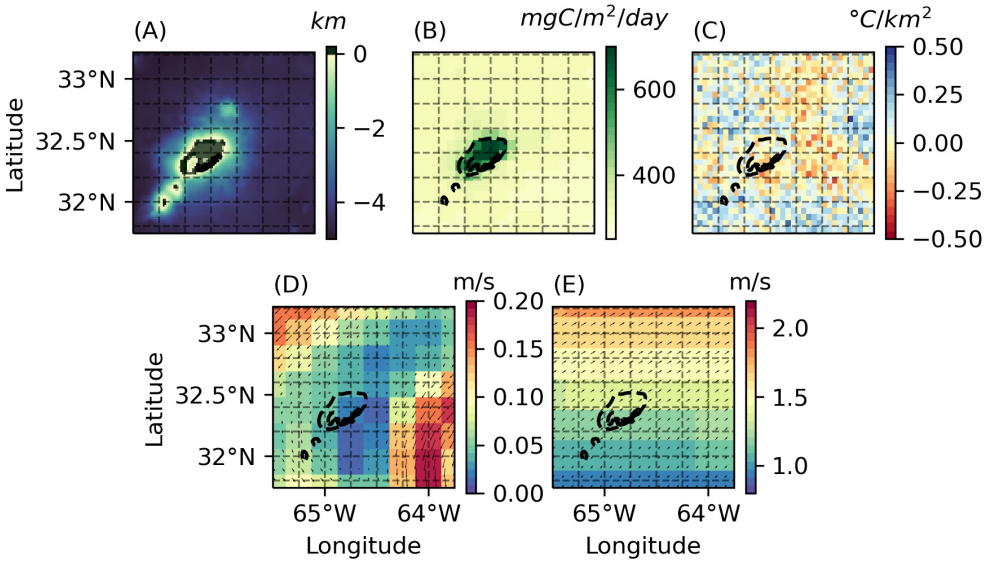

Figure 4.16: Bermudas (A) Bathymetry and Annual (B) NPP, (C) SST Laplacian, (D) Currents, and (E) Wind Speed of the 2013. Black dashed line 100 m depth isoline.

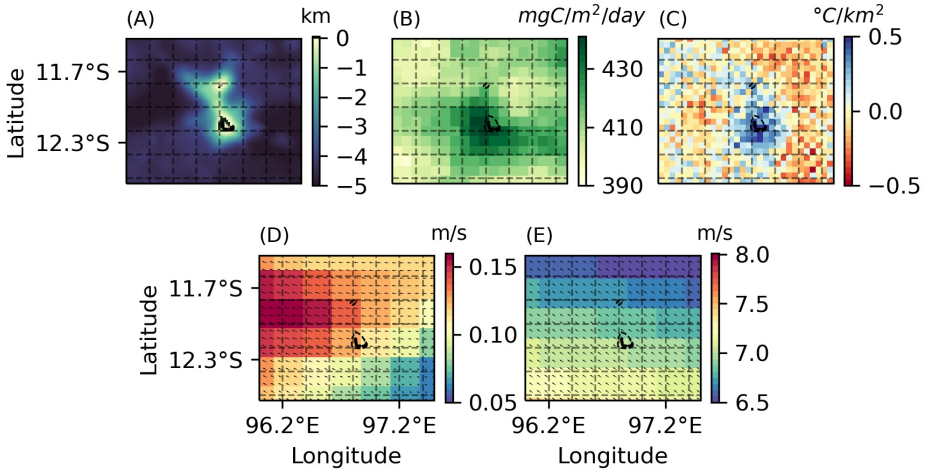

Figure 4.17: Cocos and Keeling Islands (A) Bathymetry and Annual (B) NPP, (C) SST Laplacian, (D) Currents, and (E) Wind Speed of the 2013. Black dashed line 100 m depth isoline.

adjacent to the island also draws fluid up from below (Chang et al., 2013).

Wake-like signals and increased eddy production can be seen propagating downstream of several islands, regardless of the diameter. The effects of island wakes on the ocean circulation have been studied around several islands and atolls using both cruise surveys and model results as well as laboratory experiments (e.g. Alaee et al. (2007), Caldeira and Sangrá Inciarte (2012), Chang et al. (2013), Coutis and Middleton (2002), Dong et al. (2007, 2018), Heywood et al. (1990), Perret et al. (2006), Ronald et al. (1997), Stegner (2014))

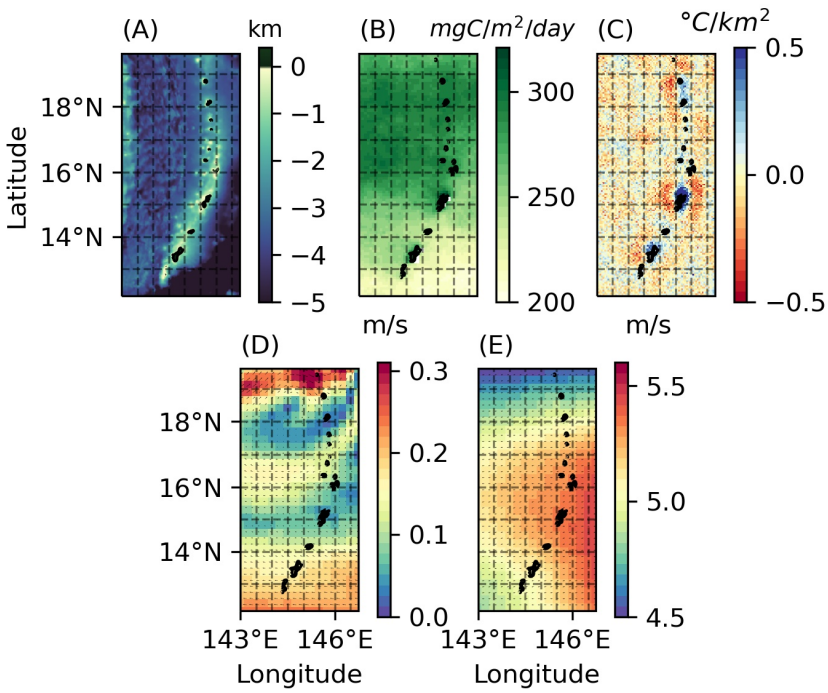

Figure 4.18: Mariana Islands (A) Bathymetry and Annual (B) NPP, (C) SST Laplacian, (D) Currents, and (E) Wind Speed of the 2013. Black dashed line 100 m depth isoline.

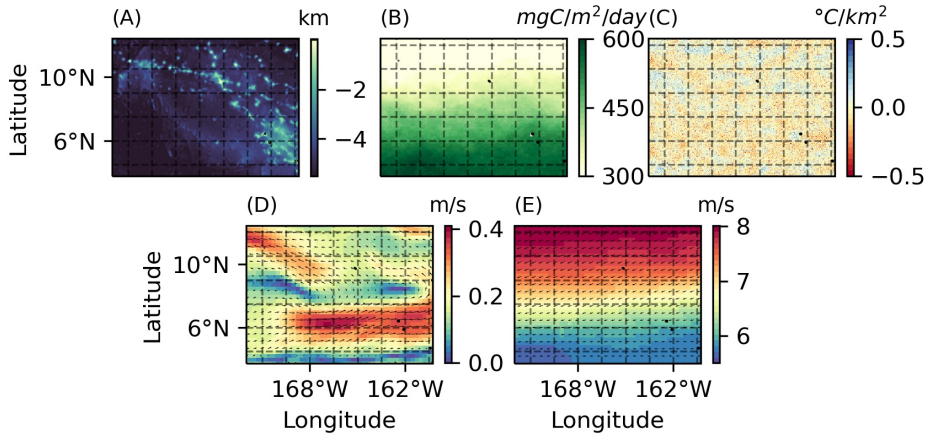

Figure 4.19: Marshall Islands (A) Bathymetry and Annual (B) NPP, (C) SST Laplacian, (D) Currents, and (E) Wind Speed of the 2013. Black dashed line 100 m depth isoline.

4.1.4 Other upwelling and mixing mechanisms

Internal waves have been proven to be of fundamental importance to entrain colder water in the upper ocean and offset bleaching events (Storlazzi et al., 2020, Wyatt et al., 2020). Their ability to propagate shoreward is related to the topographic slope (Merrifield and Holloway, 2002): a gradual slope favors internal wave propagation toward shallower waters, whereas a steeper topography reflects them offshore (Gove et al., 2016).

Furthermore, intense bottom-flow interactions can force the currents to abruptly decrease their speed. The severe shear can lead to unstable Richardson number, overcome the stratification, and enhance vertical mixing, thus entraining deep cold water in the mixed layer (De Falco et al., 2020).

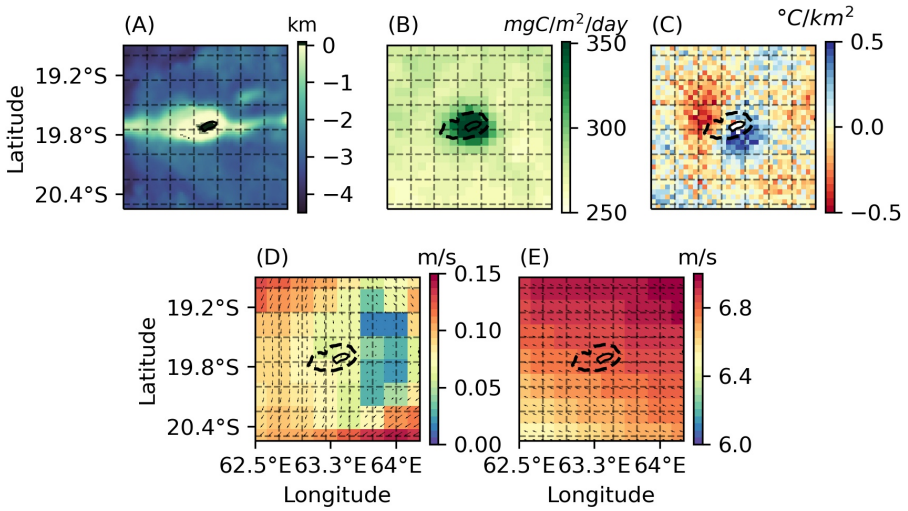

Figure 4.20: Rodrigues Island (Mauritius) (A) Bathymetry and Annual (B) NPP, (C) SST Laplacian, (D) Currents, and (E) Wind Speed of the 2013. Black dashed line 100 m depth isoline.

Finally, a strong zonal current impinging on a slope can be lifted by it, forcing colder and enriched in nutrients water inside the mixed layer, as it happens when the Equatorial Undercurrent hits the Galapagos west coastline (Liu et al., 2014b).

4.1.5 Small Islands

Despite the seasonality of these phenomena, colder anomalies and increased NPP can be seen in their annual averages around several small islands with limited altitude. For example Saint-Brandon Islands and Rodrigues

(Mauritius) (see Fig. 4.20), Chagos Archipelago (Fig. 4.15), the Comores and the Seychelles (see Fig. 4.27), the Andaman and Nicobar Islands (Fig.4.14) in the Indian Ocean; around the Azores (Fig. 4.5) in the Atlantic Ocean; the Mariana Islands (Fig. 4.18), part of Micronesia (Fig. 4.24 and Fig. 4.23) and Okinawa (Fig. 4.12) in the Pacific. Increased NPP and decreased temperature can be seen also over shallow sand banks (e.g. Figs. 4.23 and 4.24).

Plumes of colder and nutrient enriched water, propagating downstream from the islands, are consistent with increased eddy activity and deep water island wakes. Upstream cooling can be explained by current-slope interactions while patterns with higher symmetry by shear instability and internal waves.

Further and more detailed analyses for each case would be necessary in order to identify which one of the processes - or more than one - is responsible for the local cooling.

4.1.6 No surface signature

In some cases, in particular - but not only - in the case of sparse coral islands with a really low altitude, no clear signal can be detected in the SST nor in the productivity.

Few examples are: the Marshall Islands (Fig. 4.19), Tromelin (Mauritius) (Fig. 4.22), and Narau (Fig.4.26). The signal is not present either around Saint Helena (Fig.4.28), in the Pacific Ocean, even despite the considerable altitude.

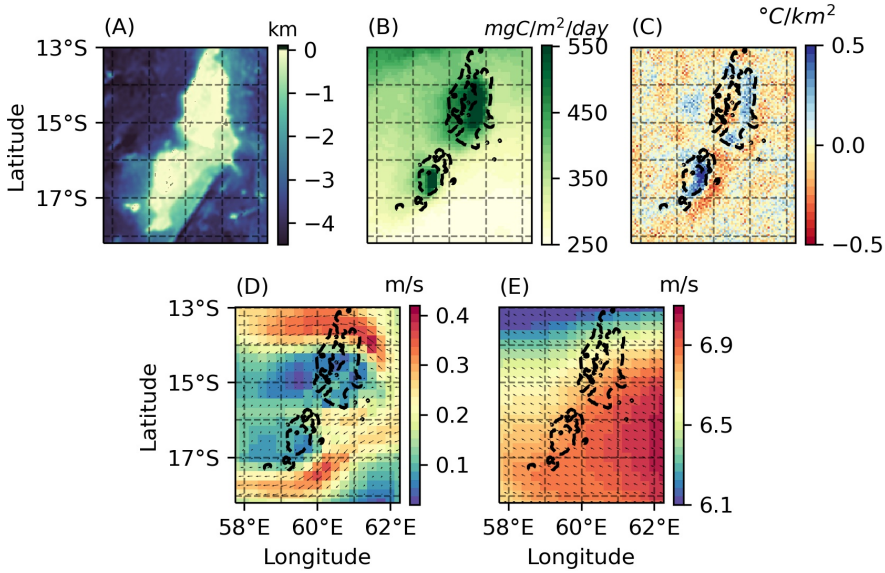

Figure 4.21: Saint Brandon Islands (Mauritius) (A) Bathymetry and Annual (B) NPP, (C) SST Laplacian, (D) Currents, and (E) Wind Speed of the 2013. Black dashed line 100 m depth isoline.

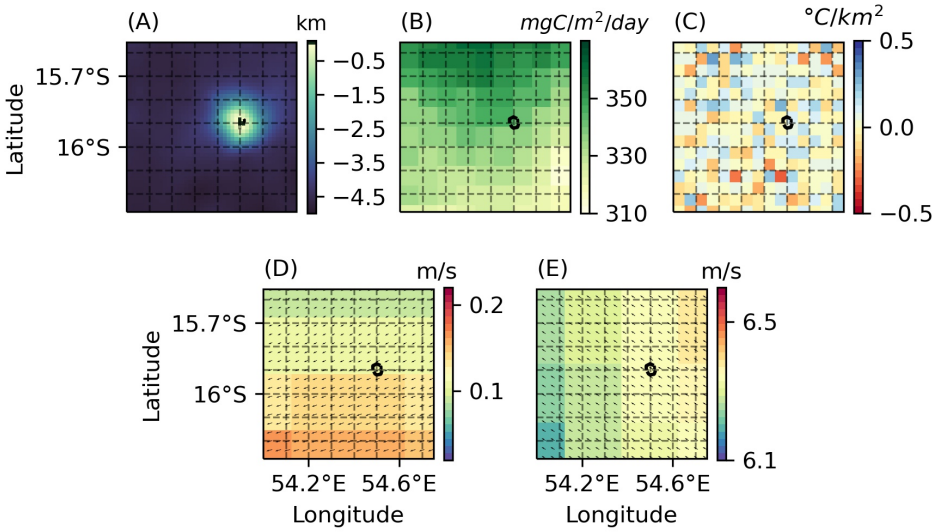

Figure 4.22: Tromelin Island (Mauritius) (A) Bathymetry and Annual (B) NPP, (C) SST Laplacian, (D) Currents, and (E) Wind Speed of the 2013. Black dashed line 100 m depth isoline.

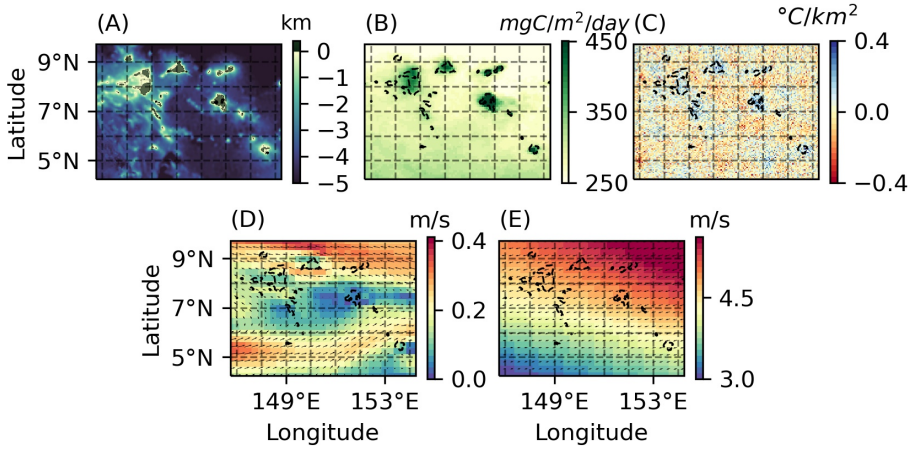

Figure 4.23: Micronesia, Tol sector (A) Bathymetry and Annual (B) NPP, (C) SST Laplacian, (D) Currents, and (E) Wind Speed of the 2013. Black dashed line 100 m depth isoline.

In some cases a surface imprint is visible in only one of the analysed variables, for example, in the NPP for Bermuda (Fig. 4.16) and in the SST for Tristan da Cunha (Fig. 4.29). Around the Comores the signal is not uniform with a weak cooling and weaker NPP around Grande Comore (Fig. 4.27). If the photic zone is deeper than the mixed layer, the nutricline can be deeper than the thermocline: upwelled water would be cold but still nutrient depleted. This could explain the last two cases described. In the case of the Bermuda, a more detailed monthly analysis (not shown) has shown that the signal could be due to enhanced vertical mixing over the shallower area constituted by the caldera of the old volcano. NPP is increased all year-round, if compared to the surrounding waters, while the local temperature is strongly coupled with the heat fluxes seasonal cycle. During summer, the heat fluxes can warm the thinner layer more efficiently, and the temperature increases in the shallower region. In winter, it cools faster, and it give rises to a spatial minimum of the temperature. Averaging the signal over the year, the SST imprint disappears.

The lack of surface signals might be due to the fact that the islands are too small to meaningfully interact with the large-scale ocean dynamics and their wakes are too weak. The other possibility is that the surface variations in temperature and productivity have a magnitude and extension too small that cannot be resolved by satellite data.

The difference between distinct coral reef archipelagos seems to be related to the underlying bathymetry and how the islands are grouped. The presence of a significant and extended topographic feature provides an important barrier to the flow, despite the small dimension of each single island, especially if they are organized in neighboring and almost closed

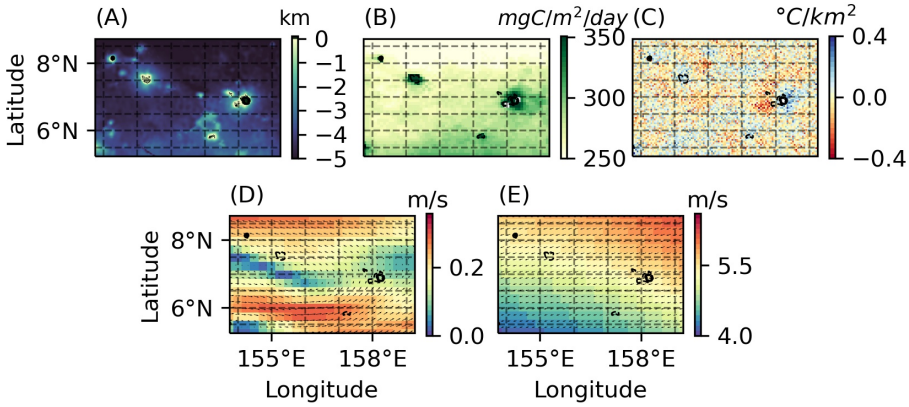

Figure 4.24: Micronesia, Pohnpei sector (A) Bathymetry and Annual (B) NPP, (C) SST Laplacian, (D) Currents, and (E) Wind Speed of the 2013. Black dashed line 100 m depth isoline.

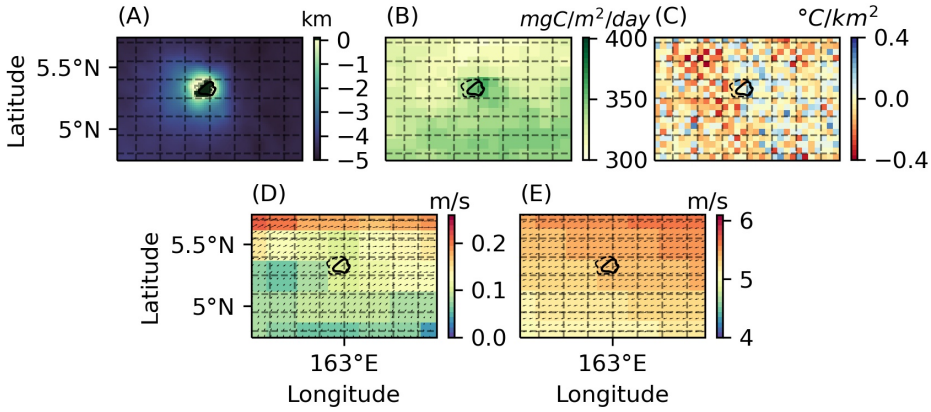

Figure 4.25: Micronesia, Korsea sector (A) Bathymetry and Annual (B) NPP, (C) SST Laplacian, (D) Currents, and (E) Wind Speed of the 2013. Black dashed line 100 m depth isoline.

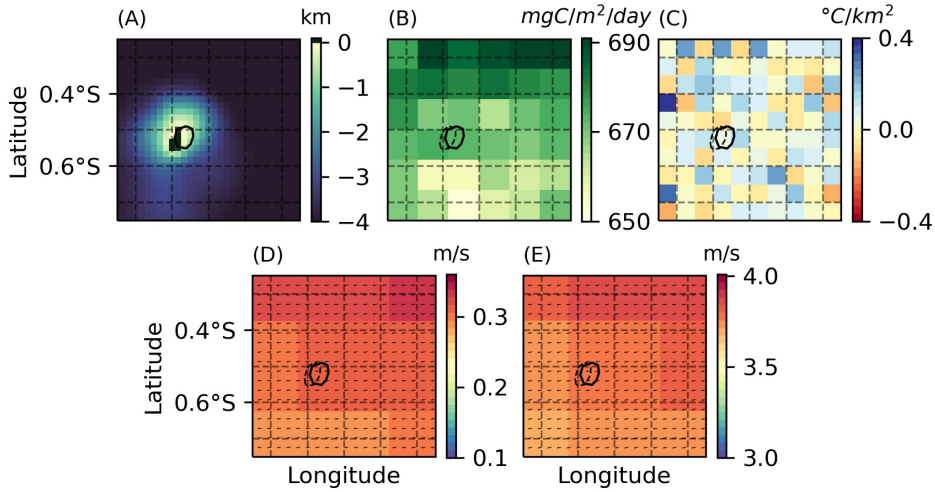

Figure 4.26: Nauru (A) Bathymetry and Annual (B) NPP, (C) SST Laplacian, (D) Currents, and (E) Wind Speed of the 2013. Black dashed line 100 m depth isoline.

atolls as in the case of the Maldives and Chagos Archipelagos. On the other hand, no variations can be seen around the Marshall Islands that are more scattered and with a stepper and less extended underlying bathymetry.

4.2 The Maldives

In the proximity of the Maldivian archipelago, the surface waters are colder and more productive than in the surrounding areas, as shown in fig. 4.30A,B. The SST Laplacian pattern is symmetric and similar to some of the cases discussed in Section 4.2.4, with the absence of a clear downwelling signal,

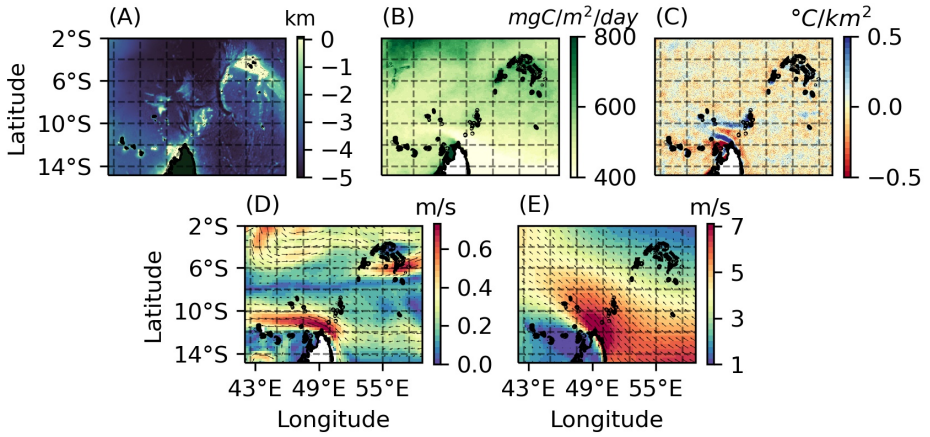

Figure 4.27: Comoros and Seychelles (A) Bathymetry and Annual (B) NPP, (C) SST Laplacian, (D) Currents, and (E) Wind Speed of the 2013. Black dashed line 100 m depth isoline.

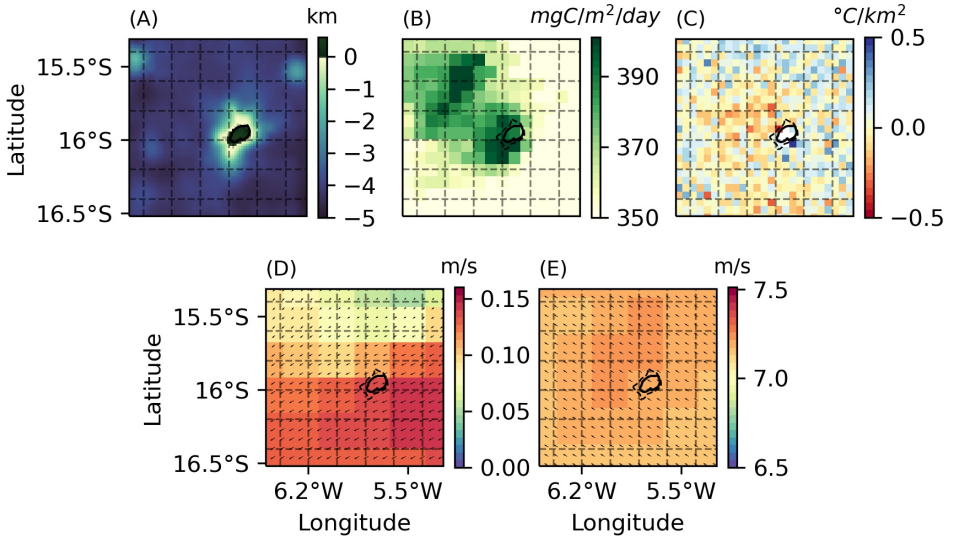

Figure 4.28: Saint Helena (A) Bathymetry and Annual (B) NPP, (C) SST Laplacian, (D) Currents, and (E) Wind Speed of the 2013. Black dashed line 100 m depth isoline.

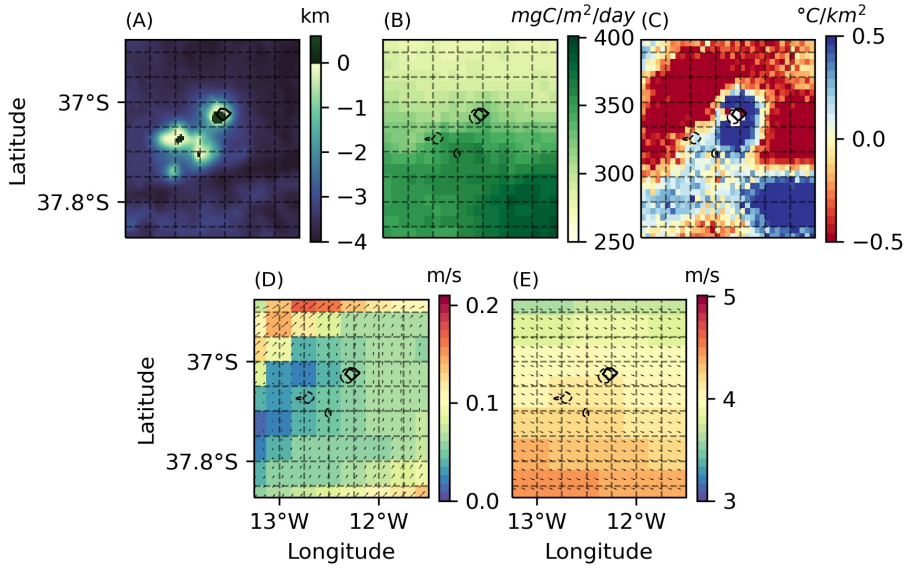

Figure 4.29: Tristan da Cuñha (A) Bathymetry and Annual (B) NPP, (C) SST Laplacian, (D) Currents, and (E) Wind Speed of the 2013. Black dashed line 100 m depth isoline.

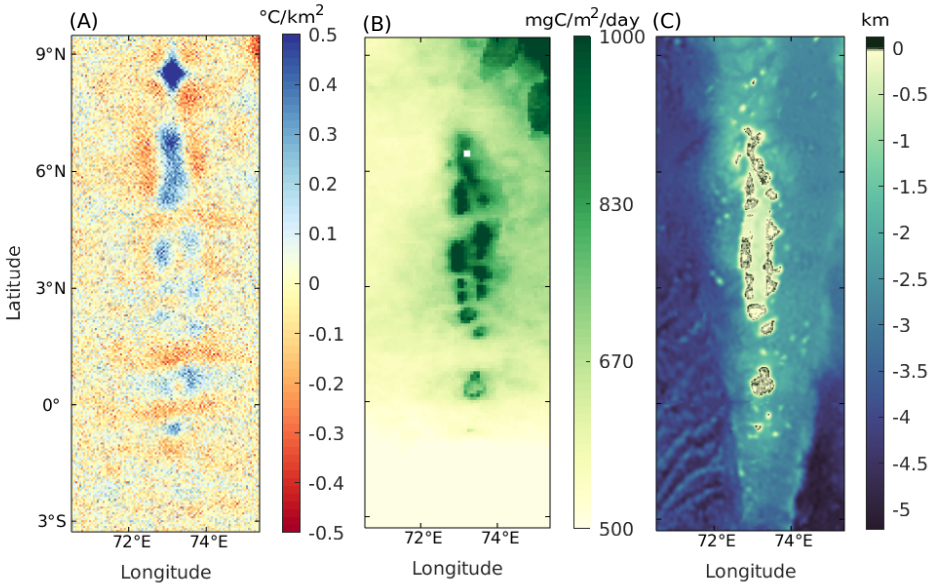

Figure 4.30: SST Laplacian (A), NPP (B) for the 2013 and bathymetry (C) of the Maldives

even though the steep bathymetry stretches for several thousands of km and provides an important topographic barrier to the strong incoming flow. The size of each island is of the order of magnitude of hundreds of meters, but they are organized in almost closed atolls, with bigger diameters and few narrow passages.

As seen in Chapter 3, currents interacting with the underlying topography give rise to shear instabilities. Unfortunately, the low resolution of the R5 simulation is not able to represent properly the complex land distribution at the surface. Wakes increased eddy production and shredding, and topographical upwelling might have been overlooked. A more detailed analysis is then performed using the R1.6v1. The chosen year for the detailed study is 2013, an ENSO neutral year. The seasonality was taken into consideration by analysing the transport across the archipelago in three different months: February and June for the NE and SW monsoons respectively, and April as a transition period.

4.2.1 Upwelling mechanisms

During the monsoons, the circulation is strongly zonal, with intense westward/eastward currents (see Fig 4.31A,C), while in April the currents are generally weaker and their direction is more variable (see Fig 4.31B). The presence of the Maldives significantly alters the circulation. The currents accelerate when passing through the narrow straits between the atolls and are deflected by the topography. The bathymetry increases more abruptly on the west side than on the east side of the Archipelago (Fig. 4.30C), being, therefore, more efficient in diverting the incoming circulation. Currents

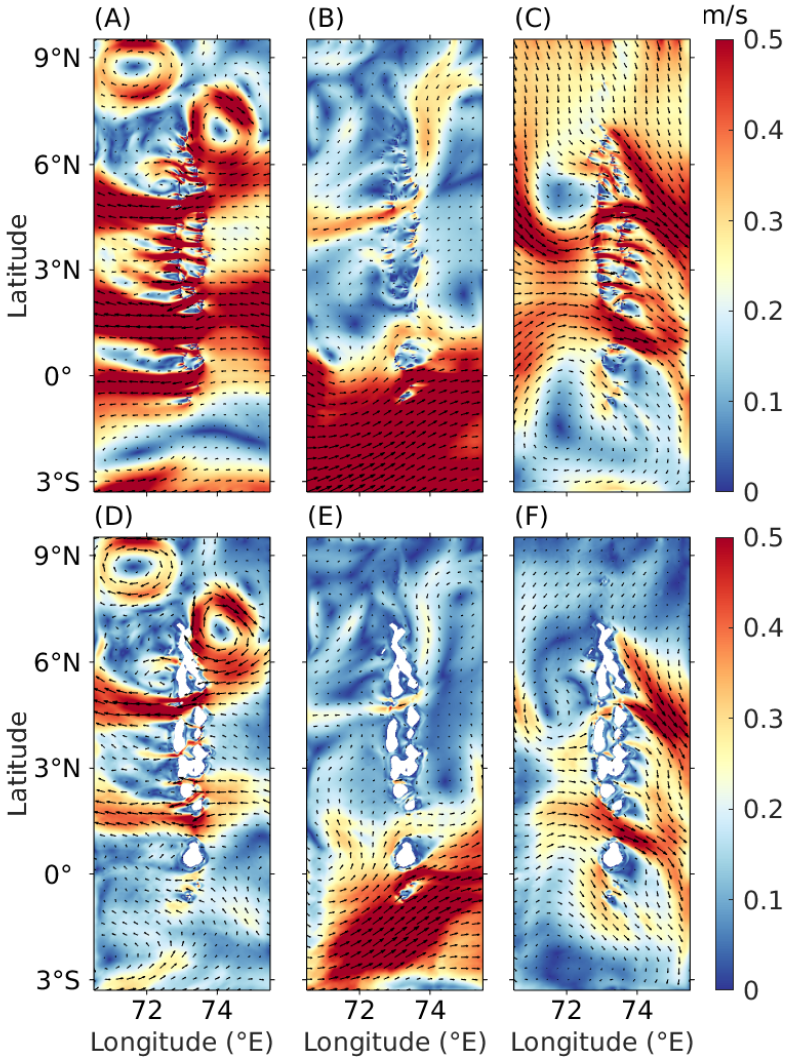

Figure 4.31: Average velocity magnitude (colorscale) and direction (arrows). Surface: panels A,B,C and at 80 m depth: panels D,E,F. From R1.6v1 2013 run. The averages are computed over the first 15 days of (A,D) February, (B,E) April and (C,F) June 2013.

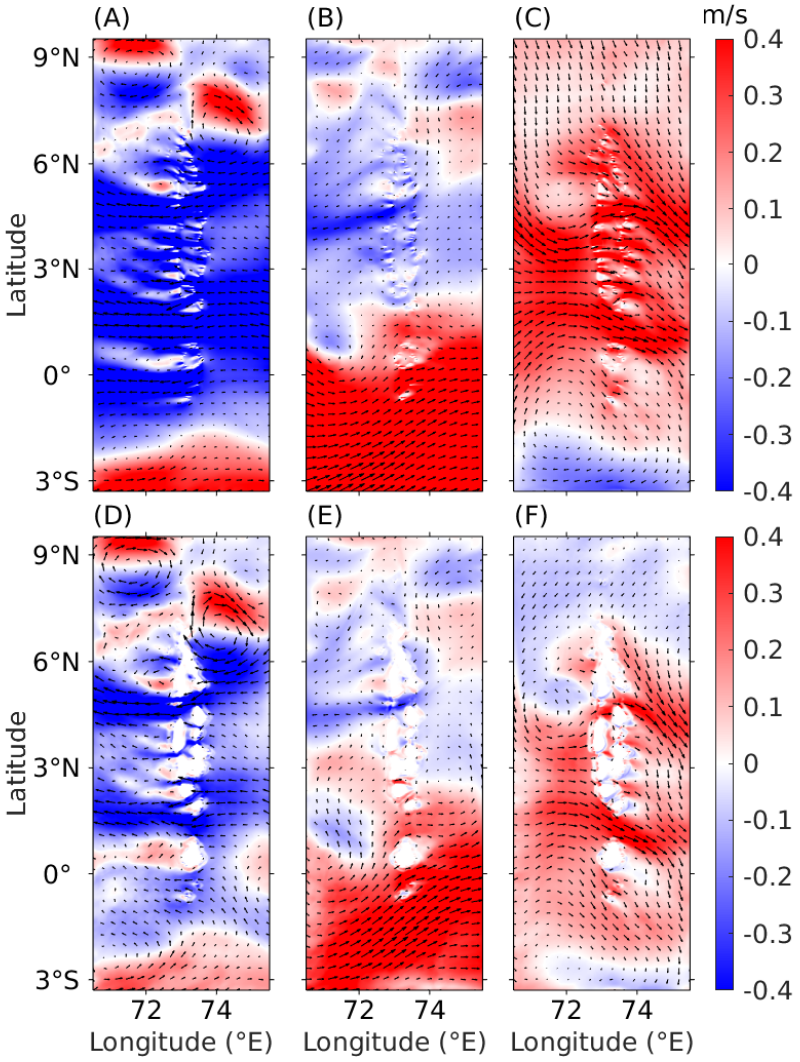

Figure 4.32: Average zonal velocity magnitude (colorscale) and direction (arrows). Surface: panels A,B,C and at 80 m depth: panels D,E,F. From R1.6v1 2013 run. The averages are computed over the first 15 days of (A,D) February, (B,E) April and (C,F) June 2013.

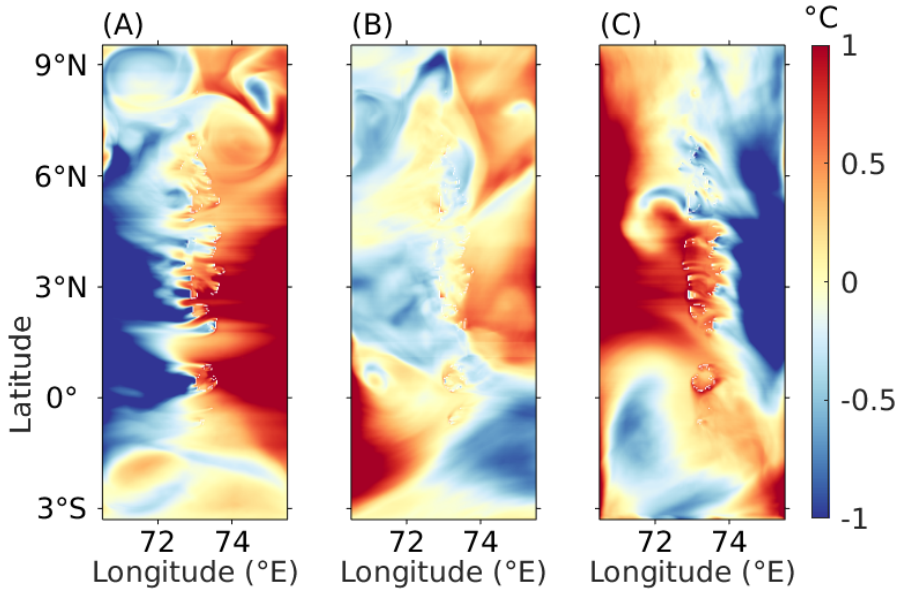

Figure 4.33: Temperature anomalies with respect to the zonal mean over the first 15 days of (A) February, (B) April and (C) June from R1.6v1 2013 run.

display larger variations from the zonal flow on the incoming side in June than in February.

During the monsoons, strong, but localized, upwelling occurs in the lee of deep water wakes. The temperature displays a large latitudinal gradient, with intense cooling taking place on the opposite side of the archipelago than the incoming flow. In Fig. 4.33A,C two successive sets of wakes can be seen, with the second one producing the stronger temperature signal. Already intense currents further accelerate when squeezed in small passages between the atolls and on the flanks of the islands. When they interact with

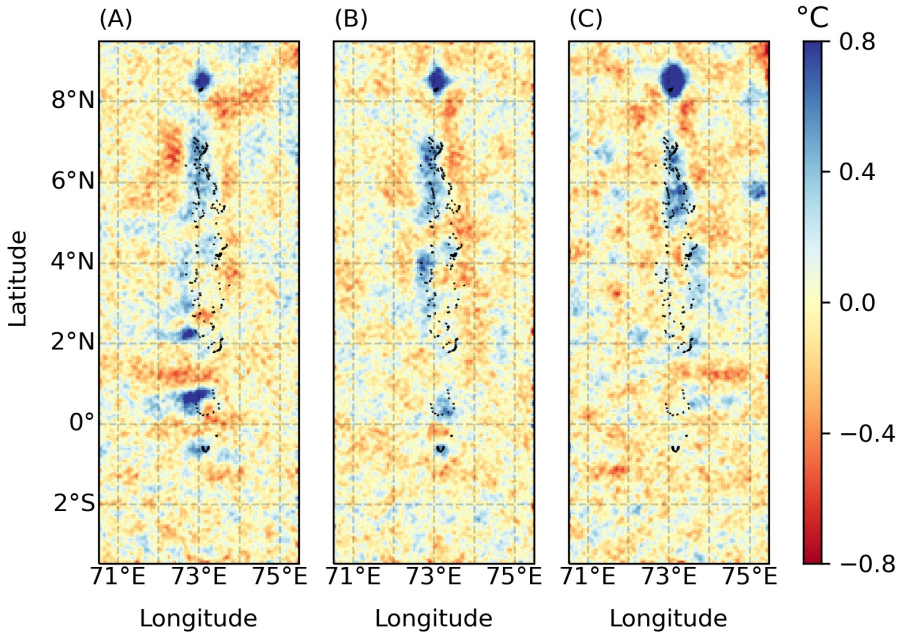

Figure 4.34: SST Laplacian from GHRSST at 5km data of (A) February, (B) April and (C) June 2013. The signal was spatially smoothing using a using a (cubic) smoothing spline of fall-off value $\lambda = 0.2$.

	February		April		June	
	Up-going	Down-going	Up-going	Down-going	Up-going	Down-going
Incoming	89%	30%	88%	85%	91%	34%
Outgoing	90%	8%	83%	75%	87%	8%

Table 4.2: Up-going and down-going particles percentages computed as the amount of particles deployed 5 meter below/above the local MLD that were able to cross 5 m above/below the local MLD. Incoming and outgoing refer to the side of the Archipelago, with respect to the flow, where the particles were deployed: east/west in February and April, and west/east in June (see Fig. 4.4)

the second chain of atolls, the horizontal velocity shear further increases and is able to drive vigorous upwelling. This hypothesis is corroborated by the presence of the deep return flow in the lee, as can be seen in Fig. 4.32,D,F and consistent with de Vos et al. (2014), reporting higher chlorophyll-a concentrations from satellite data on the west side during the NE monsoon and on the east side during the SW one.

The temperature pattern in the presence of upwelling due to a wake is strongly asymmetrical, with significant cooling occurring downstream, and higher temperatures on the incoming flow side. As it can be seen both in the model results (Fig 4.33A,C) and in the satellite data (Fig 4.34A,C).

Shear instabilities are present year-round and independent from the surface islands. The higher resolution of R1.6v1 allows to resolve the surface bathymetry, whereas R5 could not, making impossible for the model to well reproduce the eddy-generating mechanisms of the wake. Furthermore,

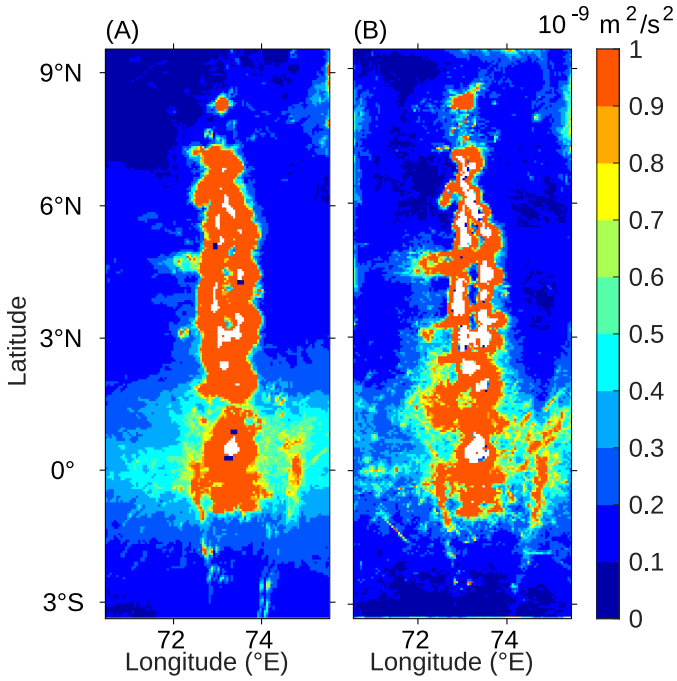

Figure 4.35: Standard deviation of the vertical velocity every 5 days at the base of the mixed layer for the (A) R5, and (B) the R1.6v1 down-scaled to R5 resolution for the period 2010-2016.

when the baroclinic Rossby radius far exceeds the obstacle diameter, the dimension of the produced eddies and the island size are almost equal (Dong et al., 2007). This length, in the case of the Maldives, is about 1km. The annual variance of the vertical velocity at the base of the mixed layer (see Fig.4.35) does not show, however, any significant difference in structure nor magnitude. The few variations seems to be related to the better resolution of the bottom topography than of the surface one.

The particles deployed using Ariane oscillate along the vertical direction in every season. During the monsoons, however, the displacement towards the surface, due to the wake induced upwelling, has a greater magnitude (see Fig. 4.36). During the monsoon periods, the effect of the vertical mixing on the temperature is concealed by the continuous and intense stream of warmer water from the open ocean and the wind-forced deeper mixed layer (ML). When the circulation weakens, the incoming currents slow down, the intensity of the upwelling in the lee fades (Fig. 4.36B) and the impact of the vertical mixing gains importance aided by the shallower ML. The magnitude of the resulting cooling is smaller but spatially more symmetric, influencing both sides of the Maldives (see Fig. 4.33B and 4.34B). The reduced, but more symmetric, imprint of the vertical mixing on the surface also fits the decrease in chlorophyll-a concentration and the absence of plumes during the spring transition months reported by de Vos et al. (2014), in their analysis of productivity variations over the Sri-Lanka/Maldives area.

In the Southern part of the Archipelago, where the currents are always intense, the asymmetry persists also in the transition period (Fig. 4.33B and Fig. 4.34B) and in the annual data (Fig. 4.30A), suggesting that wake-like mechanisms prevail all year. On the other hand, in the northern and central

Maldives, April's SST Laplacian has a structure similar to the annual one. The latter symmetry it is not, therefore, only due to the average of February and June asymmetric but specular signals.

From the trajectories of the particles deployed, I calculated the fraction of up-going and down-going particles (see table 4.2). An equal number of particles were deployed 5 m below and 5 m above the local mixed layer depth every 12 hours. Each particle was counted as up-going or down-going based on whether it crossed the MLD along its trajectory. After the first MLD crossing, the particle was discounted. As expected, the fraction of particles entering the mixed layer from below is larger than the fraction of particles exiting the mixed layer from above both in February and June when the upwelling mechanism is predominant. In April the two values are similar: this is a good indicator of the dominance of vertical mixing during this month.

The cooling signal can propagate inside the atolls thanks to several passages between the islands and it has a significant impact on the SST in shallow lagoons. I ran simulations with slightly different bathymetries, and the small changes produced important surface temperature variations.

This is due to the fact that some of the passages to the lagoons in the R1.6v2 simulations were closed by the use of a topography with slightly bigger islands and less straits. The result was a larger temperature over the atolls. In particular, in the case of weak zonal flow as in April, the temperature over the atolls is significantly higher (see Fig. 4.37,B). A similar mechanism can be noticed by taking into consideration the whole month of June: the currents are fairly less intense (Fig. 4.37F), colder water is mixed in the MLD and it accumulates on the west side of the atolls

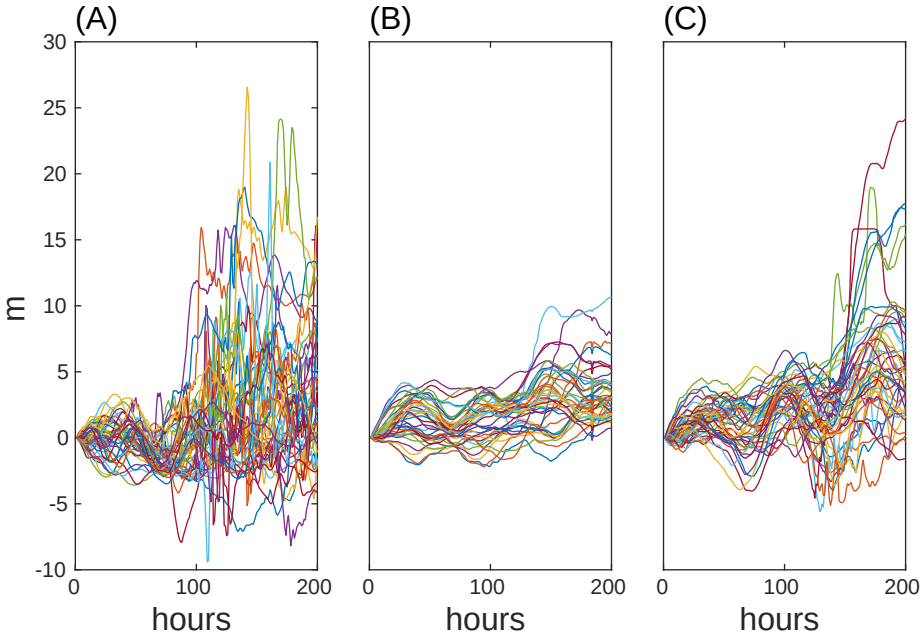

Figure 4.36: Depth variations from the initial position along their trajectories of a sample of the deployed particles on the incoming side of the flow for (A) February, (B) April, (C) June.

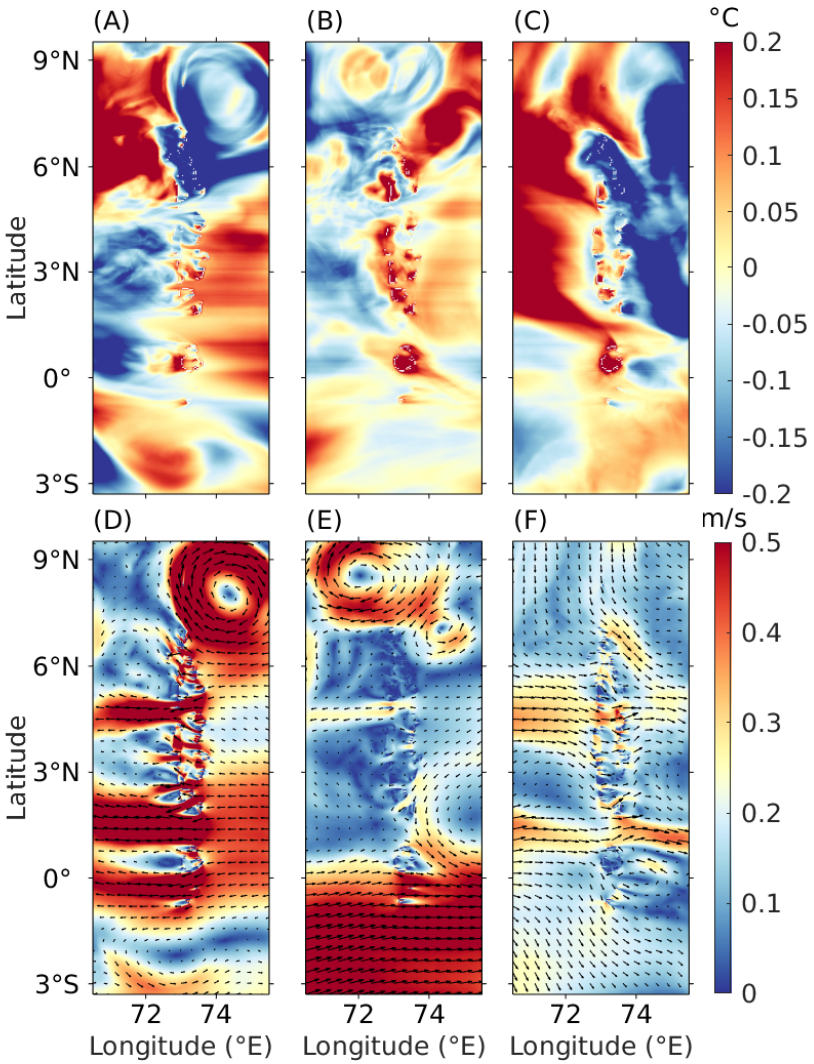

Figure 4.37: Panels A,B,C monthly temperature anomalies with respect to the zonal mean. Panels D,E,F monthly velocity. For (A,D) February, (B,E) April and (C,F) June from R1.6v2 2013 run.

unable to enter the Archipelago (Fig. 4.37,F). This hypothesis is further corroborated by the satellite data over Gaafu, the southest biggest atoll. It is almost enclosed and round-shaped and the SST remains warmer in the inner shallower waters and values of NPP similar to the open ocean (Fig. 4.30).

The same kind of seasonality in the cooling processes described above, might arise around other reefs islands and atolls, as the Chagos Archipelago that shows a similar SST and NPP signal (see Fig. 4.15).

4.3 Conclusions

Since it was first discovered, about 60 years ago (Doty and Oguri, 1956), the phenomenon of enhanced primary productivity around small islands or Island Mass Effect (IME) has been detected worldwide (e.g. Andrade et al. (2014b), Chérubin and Garavelli (2016), Gove et al. (2006), Hamner and Hauri (1981), Heywood et al. (1990)). However, despite the considerable amount of publications on the subject, the exact picture of the physical processes behind it is still unclear (Gove et al., 2016).

Here I have analyzed, around several islands, satellite SST and NPP data. The SST Laplacian showed two different kind of temperature patterns depending on the altitude and the dimension of the island.

Downstream propagation of eddies carrying colder water with high chlorophyll-a concentrations can been seen around several islands, independently of the size (e.g. Figs. 4.5; 4.9; 4.30A,B).

Around islands with considerable altitude, warm and cold temperature anomalies arise on the opposite sides of the island, suggesting the presence of downwelling and upwelling areas. This is, for example, the case of the Canaries, Cape Verde, the Hawaiis, Mauritius main island, Reunion and Vanuatu Archipelago.

The previously listed islands have volcanic origins and an elevation comprised between 800 m (Piton des Neiges, Reunion) and 4200 m (Mauna Kea, Hawaii). The considerable elevation blocks the atmospheric circulation giving rise to atmospheric wakes (Basterretxea et al., 2002, Xie et al., 2001). The resulting positive/negative wind curl forces convergence/divergence zones in the oceanic circulation. Islands with a considerable altitude but a smaller diameter, such as Tristan da Cunha (2800 m) and Saint Helena (800 m), do not show any clear downwelling signal, along with Okinawa that has a bigger diameter but a smaller altitude (500 m) (Table 4.1). However, the surface temperature structure shows few inconsistencies with the pattern that would be generated by an atmospheric wake. Furthermore, a preliminary comparison with the wind stress curl at 25 km does not show a good agreement. On the other hand, the wind data available do not have a high enough resolution to allow a reliable analysis and reach a trustworthy conclusion.

Warmer areas do not appear around smaller islands that usually display only a local cooling, even around archipelagos with considerable altitude such as the Mariana Islands (800m), the Comoros (900m), the Seychelles (800m), and the Andaman and Nicobar islands (700m). The Azores show wake-generated eddies propagating downstream and intense symmetric cooling can be seen around some of the islands. Asymmetric patterns, as

in the case of Rodrigues Island (Mauritius) (Fig. 4.20), are most likely due to deep water wakes. Several other mechanisms might be involved, that can also better explain the increased symmetry of some cases, such as: slope-currents interaction like in the Galapagos (Liu et al., 2014b), internal waves (Merrifield and Holloway, 2002), shallow island wakes (Wolanki and Hamner, 1988) and shear instabilities.

More than one process might coexist, the prevailing one varying along the year and depending on the strength and direction of the incoming flow. This is the case of the Maldivian Archipelago. It has been shown that in spring, the transition period between the monsoons, strong vertical shear enhances the vertical mixing (De Falco et al., 2020). However, even if this mechanism is present all year-round, it becomes predominant only when the incoming flow is not at its maximum intensity. During the NE/SW monsoons, the Northeast/Southwest monsoon currents cross the Archipelago from opposite directions. They successively interact with the two chains of atolls, gaining speed when squeezed in the small straits. The second wave of wakes then produces a more intense upwelling than the first one. The temperature pattern at the surface is, therefore, fairly symmetric in April, when the vertical mixing is dominating, and highly asymmetric in February and June, when the mixing gets obfuscated by the wake signal. Finally, the atolls structure of shallow banks and narrow passages let the nutrient rich water spread into the inner lagoons.

CHAPTER 5

CONCLUSIONS

The Maldives are an atoll nation located in the central Indian Ocean, to the south west of Cape Comorin (India) and composed of 26 atolls and over 1100 islands. It's one of the largest atoll groups on the planet, stretching for more than 800 km. The local climate is strongly influenced by the monsoon seasons, with a wet monsoon dominating from May to October and a dry season from December to March.

Modeling the ocean dynamics around small islands and archipelagos is a complex task and only few articles are available in literature. To investigate the interaction between the large scale ocean circulation and the steep and complicated topography of the Maldives, I have run and validated two sets of simulations with the Coastal and Regional Ocean Community model (CROCO), at 5km and 1.6km of resolution. The study of the local climate was conducted with the aid of several available products, such as: satellite data, oceanic and atmospheric reanalysis.

Tropical coral ecosystems are hotspots of biodiversity. Reefs contribute to key ecosystem services spanning from food and tourism resources to protection against high waves during storms. In the Maldives, coral reefs constitute also the primary building material (Kench, 2011). Whether the ability of coral reefs to provide these essential services will continue in the future, however, is uncertain. Warming of ocean waters, acidification, overfishing, pollution, and damage from coastal development constitute

local and global threats that jeopardize the sustainability of reef systems. In the Maldives, the increase in sea surface temperature (SST) is the most pressing danger (Pisapia et al., 2019, 2016).

Whenever SSTs exceed climatological values by 1 or 2°C in the warmest season for a sufficiently long time, corals expel their symbiotic algae, with consequent bleaching and often mortality. In the Maldives, these prolonged periods can occur in the period between April and June, usually following the peak positive of ENSO (Ibrahim et al., 2017, Pisapia et al., 2016, Schuhmacher et al., 2005, Zahir et al., 2009). The two most recent bleaching events during which coral mortality was widespread occurred in 1998 and in 2016. During the most recent event a careful assessment was possible (Ibrahim et al., 2017, Zahir et al., 2009). In the decade following the 1998 bleaching event, most of the Maldivian coral reefs recovered to pre-bleaching levels (Morri et al., 2015). The recovery was higher and faster in the Indian Ocean than in other areas of the planet. Among the factors that might have contributed to this almost complete recovery, there is the existence of refuges where corals survive through bleaching events and repopulate the surrounding reefs. The presence of refugia was clearly observed during the 2016 event, where some reefs reported bleaching only to 25% or less of their area, despite a much greater (up to 100%) decline in live coral coverage at other sites (Ibrahim et al., 2017).

In this thesis, I have investigated the possibility that also physical drivers might explain the observed patchiness of the bleaching. In spring, the Archipelago is characterized by temperatures about 0.2 °C lower than the surrounding open ocean. This anomalies were clearly visible also during the 2016 El-Niño, possibly mitigating the devastating warming. This localized

cooling spatially shapes the influence of ENSO on the SSTs, and likely contributes to the existence of refugia for corals during otherwise widespread bleaching events.

Using CROCO, with a horizontal resolution of 5 km, I have analysed the local ocean circulation and its interaction with the Maldives topography. The strong currents near the surface abruptly slow down when passing over the steep sea floor and the intense shear enhances vertical mixing, bringing colder water in the mixed layer (ML). During spring, the monsoon winds abate and the ML becomes shallower, the colder water can imprint the ocean surface and lead to local cooling. During the monsoon season, the winds are strong enough to sustain a mixed layer deeper than 30 m and the impact of the mixing on the surface temperature is negligible. Nevertheless, the model resolution of 5 km is not enough to explore the strength variability and the local distribution of this mechanism across and within the atolls.

The reduced SST surrounding the Maldives is probably linked to the Island Mass Effect: the enhanced productivity around small islands discovered about 60 years ago (Doty and Oguri, 1956) that has since been detected worldwide (e.g. Andrade et al. (2014b), Chérubin and Garavelli (2016), Gove et al. (2006), Hamner and Hauri (1981), Heywood et al. (1990)). Local upwelling and vertical mixing can fuel primary productivity by bringing nutrients enriched waters in the euphotic zone, the surface signature of this signal consists in circumscribed colder and saltier anomalies. Despite the huge amount of publications on the subject, the exact picture of the physical processes behind it is still unknown (Gove et al., 2016).

Downstream propagation of eddies carrying colder water with high chlorophyll-a concentrations have been measured around several islands

independently of their size (e.g. Arístegui et al. (1994), Caldeira et al. (2002), Chang et al. (2013), Coutis and Middleton (2002)). The trail signal is clearly visible in the NPP of the Azores and the Hawaii. Temperature cooling and increased productivity that display a strong asymmetry are usually associated with increased eddy production and upwelling in the lee of a wake that are due to the interaction of the surface topography and the oceanic circulation. Peaks in productivity can be observed also upstream of the islands, due to currents impinging on a slope, increased shear or internal waves. The last two mechanisms would give rise to more symmetric patterns.

Analysing the SST variations and the NPP around several small islands and archipelagos, I have noticed that cold/warm anomalies, most likely corresponding to upwelling/downwelling zones, appear around islands with a considerable altitude. The high peaks interact with the synoptic winds and produce a positive/negative wind curl that, through Ekman pumping, can in turn force local upwelling and downwelling (Basterretxea et al., 2002), such as in the case of the Canaries, the Hawaii, Caper Verde, Reunion and Mauritius main island. However, despite having similar altitudes to the previously listed ones, warm areas cannot be recognized around islands with smaller diameters. A preliminary comparison between the SST Laplacian and the wind stress curl at 25 km does not show a good agreement. Unfortunately, the wind data resolution is not enough to compute a reliable curl and further and more detailed analysis are necessary to understand the atmospheric and oceanic mechanisms behind the dowwnelling/upwelling patterns.

The smaller islands studied only display a local cooling and, in several cases, the temperature pattern is fairly symmetric around the obstacle. Even

islands with not negligible altitude - ranging from 700m to 900m - do not show any clear downwelling signal in the SSTs Laplacian. Furthermore, the symmetry cannot be explained by the upwelling in the lee of a wake. More than one oceanic process can coexist with the islands' wake and contribute to create the local cooling. This is the specific case of the Maldivian Archipelago.

In the Maldives, the monsoons force strong reversing winds twice a year that in turn force strong reversing currents. During the winter or dry monsoon, the Northeast Monsoon Current hits the Archipelago. During the summer or wet monsoon, the strong zonal flow changes direction and the Southwest Monsoon Current crosses the islands. Two separate sets of wakes are generated, one for each chain of atolls. The second one being more intense, due to the further acceleration of the currents when they have to squeeze in the narrow passages. A different pattern emerges during the transition period, the currents lose strength, and the vertical transport in the lee of the wake becomes weaker. The surface imprint of the shear-generated vertical mixing can emerge and the local cooling is more symmetric. The percentages of particles that cross the local mixed layer from above or below have similar values. This confirms the hypothesis that mixing, and not upwelling, is entraining colder water from the thermocline in the surface layer and it is, therefore, responsible for the temperature decrease. Finally, the peculiar morphology of the Archipelago, with small islands grouped in almost enclosed atolls and narrow passages, significantly contributes to determine the final spatial pattern of how colder and nutrient enriched waters are ultimately distributed.

Of the simulations performed, only a small fraction was analysed during

this thesis. Several years are available (1993-2016 for R5 and 2010-2016 for R1.6), making possible a climatological analysis of the area. For example, long-term trends of the Eddy Kinetic Energy as well as variations due to climatic events, such as ENSO or IOD, could be explored together with the seasonal cycle. Taking advantage of the reversing circulation of the Archipelago and the tests performed with different bathymetries, it should be possible to deeply investigate the eddy formation due to the interaction between the flow and the islands. With a focus on the presence of asymmetries between the left and right sides, the prevailing occurrence of cyclonic or anticyclonic eddies as well as the relation between their size and the diameter of the obstacle couldbe investigated. Furthermore, coral larvae dispersion and connectivity patterns among different geographical regions could be studied. Not only to try to quantify the tracer dispersion but also the vertical fluxes. Inhibited vertical exchanges could, for example, prevent communication among colonies at different depths. Using two different resolutions, one able to resolve only the mesoscale (R5) and one also the submesoscale (R1.6), it would be possible to differentiate contributions of each to the connectivity. The different bathymetries adopted would help to quantify the effects of the topography on the patterns. Finally, each small island or archipelago could be studied in detail, checking the seasonality of the different processes involved in enhancing the surface productivity to identify the prevailing ones.

BIBLIOGRAPHY

Achituv, Y. and Dubinsky, Z. (1990). Evolution and zoogeography of coral reefs. In Dubinsky, Z. and Goodall, D. W., editors, *Ecosystems of the world: Coral Reefs*, volume 25, pages 1–9. Elsevier, Amsterdam.

Alaee, M. J., Pattiaratchi, C., and Ivey, G. (2007). Numerical simulation of the summer wake of Rottnest Island, Western Australia. *Dynamics of Atmospheres and Oceans*, 43(3):171 – 198.

Amante, C. and Eakins, B. (2009). ETOPO1 1 Arc-Minute Global Relief Model: Procedures, Data Sources and Analysis. *NOAA Technical Memorandum NESDIS NGDC-24. National Geophysical Data Center, NOAA*. Last accessed November 2017.

Andrade, I., Hormazabal, S., and Combes, V. (2014a). Intrathermocline eddies at the Juan Fernandez Archipelago, southeastern Pacific Ocean. *Latin American Journal of Aquatic Research*, 42:888–906.

Andrade, I., Sangrà, P., Hormazabal, S., and Correa-Ramirez, M. (2014b). Island mass effect in the Juan Fernández Archipelago (33°S), Southeastern Pacific. *Deep Sea Research Part I: Oceanographic Research*, 84:86–99.

Anthony, K., Kline, D., Diaz-Pulido, G., Dove, S., and Hoegh-Guldberg, O. (2008). Ocean acidification causes bleaching and productivity loss in coral reef builders. *Proceedings of the National Academy of Sciences of the United States of America*, 105.

Arakawa, A. and Lamb, V. R. (1999). *General Circulation Models of the Atmosphere*. Elsevier.

Arango, H. G., Levin, J. C., Curchitser, E. N., Zhang, B., Moore, A. M., Han, W., Gordon, A. L., Lee, C. M., and Girton, J. B. (2011). Development of a hindcast/forecast model for the Philippine Archipelago. *Oceanography*.

Arístegui, J., Sangrá, P., Hernández-León, S., Cantón, M., Hernández-Guerra, A., and Kerling, J. L. (1994). Island-induced eddies in the Canary islands. *Deep Sea Research Part I: Oceanographic Research Papers*, 41(10):1509 – 1525.

Auclair, F., Benshila, R., Debreu, L., Ducousso, N., Dumas, F.and Marchesiello, P., and Lemarié, F. (2018). Some recent developments around the CROCO initiative for complex regional to coastal modeling. In *COMOD 2018 - Workshop on Coastal Ocean Modelling, Hambourg, Germany*.

Barton, E. D. (2001). *Island Wakes*, pages 1397–1403. San Diego, CA (USA) Academic Press.

Basterretxea, G., Barton, E., Tett, P., Sangrá, P., Navarro-Perez, E., and Arístegui, J. (2002). Eddy and deep chlorophyl maximum response to wind-shear in the lee of Gran Canaria. *Deep Sea Research Part I: Oceanographic Research Papers*, 49(6):1087 – 1101.

Batchelor, G. K. (2000). *An Introduction to Fluid Dynamics*. Cambridge Mathematical Library. Cambridge University Press.

Behrenfeld, M. J. and Falkowski, P. G. (1997). Photosynthetic rates derived from satellite-based chlorophyll concentration. *Limnology and Oceanography*, 42(1):1–20.

Bell, P. (1992). Eutrophication and coral reefs-some examples in the Great Barrier Reef lagoon. *Water Research*, 26:553–568.

Bhaskar, U. T. V. S., Ravichandran, M., and Rao, E. P. R. (2009). Mixed layer depth climatology for the Indian Ocean based on Argo observations. Indian National Centre for Ocean Information Services (INCOIS).

Blanke, B. and Raynaud, S. (1997). Kinematics of the Pacific Equatorial Undercurrent: An eulerian and lagrangian approach from GCM results. *Journal of Physical Oceanography*, 27(6):1038 – 1053.

Brierley, A. and Kingsford, M. (2009). Impacts of climate change on marine organisms and ecosystems. *Current biology*, 19.

Brown, B. E. and Cossins, A. R. (2011). The potential for temperature acclimatisation of reef corals in the face of climate change. In Dubinsky and Stambler (2011), pages 421–433.

Bucciarelli, E., Blain, S., and Tréguer, P. (2001). Iron and manganese in the wake of the Kerguelen Islands (Southern Ocean). *Marine Chemistry*, 73:21–36.

Caldeira, R., Couvelard, X., Vieira, R., Lucas, C., Sala, I., and Casanova, I. V. (2016). Challenges of building an operational ocean forecasting system for small island regions: regional to local. *Journal of Operational Oceanography*, 9(1):1–12.

Caldeira, R., Groom, S., Miller, P., Pilgrim, D., and Nezlin, N. (2002). Sea-surface signatures of the island mass effect phenomena around Madeira Island, Northeast Atlantic. *Remote Sensing of Environment*, 80(2):336 – 360.

Caldeira, R. M. A. and Reis, J. C. (2017). The Azores confluence zone. *Frontiers in Marine Science*, 4:37.

Caldeira, R. M. A. and Sangrá Inciarte, P. (2012). Complex geophysical wake flows. *Ocean Dynamics*, 62.

Capotondi, A., Wittenberg, A. T., Newman, M., Di Lorenzo, E., Yu, J.-Y., Braconnot, P., Cole, J., Dewitte, B., Giese, B., Guilyardi, E., Jin, F.-F., Karnauskas, K., Kirtman, B., Lee, T., Schneider, N., Xue, Y., and Yeh, S.-W. (2015). Understanding ENSO Diversity. *Bulletin of the American Meteorological Society*, 96(6):921–938.

Carilli, J., Donner, S., and Hartmann, A. (2012). Historical temperature variability affects coral response to heat stress. *PloS one*, 7.

Carson, M., Köhl, A., and Stammer, D. (2015). The impact of regional multidecadal and Century-scale internal climate variability on sea level trends in CMIP5 models. *Journal of Climate*, 28(2):853–861.

Carton, J., Chepurin, G., and Chen, L. (2018). SODA3: A new ocean climate reanalysis. *Journal of Climate*, 31.

Chang, M.-H., Tang, T. Y., Ho, C.-R., and Chao, S.-Y. (2013). Kuroshio-induced wake in the lee of Green Island off Taiwan. *Journal of Geophysical Research: Oceans*, 118(3):1508–1519.

Chatterjee, A., Shankar, D., Shenoi, S., Reddy, G., Michael, G. S., Ravichandran, M., Gopalkrishna, V., Eluri, P., Udaya Bhaskar, T., and Sanjeevan, V. (2012). A new atlas of temperature and salinity for the north indian ocean. *Journal of Earth System Science*, 121.

Chaudhury, N., Arora, M., and Gujrati, A. (2019). Mass coral bleaching responses from indian coral reef regions. In *Climate change and the vulnerable Indian coast*. Ministry of Environment, Forest and Climate Change.

Chavanne, C., Flament, P., Lumpkin, R., Dousset, B., and Abderrahim, B. (2002). Scatterometer observations of wind variations induced by oceanic islands: Implications for wind-driven ocean circulation. *Canadian Journal of Remote Sensing*, 28.

Chelton, D. B., deSzoeke, R. A., Schlax, M. G., Naggar, K. E., and Siwertz, N. (01 Mar. 1998). Geographical variability of the first baroclinic Rossby radius of deformation. *Journal of Physical Oceanography*, 28(3):433 – 460.

Cheng, L., Trenberth, K. E., Fasullo, J., Boyer, T., Abraham, J., and Zhu, J. (2017). Improved estimates of ocean heat content from 1960 to 2015. *Science Advances*, 3(3).

Chérubin, L. M. and Garavelli, L. (2016). Eastern Caribbean circulation and island mass effect on St. Croix, US Virgin Islands: A mechanism for relatively consistent recruitment patterns. *PLOS ONE*, 11(3):1–28.

Copernicus Climate Change Service C3S (2017). ERA5: Fifth generation of ECMWF atmospheric reanalyses of the global climate . Copernicus Climate Change Service Climate Data Store (CDS). Last accessed 15 January 2019.

Coutis, P. and Middleton, J. (2002). The physical and biological impact of a small island wake in the deep ocean. *Deep Sea Research Part I: Oceanographic Research Papers*, 49(8):1341 – 1361.

CROCO Developing Team (2020). CROCO's Documentation.

Cushman-Roisin, B. and Beckers, J.-M. (2011). *Introduction to Geophysical Fluid Dynamics: Physical and Numerical Aspects*, page 789. Academic Press, 2 edition.

Damerell, G. M., Heywood, K. J., Calvert, D., Grant, A. L., Bell, M. J., and Belcher, S. E. (2020). A comparison of five surface mixed layer models with a year of observations in the north atlantic. *Progress in Oceanography*, 187:102316.

De Falco, C., Bracco, A., and Pasquero, C. (2020). Climatic and oceanographic controls on coral bleaching conditions in the Maldivian region. *Frontiers in Marine Science*, 7:790.

de Souza, A. C., Marcos, J., Powell, B., Castillo-Trujillo, A. C., and Flament, P. (2015). The Vorticity Balance of the Ocean Surface in Hawaii from a Regional Reanalysis. *Journal of Physical Oceanography*, 45(2):424–440.

de Vos, A., Pattiaratchi, C. B., and Wijeratne, E. M. S. (2014). Surface circulation and upwelling patterns around Sri Lanka. *Biogeosciences*, 11(20):5909–5930.

Debreu, L., Marchesiello, P., Penven, P., and Cambon, G. (2012). Two-way nesting in split-explicit ocean models: algorithms, implementation and validation. *Ocean Modelling*, page 1–21.

Dee, D. P., Uppala, S. M., Simmons, A. J., Berrisford, P., Poli, P., Kobayashi, S., Andrae, U., Balmaseda, M. A.and Balsamo, G., Bauer, P., Bechtold, P., Beljaars, A. C. M., van de Berg, L., Bidlot, J., Bormann, N., Delsol, C., Dragani, R., Fuentes, M., Geer, A. J., Haimberger, L., Healy, S. B., Hersbach, H., Hólm, E. V., Isaksen, L., Kållberg, P., Köhler, M., Matricardi, M., McNally, A. P., Monge-Sanz, B. M., Morcrette, J. J., Park, B. K., Peubey, C., de Rosnay, P., Tavolato, C., Thépaut, J. N., and Vitart, F. S. (2011). The ERA-Interim reanalysis: configuration and performance of the data assimilation system. *Quarterly Journal of the Royal Meteorological Society*, 137(656):553–597.

Dey, S., Nishant, N., Sengupta, K., and Ghosh, S. (2015). Cloud climatology over the oceanic regions adjacent to the Indian Subcontinent: inter-comparison between passive and active sensors. *International Journal of Remote Sensing*, 36.

Dhame, S., Taschetto, A., Santoso, A., and Meissner, K. (2020). Indian Ocean warming modulates global atmospheric circulation trends. *Climate Dynamics*.

Dong, C., McWilliams, J. C., and Shchepetkin, A. F. (2007). Island wakes in deep water. *Journal of Physical Oceanography*, 37(4):962 – 981.

Dong, C., Yuhan, C., and McWilliams, J. (2018). Island wakes in shallow water. *Atmosphere-Ocean*, pages 1–8.

Doty, M. S. and Oguri, M. (1956). The Island Mass Effect. *ICES Journal of Marine Science*, 22(1):33–37.

Dove, S., Kline, D., Pantos, O., Angly, F., Tyson, G., and Hoegh-Guldberg, O. (2013). Future reef decalcification under business-as-usual CO2 emission scenario. *Proceedings of the National Academy of Sciences of the United States of America*, 110.

Dove, S. G. and Hoegh-Guldberg, O. (2006). *The Cell Physiology of Coral Bleaching*, chapter 4, pages 55–71. American Geophysical Union (AGU).

Dubinsky, Z. and Stambler, N., editors (2011). *Coral Reefs: An Ecosystem in Transition*. Springer Netherlands, Dordrecht.

Dufois, F., Hardman-Mountford, N., Greenwood, J., Richardson, A., Feng, M., and Matear, R. (2016). Anticyclonic eddies are more productive than

cyclonic eddies in subtropical gyres because of winter mixing. *Science Advances*, 2.

Durski, S., Glenn, S., and Haidvogel, D. (2004). Vertical mixing schemes in the coastal ocean: Comparison of the level 2.5 mellor-yamada scheme with an enhanced version of the k profile parameterization. *Journal of Geophysical Research (Oceans)*, 109.

Eakin, C. M., Sweatman, H. P. A., and Brainard, R. E. (2019). The 2014-2017 global-scale coral bleaching event: insights and impacts. *Coral Reefs*, 38(4):539–545".

Edwards, A., Clark, S., Zahir, H., Rajasuriya, A., Naseer, A., and Rubens, J. (2001). Coral bleaching and mortality on artificial and natural reefs in Maldives in 1998, sea surface temperature anomalies and initial recovery. *Marine Pollution Bulletin*, 42:7–15.

Ferrario, F., Beck, M., Storlazzi, C., Micheli, F., Shepard, C., and Airoldi, L. (2014). The effectiveness of coral reefs for coastal hazard risk reduction and adaptation. *Nature communications*, 5:3794.

Fieux, M. (2001). Somali current. In Steele, J. H., editor, *Encyclopedia of Ocean Sciences (Second Edition)*, pages 494 – 503. Academic Press, Oxford, second edition edition.

Fringer, O. B., Dawson, C. N., He, R., Ralston, D. K., and Zhang, Y. J. (2019). The future of coastal and estuarine modeling: Findings from a workshop. *Ocean Modelling*, 143:101458.

Gao, Y., Guan, C., Sun, J., and Xie, L. (2019). A wind speed retrieval model for Sentinel-1A EW mode cross-polarization images. *Remote Sensing*, 11:153.

Gargett, A. E. and Holloway, G. (1984). Dissipation and diffusion by internal wave breaking. *Journal of Marine Research*, 42:15–27.

Gelaro, R., McCarty, W., Suárez, M. J., Todling, R., Molod, A., Takacs, L., Randles, C. A., Darmenov, A., Bosilovich, M. G., Reichle, R., Wargan, K., Coy, L., Cullather, R., Draper, C., Akella, S., Buchard, V., Conaty, A., da Silva, A. M., Gu, W., Kim, G.-K., Koster, R., Lucchesi, R., Merkova, D., Nielsen, J. E., Partyka, G., Pawson, S., Putman, W., Rienecker, M., Schubert, S. D., Sienkiewicz, M., and Zhao, B. (2017). The Modern-Era Retrospective Analysis for Research and Applications, Version 2 (MERRA-2). *Journal of Climate*, 30(14):5419–5454.

GHRSST Science Team (2010) (2011). The Recommended GHRSST Data Specification (GDS) 2.0, document revision 4, available from the GHRSST International Project Office.

Glynn, P. W. and D'Croz, L. (1990). Experimental evidence for high temperature stress as the cause of El Niño-coincident coral mortality. *Coral Reefs*, 8(4):181–191.

Gove, J., McManus, M., Neuheimer, A., Polovina, J., Drazen, J., Smith, C., Merrifield, M., Friedlander, A., Ehses, J., Young, C., Dillon, A., and Williams, G. (2016). Near-island biological hotspots in barren ocean basins. *Nature Communications*, 7:10581.

Gove, J. M., Merrifield, M. A., and Brainard, R. E. (2006). Temporal variability of current-driven upwelling at Jarvis Island. *Journal of Geophysical Research: Oceans*, 111(C12).

Griffies, S. M., Boning, C., Bryan, F. O., Chassignet, E. P., Gerdes, R., Hasumi, H., Hirst, A.and Treguier, A.-M., and Webb, D. (2000). Devel-

opments in ocean climate modelling. *Journal of Computational Physics*, 2:123–192.

Guest, J., Baird, A., Maynard, J., Muttaqin, E., Edwards, A., Campbell, S., Yewdall, K., Yang Amri, A., and Chou, L. (2012). Contrasting patterns of coral bleaching susceptibility in 2010 suggest an adaptive response to thermal stress. *PloS one*, 7.

Haidvogel, D. B. and Beckmann, A. (1999). *Numerical Ocean Circulation Modeling*. Environmental Science and Management. Imperial College Press.

Hamner, W. M. and Hauri, I. R. (1981). Effects of island mass: Water flow and plankton pattern around a reef in the Great Barrier Reef lagoon, Australia. *Limnology and Oceanography*, 26(6):1084–1102.

Han, W., Moore, A. M., Levin, J., Zhang, B., Arango, H. G., Curchitser, E., Di Lorenzo, E., Gordon, A. L., and Lin, J. (2009). Seasonal surface ocean circulation and dynamics in the Philippine Archipelago region during 2004–2008. *Dynamics of Atmospheres and Oceans*, 47(1):114 – 137.

Han, W., Vialard, J., McPhaden, M. J., Lee, T., Masumoto, Y., Feng, M., and de Ruijter, W. P. (2015). Indian Ocean Decadal variability: A review. *Bulletin of the American Meteorological Society*, 95(11):1679–1703.

Hasegawa, D., Yamazaki, H., Lueck, R. G., and Seuront, L. (2004). How islands stir and fertilize the upper ocean. *Geophysical Research Letters*, 31(16).

Hermes, J., Masumoto, Y., Beal, L., Koll, R., Vialard, J., Andres, M., Annamalai, H., Behera, S., D'adamo, N., Doi, T., Feng, M., Han, W.,

Hardman-Mountford, N., Hendon, H., Hood, R., Kido, S., Lee, C., Lee, T., Lengaigne, M., and Yu, W. (2019). A sustained ocean observing system in the Indian Ocean for climate related scientific knowledge and societal needs. *Frontiers in Marine Science*, 6.

Heywood, K., Barton, E., and Simpson, J. (1990). The effects of flow disturbance by an oceanic island. *Journal of Marine Research*, 48:55–73.

Hoegh-Guldberg, O., Poloczanska, E. S., Skirving, W., and Dove, S. (2017). Coral reef ecosystems under climate change and ocean acidification. *Frontiers in Marine Science*, 4:158.

Hopley, D., editor (2011). *Encyclopedia of Modern Coral Reefs: Structure, Form and Process*. Springer Netherlands, Dordrecht.

Hormann, V., Centurioni, L. R., and Gordon, A. L. (2019). Freshwater export pathways from the Bay of Bengal. *Deep Sea Research Part II: Topical Studies in Oceanography*, 168:1–12.

Hughes, T., Anderson, K., Connolly, S., Heron, S., Kerry, J., Lough, J., Baird, A., Baum, J., Berumen, M., Bridge, T., Claar, D., Eakin, C. M., Gilmour, J., Graham, N., Harrison, H., Hobbs, J.-P., Hoey, A., Hoogenboom, M., Lowe, R., and Wilson, S. (2018). Spatial and temporal patterns of mass bleaching of corals in the Anthropocene. *Science*, 359:80–83.

Hughes, T., Baird, A., Bellwood, D., Card, M., Connolly, S., Folke, C., Grosberg, R., Hoegh-Guldberg, O., Jackson, J., Kleypas, J., Lough, J., Marshall, P., Nyström, M., Palumbi, S., Pandolfi, J., Rosen, B., and Roughgarden, J. (2003). Climate change, human impacts, and the resilience of coral reefs. *Science (New York, N.Y.)*, 301:929–33.

Hughes, T., Kerry, J., Alvarez-Noriega, M., Álvarez Romero, J., Anderson, K., Baird, A., Babcock, R., Beger, M., Bellwood, D., Berkelmans, R., Bridge, T., Butler, I., Byrne, M., Cantin, N., Comeau, S., Connolly, S., Cumming, G., Dalton, S., Diaz-Pulido, G., and Wilson, S. (2017). Global warming and recurrent mass bleaching of corals. *Nature*, 543:373–377.

Huo, Y. and Peltier, W. (2021). The southeast asian monsoon: dynamically downscaled climate change projections and high resolution regional ocean modelling on the effects of the tibetan plateau. *Climate Dynamics*, pages 1–20.

Hwang, D.-W., Lee, Y.-W., and Kim, G. (2005). Large submarine groundwater discharge and benthic eutrophication in Bangdu Bay on volcanic Jeju Island, Korea. *Limnology and Oceanography*, 50(5):1393–1403.

Ibrahim, N., Mohamed, M., Basheer, A., Haleem, I., Nistharan, F., Schmidt, A., Naeem, R., Abdulla, A., and Grimsditch, G. (2017). Status of coral bleaching in the Maldives 2016. Marine Research Centre, Ministry of Fisheries and Agricolture, Malè, Maldives.

IPCC (2013). *Climate Change 2013: The Physical Science Basis. Contribution of Working Group I to the Fifth Assessment Report of the Intergovernmental Panel on Climate Change*. Cambridge University Press, Cambridge, United Kingdom and New York, NY, USA.

Jackett, D. R. and McDougall, T. J. (01 Apr. 1995). Minimal adjustment of hydrographic profiles to achieve static stability. *Journal of Atmospheric and Oceanic Technology*, 12(2):381 – 389.

Japan Meteorological Agency, Japan (2013). JRA-55: Japanese 55-year reanalysis, daily 3-hourly and 6-hourly data.

JPL Climate Oceans and Solid Earth group (2019). JPL SMAP Level 2B CAP Sea Surface Salinity V4.2 Validated Dataset. Ver. 4.2. PO.DAAC, CA, USA.

Kayanne, H. (2017). Validation of degree heating weeks as a coral bleaching index in the northwestern Pacific. *Coral Reefs*, 36.

Kench, P. (2011). Maldives. In Hopley (2011), pages 648–653.

Kench, P., Mclean, R., Brander, R., Nichol, S., Smithers, S., Ford, M., Parnell, K., and Aslam, M. (2006). Geological effects of tsunami on mid-ocean atoll islands: The Maldives before and after the Sumatran tsunami. *Geology*, 34.

Korsbakken, E. and Furevik, B. (1998). Wind field retrieval from SAR compared with scatterometer wind field during ERS Tandem phase. *Earth Observation Quarterly*, 59:23–26.

Kumar, S., Bhavya, P., Ramesh, R., Gupta, G., Chiriboga, F., Singh, A., Karunasagar, I., Rai, A., Rehnstam-Holm, A.-S., Edler, L., and Godhe, A. (2018). Nitrogen uptake potential under different temperature-salinity conditions: Implications for nitrogen cycling under climate change scenarios. *Marine Environmental Research*, 141:196 – 204.

Lahaye, N., Gula, J., and Roullet, G. (2019). Sea surface signature of internal tides. *Geophysical Research Letters*, 46(7):3880–3890.

Large, W. G., McWilliams, J. C., and Doney, S. C. (1994). Oceanic vertical mixing: A review and a model with a nonlocal boundary layer parameterization. *Reviews of Geophysics*.

Lesser, M. P. (2011). Coral bleaching: Causes and mechanisms. In Dubinsky and Stambler (2011), pages 405–419.

Liu, G., Heron, S., Eakin, C. M., Muller-Karger, F., Vega-Rodriguez, M., Guild, L., De La Cour, J., Geiger, E., Skirving, W., Burgess, T., Strong, A., Harris, A., Maturi, E., Ignatov, A., Sapper, J., Li, J., and Lynds, S. (2014a). Reef-scale thermal stress monitoring of coral ecosystems: New 5-km global products from NOAA coral reef watch. *Remote Sensing*, 6:11579–11606.

Liu, G., Strong, A., Skirving, W., and Arzayus, F. (2006). Overview of NOAA coral reef watch program's near-real time satellite global coral bleaching monitoring activities. *Proceedings of 10th International Coral Reef Symposium*, 1:1783–1793.

Liu, Y., Xie, L., Morrison, J., Kamykowski, D., and Sweet, W. (2014b). Ocean circulation and water mass characteristics around the Galápagos Archipelago simulated by a multiscale nested ocean circulation model. *International Journal of Oceanography*, 2014.

Liu, Z. and Alexander, M. (2007). Atmospheric bridge, oceanic tunnel, and global climatic teleconnections. *Reviews of Geophysics*, 45:2–34.

Locarnini, R. A., Mishonov, A. V., Baranova, O. K., Boyer, T. P., Zweng, M. M., Garcia, H. E., Reagan, J. R., Seidov, D., Weathers, K., Paver, C. R., and Smolyar, I. (2018). World Ocean Atlas 2018, Volume 1: Temperature.

Lough, J., Anderson, K., and Hughes, T. (2018). Increasing thermal stress for tropical coral reefs: 1871–2017. *Scientific Reports*, 8.

Lough, J. M. (2011). Climate change and coral reefs. In Hopley (2011), pages 198–210.

Marchesiello, P. (2020). CROCO: Coastal and Regional Ocean COmmunity model.

Marchesiello, P., McWilliams, J. C., and Shchepetkin, A. (2001). Open boundary conditions for long-term integration of regional oceanic models. *Ocean Modelling*, pages 1–20.

Maynard, J., Anthony, K., Marshall, P., and Masiri, I. (2008). Major bleaching events can lead to increased thermal tolerance in corals. *Marine Biology*, 155:173–182.

McClanahan, T., Darling, E., Maina, J., Muthiga, N., D'agata, S., Jupiter, S., Arthur, R., Wilson, S., Mangubhai, S., Nand, Y., Ussi, A., Humphries, A., Patankar, V., Guillaume, M., Keith, S., Shedrawi, G., Julius, P., Grimsditch, G., Ndagala, J., and Leblond, J. (2019). Temperature patterns and mechanisms influencing coral bleaching during the 2016 El Niño. *Nature Climate Change*, 9.

McClanahan, T., Maina, J., and Muthiga, N. (2011). Associations between climate stress and coral reef diversity in the Western Indian Ocean. *Global Change Biology*, 17:2023 – 2032.

McWilliams, J. C., Huckle, E., and Shchepetkin, A. F. (2009). Buoyancy Effects in a Stratified Ekman Layer. *Journal of Physical Oceanography*, 39(10):2581–2599.

Mellor, G. L. and Yamada, T. (1982). Development of a turbulence closure model for geophysical fluid problems. *Reviews of Geophysics*, 20(4):851–875.

Merrifield, M. A. and Holloway, P. E. (2002). Model estimates of M2 internal tide energetics at the Hawaiian Ridge. *Journal of Geophysical Research: Oceans*, 107.

Minnett, Peter and Kaiser-Weiss, Andrea (2012). GHRSST - Discussion document: Near-surface oceanic temperature gradients.

Mirsaeid, M., Mehdizadeh, M., and Bannazadeh, m. (2017). Investigation of water circulation and temperature effect in Indian Ocean by perturbation method. *International Journal of coastal and offshore engineering*, 1:1–10.

Moberg, F. and Folke, C. (1999). Ecological goods and services of coral reef ecosystems. *Ecological Economics*, 29(2):215 – 233.

Morel, A. and Berthon, J.-F. (1989). Surface pigments, algal biomass profiles, and potential production of the euphotic layer: Relationships reinvestigated in view of remote-sensing applications. *Limnology and Oceanography*, 34(8):1545–1562.

Morri, C., Montefalcone, M., Lasagna, R., Gatti, G., Rovere, A., Parravicini, V., Giuseppe, B., Colantoni, P., and Bianchi, C. (2015). Through bleaching and tsunami: Coral reef recovery in the Maldives. *Marine pollution bulletin*, 98.

NASA Goddard Space Flight Center, Ocean Ecology Laboratory, Ocean Biology Processing Group (2014). MODIS-Aqua Ocean Color Data.

Naseer, A. (2003). *The integrated growth response of coral reefs to environmental forcing: morphometric analysis of coral reefs of the Maldives.* PhD thesis, Maldives National University.

Naseer, A. and Hatcher, B. (2004). Assessing the integrated growth response of coral reefs to monsoon forcing using morphometric analysis of reefs in the Maldives. *Coral Reefs*.

National Centers for Environmental Information (NOAA) (2016). GHRSST Level 4 AVHRR_OI Global Blended Sea Surface Temperature Analysis (GDS version 2) from NCEI. Ver. 2.0. PO.DAAC, CA, USA. Last accessed 15 January 2020.

Nurser, G. and Bacon, S. (2014). The Rossby radius in the Arctic Ocean. *Ocean Sci.*, 10:967–975.

Owen, A., Kruijsen, J., Turner, N., and Wright, K. (2011). Marine energy in the Maldives. pre-feasibility report on scottish support for Maldives marine energy implementation. Technical report, Centre for Understanding Sustainable Practice, Robert Gordon University.

Penin, L., Vidal-Dupiol, J., and Adjeroud, M. (2013). Response of coral assemblages to thermal stress: Are bleaching intensity and spatial patterns consistent between events? *Environmental monitoring and assessment*, 185:5031–5042.

Perret, G., Stegner, A., Farge, M., and Pichon, T. (2006). Cyclone-anticyclone asymmetry of large-scale wakes in the laboratory. *Physics of Fluids*, 18.

Pisapia, C., Burn, D., and Pratchett, M. (2019). Changes in the population and community structure of corals during recent disturbances (February 2016-October 2017) on Maldivian coral reefs. *Scientific Reports*, 9:8402.

Pisapia, C., Burn, D., Yoosuf, R., Najeeb, A., Anderson, K., and Pratchett,

M. (2016). Coral recovery in the central Maldives archipelago since the last major mass-bleaching, in 1998. *Scientific Reports*, 6.

Plaisance, L., Caley, M., Brainard, R., and Knowlton, N. (2011). The diversity of coral reefs: what are we missing? *PloS one*, 6.

Preu, C. and Engelbrecht, C. (1991). Patterns and processes shaping the present morphodynamics of coral reef islands—case study from the North-Male atoll, Maldives (Indian Ocean). In Brückner, H. and Radtke, U., editors, *From the North Sea to the Indian Ocean*, pages 209–220. Franz Steiner Verlag Stuttgart.

Quinn, N. J. and Zahir, H. (2013). Assessment of coral cover on Maldivian reefs after the 1998 bleaching event and 2004 tsunami. *Galaxea, Journal of Coral Reef Studies*, 15:45–53.

Radice, V. Z., Hoegh-Guldberg, O., Fry, B., Fox, M. D., and Dove, S. G. (2019). Upwelling as the major source of nitrogen for shallow and deep reef-building corals across an oceanic atoll system. *Functional Ecology*, 33(6):1120–1134.

Rao, A. R., Rao, G. N., Sreenivas, P., and Kumar, P. V. H. (2013). Role of meso-scale eddies on circulation in the South Eastern Arabian Sea in 2009. *Marine Geodesy*, 36(3):319–333.

Renault, L., Molemaker, M. J., Gula, J., Masson, S., and McWilliams, J. C. (2016). Control and stabilization of the gulf stream by oceanic current interaction with the atmosphere. *Journal of Physical Oceanography*, 46(11):3439 – 3453.

Reynolds, R., Smiths, T., Liu, Chelton, D., Casey, K., and Schlax, M.

(2007). Daily high-resolution-blended analyses for sea surface temperature. *Journal of Climate*, 20.

Richmond, R. H., Tisthammer, K. H., and Spies, N. P. (2018). The effects of anthropogenic stressors on reproduction and recruitment of corals and reef organisms. *Frontiers in Marine Science*, 5:226.

Risien, C. M. and Chelton, D. B. (2008). A Global Climatology of Surface Wind and Wind Stress Fields from Eight Years of QuikSCAT Scatterometer Data. *Journal of Physical Oceanography*, 38(11):2379–2413.

Risk, M. and Sluka, R. (2000). The Maldives: A nation of atolls. *Coral Reefs of the Indian Ocean: Their Ecology and Conservation*, pages 325–351.

Robertson, R. and Dong, C. (2019). An evaluation of the performance of vertical mixing parameterizations for tidal mixing in the regional ocean modeling system (roms). *Geoscience Letters*, 6.

Ronald, B. S., Gleason, A. C., Gluhosky, P. A., and Grubišić, V. (1997). The wake of St. Vincent. *Journal of the Atmospheric Sciences*, 54(5):606 – 623.

Roy, S., Saha, S., Bhowmik, S., and Kundu, P. (2014). Analysis of monthly cloud climatology of the indian subcontinent as observed by TRMM precipitation radar. *International Journal of Climatology*, 35.

Safaie, A., Silbiger, N., Mcclanahan, T., Pawlak, G., Barshis, D., Hench, J., Rogers, J., Williams, G., and Davis, K. (2018). High frequency temperature variability reduces the risk of coral bleaching. *Nature Communications*, 9.

Saji, N. H. (2018). *The Indian Ocean Dipole*, pages 1–34. Oxford University Press.

Sasamal, S. K. (2006). Island mass effect around the Maldives during the winter months of 2003 and 2004. *International Journal of Remote Sensing*, 27(22):5087–5093.

Schott, F. and McCreary, J. (2001). The monsoon circulation of the Indian Ocean. *Progress in Oceanography*, 51:1–123.

Schott, F., Xie, S.-P., and McCreary, J. (2009). Indian Ocean circulation and climate variability. *Reviews of Geophysics*, 47.

Schuhmacher, H., Loch, K., Loch, W., and See, W. (2005). The aftermath of coral bleaching on a Maldivian reef - a quantitative study. *Facies*, 51:80–92.

Shchepetkin, A. and McWilliams, J. (2003). A method for computing horizontal pressure-gradient force in an oceanic model with a nonaligned vertical coordinate. *Journal of Geophysical Research C: Oceans*, 108:35–1.

Shchepetkin, A. and McWilliams, J. (2005). The Regional Oceanic Modeling System (ROMS): a split-explicit, free-surface, topography-following-coordinate ocean model. *Ocean Modelling*, 9:347–404.

Shchepetkin, A. F. and McWilliams, J. C. (2009). Computational kernel algorithms for fine-scale, multiprocess, longtime oceanic simulations. *Handbook of Numerical Analysis*, 14:121–183.

Shineng, H. and Fedorov, A. V. (2019). Indian Ocean warming can strengthen the Atlantic meridional overturning circulation. *Nature Climate Change*, 9:747–751.

Song, Y. and Haidvogel, D. (1994). A semi-implicit ocean circulation model using a generalized topography following coordinate system. *Journal of Computational Physics*, 115:228–248.

Spall, M. and Pedlosky, J. (2013). Interaction of Ekman Layers and islands. *Journal of Physical Oceanography*, 43:1028–1041.

Stegner, A. (2014). Oceanic island wake flows in the laboratory. In *Modeling Atmospheric and Oceanic Flows*, pages 265–276. American Geophysical Union (AGU).

Storlazzi, C., Cheriton, O., van Hooidonk, R., Zhao, Z., and Brainard, R. (2020). Internal tides can provide thermal refugia that will buffer some coral reefs from future global warming. *Scientific Reports*, 10:13435.

Street, J. H., Knee, K. L., Grossman, E. E., and Paytan, A. (2008). Submarine groundwater discharge and nutrient addition to the coastal zone and coral reefs of leeward Hawai'i. *Marine Chemistry*, 109(3):355 – 376.

Teinturier, S., Stegner, A., Didelle, H., and Viboud, S. (2010). Small-scale instabilities of an island wake flow in a rotating shallow-water layer. *Dynamics of Atmospheres and Oceans*, 49:1–24.

Thompson, D. M. and van Woesik, R. (2009). Corals escape bleaching in regions that recently and historically experienced frequent thermal stress. *Proceedings of the Royal Sociaety B*, 276:2893–2901.

Timmermann, A., An, S.-I., Kug, J.-S., Jin, F.-F., Cai, W., Capotondi, A., Cobb, K. M., Lengaigne, M., McPhaden, M. J., Stuecker, M. F., Stein, K., Wittenberg, A. T., Yun, K.-S., Bayr, T., Chen, H.-C., Chikamoto, Y., Dewitte, B., Dommenget, D., Grothe, P., Guilyardi, E., Ham, Y.-G.,

Hayashi, M., Ineson, S., Kang, D., Kim, S., Kim, W., Lee, J.-Y., Li, T., Luo, J.-J., McGregor, S., Planton, Y., Power, S., Rashid, H., Ren, H.-L., Santoso, A., Takahashi, K., Todd, A., Wang, G., Wang, G., Xie, R., Yang, W.-H., Yeh, S.-W., Yoon, J., Zeller, E., and Zhang, X. (2018). El Niño-Southern Oscillation complexity. *Nature*, 559(7715):535—545.

UK Met Office (2005). GHRSST Level 4 OSTIA Global Foundation Sea Surface Temperature Analysis. Ver. 1.0. PO.DAAC, CA, USA. Last accessed 12 February 2020.

Umlauf, L. and Burchard, H. (2003). A generic length-scale equation for geophysical turbulence models. *Journal of Marine Research*, 61:235–265.

Vallis, G. K. (2017). *Atmospheric and Oceanic Fluid Dynamics: Fundamentals and Large-Scale Circulation*. Cambridge University Press, 2 edition.

Velleman, P. F. and Hoaglin, D. C. (1981). *Applications, Basics, and Computing of Exploratory Data Analysis*. Duxbury Press.

Vitousek, P. M., Mooney, H. A., Lubchenco, J., and Melillo, J. M. (1997). Human domination of Earth's ecosystems. *Science*, 277(5325):494–499.

Wilkinson, C. (2004). *Status of Coral Reefs of the World: 2004*. Global Coral Reef Monitoring Network and Australian Institute of Marine Science, Townsville.

Wilkinson, C. (2008). *Status of Coral Reefs of the World: 2008*. Global Coral Reef Monitoring Network and Australian Institute of Marine Science, Townsville.

Wolanki, E. and Hamner, W. M. (1988). Topographically controlled fronts in the ocean and their biological influence. *Science*, 241(4862):177–181.

Woodruff, S. D., Slutz, R. J., Jenne, R. L., and Steurer, P. M. (1987). A comprehensive ocean-atmosphere data set. *Bulletin of the American Meteorological Society*, 68(10):1239–1250.

Wooldridge, S. (2009). Water quality and coral bleaching thresholds: Formalising the linkage for the inshore reefs of the Great Barrier Reef, Australia. *Marine Pollution Bulletin*, 58:745–751.

Wyatt, A., Leichter, J., Toth, L., Miyajima, T., Aronson, R., and Nagata, T. (2020). Heat accumulation on coral reefs mitigated by internal waves. *Nature Geoscience*, 13:1–7.

Wyrtki, K. (1973). An equatorial jet in the Indian Ocean. *Science*, 181(4096):262–264.

Xie, S., Liu, W. T., Liu, Q., and Nonaka, M. (2001). Far-reaching effects of the Hawaiian Islands on the Pacific ocean-atmosphere system. *Science*, 292(5524):2057–2060.

Zahir, H., Quinn, N., and Cargillia, N. (2009). Assessment of Maldivian coral reefs in 2009 after natural disasters. Marine Research Center.

Zeiden, K. L., Rudnick, D. L., and MacKinnon, J. A. (2019). Glider observations of a mesoscale oceanic island wake. *Journal of Physical Oceanography*, 49(9):2217 – 2235.

Zimmerman, L. I. (1969). Atmospheric wake phenomena near the Canary Islands. *Journal of Applied Meteorology and Climatology*, 8(6):896 – 907.

Zweng, M. M., Reagan, J. R., Seidov, D., Boyer, T. P., Locarnini, R. A., Garcia, H. E., Mishonov, A. V., Baranova, O. K., Weathers, K., Paver, C. R., and Smolyar, I. (2018). World Ocean Atlas 2018, Volume 2: Salinity.